

STUDIES ON IMPROVING QUALITY FACTOR OF 2D GMR GRATINGS AND ON
NONWETTING PROPERTIES OF PLASMA-TREATED POLYMER SURFACES
TOWARDS LIQUID METAL MICROFLUIDICS

by

Sachin Babu

APPROVED BY SUPERVISORY COMMITTEE:

Jeong-Bong Lee, Chair

Siavash Pourkamali

Hongbing Lu

Matthew J. Goeckner

Lawrence J. Overzet

Copyright 2021

Sachin Babu

All Rights Reserved

To my parents.

STUDIES ON IMPROVING QUALITY FACTOR OF 2D GMR GRATINGS AND ON
NONWETTING PROPERTIES OF PLASMA-TREATED POLYMER SURFACES
TOWARDS LIQUID METAL MICROFLUIDICS

by

SACHIN BABU, MS

DISSERTATION

Presented to the Faculty of
The University of Texas at Dallas
in Partial Fulfillment
of the Requirements
for the Degree of

DOCTOR OF PHILOSOPHY IN
ELECTRICAL ENGINEERING

THE UNIVERSITY OF TEXAS AT DALLAS

May 2021

ACKNOWLEDGMENTS

I would like to thank my parents for their unwavering support in all my endeavors.

I would like to thank my colleague, Behnoush Dousti, for invaluable discussions and collaborations, without whom a key portion of this work would not be possible. Additionally, I would like to thank my MiNDs group members, Dr. Steven Foland, Ziyu Chen, and Arkadeep Mitra, as well as colleague Michael Choi, for lending their ears to listen to countless ideas and discussions. I hope it was as inspiring and engaging for you as it was for me.

I would like to thank my committee members, Prof. Matthew Goeckner, Prof. Siavash Pourkamali, Prof. Hongbing Lu, and Prof. Lawrence Overzet, for kindly agreeing to serve on my dissertation defense committee. Finally, I would like to thank my advisor, Prof. Jeong-Bong Lee, for continually supporting me throughout my graduate career. If I succeed in my future endeavors, it will surely be due to the lessons I learned under his mentorship.

April 2021

STUDIES ON IMPROVING QUALITY FACTOR OF 2D GMR GRATINGS AND ON
NONWETTING PROPERTIES OF PLASMA-TREATED POLYMER SURFACES
TOWARDS LIQUID METAL MICROFLUIDICS

Sachin Babu, PhD
The University of Texas at Dallas, 2021

Supervising Professor: Jeong-Bong Lee

Polydimethylsiloxane (PDMS) is a biocompatible elastomer that is used widely in microfabrication, and this work presents three studies that utilize this elastomer in the areas of strain sensors, thin film coatings, and liquid metal microfluidics. The first study is on improving the quality factor of a 2D guided-mode resonance (GMR) strain sensor, which is a binary grating made of PDMS and titanium dioxide. To improve the quality factor, a slotting design rule is developed that can be applied to any grating design. To study the effect of the slotting design rule, finite element analysis simulations were performed, and the results indicate that the design rule helps produce resonances with at least a 6-fold increase in quality factor over the original design as well as more axially-symmetric sensitivities. The second study concerns the CF_4/O_2 plasma-treatment of polymers (PDMS being one of several studied) which creates a nonwetting surface toward gallium-based liquid metals. Gallium-based liquid metals tend to wet a variety of materials, and a method that allows conversion of a previously wetting polymer surface to a nonwetting one can help open new areas of research for liquid metal applications. The study

conducts a variety of surface-level analyses – contact angle goniometry, X-ray photoelectron spectroscopy (XPS), atomic force microscopy (AFM), and apparent surface free energy analysis – to show that the cause of the nonwetting property is primarily due to surface roughness. The third study is on the feasibility of CF_4/O_2 plasma-treated PDMS channels to allow actuation and generation of surface-oxidized gallium based liquid metal (oxLM) droplets. The results of the study indicate that actuation and generation of oxLM droplets is not feasible due to the surface oxide of the liquid metal.

TABLE OF CONTENTS

ACKNOWLEDGMENTS	v
ABSTRACT.....	vi
LIST OF FIGURES	xi
LIST OF TABLES.....	xvi
CHAPTER 1 BACKGROUND AND MOTIVATION	1
1.1 Background on guided-mode resonance and motivation for improving the quality factor of 2D guided-mode resonance gratings	1
1.2 Background of gallium-based liquid metals and motivation for seeking an understanding of the cause of non-wetting property of plasma-treated polymer surfaces for liquid metals	4
1.3 Literature survey on liquid metal microfluidics and motivation for using CF ₄ /O ₂ plasma-treated surfaces for pneumatics-based liquid metal microfluidics	7
1.4 Research objectives and chapter outline	12
CHAPTER 2 AXIALLY-ANISOTROPIC HIERARCHICAL GRATING 2D GUIDED-MODE RESONANCE STRAIN-SENSOR	14
2.1 Introduction.....	14
2.2 Methods.....	20
2.2.1 Design of Slotted-Disc GMR filters.....	20
2.2.2 Axially Anisotropic Refractive Index	22
2.2.3 Choosing q and S.....	24
2.3 Results.....	25
2.3.1 3D FEA simulation.....	25
2.3.2 Sensitivity Study Results.....	28
2.3.3 Quality factor study results	30
2.4 Discussion	32
2.5 Conclusion	34
CHAPTER 3 PLASMA TREATMENT PROCESS TO CONVERT POLYMER SURFACES INTO NON-WETTING SUBSTRATES FOR GALLIUM-BASED LIQUID METALS	36

3.1	Introduction.....	37
3.2	Materials and fabrication	39
3.3	Experimental Methods	41
	3.3.1 Contact angle measurements.....	41
	3.3.2 Surface characterization methods.....	42
3.4	Results and discussion	43
	3.4.1 CF ₄ /O ₂ plasma exposure time study for PDMS	43
	3.4.2 Contact angle measurements of O ₂ plasma-treated polymers.....	46
	3.4.3 Contact angle measurements for CF ₄ /O ₂ plasma-treated polymer.....	48
	3.4.4 Surface chemistry	50
	3.4.5 A primer on Young, Wenzel, and Cassie-Baxter state.....	54
	3.4.6 Surface roughness analysis of pristine and CF ₄ /O ₂ plasma-treated surfaces using AFM	56
	3.4.7 Estimating apparent surface free energy	58
	3.4.8 Generalizing the process to other polymers	60
3.5	Conclusion	61
 CHAPTER 4 FEASIBILITY STUDY ON PNEUMATIC ACTUATION AND GENERATION OF SURFACE-OXIDIZED GALLIUM-BASED LIQUID METAL DROPLETS IN NON- WETTING PLASMA-TREATED POLYMER CHANNELS		62
4.1	Channel design choice for droplet generation and actuation	63
4.2	Experimental setup and fabrication	64
	4.2.1 Experimental setup.....	64
	4.2.2 Fabrication of plasma-treated PDMS microfluidic channels	65
	4.2.3 Limitations of plasma-treated PDMS surfaces.....	66
	4.2.4 Limitations of channel depth and shape	67
4.3	Actuation results	69
	4.3.1 Plasma-treated 1D channels	69
	4.3.2 Liquid metal droplet generation results.....	70
	4.3.3 H ₂ SO ₄ -treated channels results.....	72
4.4	Conclusion	74
 CHAPTER 5 SUMMARY AND FUTURE WORKS		75

5.1	Summary and conclusions	75
5.2	Future works	76
APPENDIX	TUNABLE EXTRAORDINARY OPTICAL TRANSMISSION	78
A.1	Overview of extraordinary optical transmission (EOT)	78
A.2	Complex index of refraction of galinstan	83
A.3	Design of tunable color filter	85
A.4	Simulation of tunable optical filter	87
A.5	Analysis of simulation results	89
A.6	Fabrication approach and limitations.....	92
A.7	Conclusions and future work	95
REFERENCES	97
BIOGRAPHICAL SKETCH	111
CURRICULUM VITAE		

LIST OF FIGURES

Figure 1.1. Guided-mode resonance phenomenon as broadband light interacts with a binary slab grating waveguide. (a) Diagram depicting a 1D binary grating, (b) diagram depicting a 2D binary (or “solid disc”) grating. Note: “sup” stands for “superstrate” and “sub” stands for “substrate.”	2
Figure 1.2. Demonstration of the mechanical strength of the surface oxide (a) free-standing liquid metal wires (270 μ m), and (b) 3D printed tower of liquid metal droplets, reprinted from Ladd et al. [33] © 2013 Wiley.	6
Figure 1.3. (a) Galinstan [®] femtosyringe, reprinted from Ref. [43] © 1999 Nature Biotechnology; (b) Actuation of liquid metal droplet via magnetic repulsion, reprinted from Ref. [44] © 2006 IEEE; (c) hydraulic actuation of liquid metal droplet in Teflon [®] solution reprinted from Ref. [45] © 2007 IEEE; (d) continuous electrowetting of liquid metal droplet in basic electrolyte solution reprinted from [46], © 2014 IEEE.....	8
Figure 1.4. (a) 3D lyophobic micropillar tunnel, reprinted from Ref. [47] © 2012 IEEE; (b) Pneumatic actuation of HCl-vapor deoxidized liquid metal droplet in PDMS, reprinted from Ref. [36] © 2014 American Chemical Society; (c) Neverwet coating as nonwetting surface for liquid metal, reprinted from Ref. [48] © 2018 American Chemical Society; (d) Gallium thin film coating on PDMS channel creates nonwetting surface that allows pneumatic actuation of liquid metals, reprinted from Ref. [49] © 2019 American Chemical Society.	10
Figure 1.5. (a) liquid metal droplet generation in PEG fluid [50] © 2012 IEEE; (b) deoxidized liquid metal droplet using HCl-impregnated paper. © 2012 IEEE.....	11
Figure 2.1. Design of 2D GMR grating strain sensor. (a) Solid-disc GMR reflection filter, consisting of discs of TiO ₂ embedded in PDMS; $\Lambda_z=560\text{nm}$, $\Lambda_y=480\text{nm}$, $t=200\text{nm}$, $d=420\text{nm}$, $n_H=2.35$, $n_L=1.4$, $n_{\text{sup}}=1.0$, $n_{\text{sub}}=1.4$. (b) Slotted disc GMR reflection filter, a grating-within-a-grating device, consisting of slotted-discs of TiO ₂ embedded in PDMS; $\Lambda_z=\Lambda_y=480\text{nm}$, $t=200\text{nm}$, $d=420\text{nm}$, $S=120\text{nm}$, $q=0.5$, $n_H=2.35$, $n_L=1.4$, $n_{\text{sup}}=1.0$, $n_{\text{sub}}=1.4$	22
Figure 2.2. (a) Binary grating with PDMS substrate and air superstrate. The grating parameters are $S=120\text{nm}$, $q=0.5$, $n_H=2.35$, $n_L=1.4$, $n_{\text{sup}}=1.0$, $n_{\text{sub}}=1.4$. (b) Plot of $\Delta n = (n_{\parallel} - n_{\perp})$, vs. q ; for $q = 0.5$, $n_{\parallel} = 1.93$ and $n_{\perp} = 1.70$, and $\Delta n = 0.23$	23
Figure 2.3. COMSOL [®] simulation of (a) solid disc GMR filter device using parameters in Figure 2.1a (b) slotted-disc GMR filter device using parameters in Figure 2.1 b.....	26

Figure 2.4. (a) COMSOL [®] stress-strain simulation of slotted-disc for 25% Z-axis strain; (b) close-up view of center 25% Z-axis strained unit cell ; resting slotted disc (pink) and 25% Z-axis strained slotted disc (purple) in (c) top view, and (d) isometric view, used for the 2-port FEA model.	28
Figure 2.5. Reflection spectrum obtained from COMSOL [®] simulations using the RF module. The ‘Y-peak’ denotes the peak that shifts under Y-axis strains, and ‘Z-peak’ denotes the peak that shifts under Z-axis strains. (a) solid-disc under Z-axis strain; Note the drop in Y-peak reflectance. (b) solid-disc under Y-axis strain; note the Y-peak partially the Z-peak around 15% strain, and move past it at 25% strain. (c) slotted-disc under Z-axis strain; note the drop in reflectivity of the Y-peak. (d) slotted-disc under Y-axis strain; there is a significant drop in Z-peak reflectance.	29
Figure 2.6. (a) Sensitivity vs. strain for solid-disc grating. (b) Sensitivity vs. strain for slotted-disc grating. (c) Quality factor vs. strain for solid-disc grating. (d) Quality factor vs. strain for slotted-disc grating.	31
Figure 3.1. Static contact angle vs. exposure time to CF ₄ /O ₂ plasma treatment from Babu et al. [37]. © 2020 IEEE. The authors measure the contact angles using 8μL galinstan droplets in ambient air, for both resting (solid circle) and 25% strained (solid square) 2 mm thick PDMS slabs.....	45
Figure 3.2. Static contact angle measurements of liquid metal droplets on SU8-2010 and S1813, for pristine (green data points, bottom inset figures) and 60 s O ₂ plasma-treated (red data points, top inset figures).....	47
Figure 3.3. Dynamic contact angle measurements of liquid metal droplets on SU8-2010 and S1813, for pristine (left plot) and 60 s O ₂ plasma-treated (right plot) surfaces.....	48
Figure 3.4. Static contact angle measurements of CF ₄ /O ₂ plasma-treated (top) and pristine (bottom) polymer films on silicon wafer using surface-oxidized galinstan droplets. 8uL liquid metal droplets were used; all droplet radii are ~2 mm.	48
Figure 3.5. Dynamic contact angle measurements for (a) pristine and (b) plasma-treated materials. The vertically downward arrow indicates infusion, the vertically upward arrow indicates withdrawal; LM stands for “liquid metal”.....	49
Figure 3.6. XPS survey of (a) plasma-treated (PDMS-PL curve) and pristine (PDMS-PR curve) PDMS; and (b) plasma-treated (SU8-PL curve) and pristine (SU8-PR curve) SU8-2010.	51
Figure 3.7. (a) XPS survey spectrum of S1813, plasma-treated (top) and pristine (bottom); (b) XPS survey spectrum of Kapton tape (polyimide), plasma-treated (top) and pristine (bottom).....	51

Figure 3.8. C 1s XPS spectra for (a) pristine PDMS (PDMS-PR), the inset is the molecular structure of PDMS (redrawn from Seethapathy et al. [121]); (b) pristine SU8 (SU8-PR), the inset is the molecular structure of SU8 (redrawn from Madou et al. [122]); (c) plasma-treated PDMS (PDMS-PL); (d) plasma-treated SU8 (SU8-PL). The binding energies were obtained from Bratt, et al. [123] and Cordeiro et al. [124].	52
Figure 3.9. (a) Young state and the equation associated with it assumes the surface is perfectly smooth; (b) the Wenzel state and the equation associated with it assumes the surface is rough and that the liquid is contact with more surface area that the area enclosed by the triple contact line between liquid, air, and solid, which leads to more wetting; (c) the Cassie-Baxter state and the equation associated with it assumes the surface is rough and the liquid has partial contact with the surface leading to a less wetting.	55
Figure 3.10. (a) 3D surface plot of plasma-treated PDMS and its (b) height profile; (c) 3D surface plot of pristine PDMS and its (d) height profile.	57
Figure 3.11. (a) 3D surface plot of pristine S1813 and (b) 3D surface plot of plasma-treated S1813; (c) 3D surface plot of pristine Kapton tape and (d) 3D surface plot of plasma-treated Kapton tape; (e) 3D surface plot of pristine SU8-2010 and (f) 3D surface plot of plasma-treated SU8-2010.	58
Figure 4.1. (a) HCl-vapor exposed liquid metal droplet in PDMS T-junction channel, reprinted from Ref. [36] © 2014 American Chemical Society; (b) T-junction channel with superhydrophobic surface for generation of uniform water slugs, reprinted from Ref. [140] under Creative-Commons CC-BY license; (c) CAD drawing of 1D Channel; (d) CAD drawing of T-junction channel.	64
Figure 4.2. Fabrication steps for making a 1D PDMS channel and a T-junction channel.	65
Figure 4.3. PDMS plasma-treated nonwetting T-junction channel (a) isometric view and (b) top view.	67
Figure 4.4. 600 s CF ₄ /O ₂ plasma-treated square channels (a) before liquid metal touch test and (b) residue after touch test. 600 s CF ₄ /O ₂ plasma-treated cylindrical channels: (c) before liquid metal touch test, (d) with liquid metal drop on channels, and (e) free movement of liquid metal droplets, demonstrating that plasma treatment is better suited for cylindrical channels than square channels.	68
Figure 4.5. (a) surface oxidized liquid metal slug; (b) 37% HCl (aq.) introduced, however slug not moving, air is moving freely around the slug; (c) 37% HCl (aq.) a few mm from slug, still no movement, slug surface oxide has been removed. HCl (aq.) now forms a slip layer and actuation (d-f) is now possible.	70

- Figure 4.6. (a) a very long liquid metal slug is draw out from the T-junction. As pressure is applied (to the right) the oxide layer buckles (b) with some parts stable and other parts deforming. As pressure builds due to the strength of the oxide layer it reaches a threshold that eventually over comes the strength of the oxide skin and the liquid metal droplet rapidly stretches and deforms until the air can flow without hindrance with in the channel.71
- Figure 4.7. (a-d) Demonstration that the mechanical strength of the oxide layer can keep a liquid metal droplet flat, preventing the surface tension forces from forming a uniformly spherical droplet, until the oxide layer is removed by HCl vapors.....72
- Figure 4.8. (a) contact angle vs reaction time to 89% H₂SO₄ solution, and (b) SEM image of PDMS exposed to 89% H₂SO₄ for 90s; reprinted from Ref. [53] © 2015 American Chemical Society. (c) hierarchical roughness of PDMS surface caused by 89% H₂SO₄ for 90s, fabricated by the author.....73
- Figure 4.9. (a) serpentine T-junction channel, reprinted from Ref. [53] © 2015 American Chemical Society; (b) replica of 89% H₂SO₄-treated serpentine PDMS channel, with oxLM residue; (c) 89% H₂SO₄-treated 1D channel with oxLM residue, (d) 89% H₂SO₄-treated T-junction channel with oxLM residue.....73
- Figure A.1. (a) diagram depicting a metallic hole array on dielectric illuminated by white at normal incidence from Rodrigo et al. [144] © 2016 IEEE; (b) example of EOT from Genet et al. of [150] of two square hole arrays, left array with period 550 nm (red) and right array with period 450 nm (green), in Ag thin film illuminated underneath by white light with transmitted light on the other side © 2007 Nature Publishing Group; (c) diagram of surface plasmon polaritons at metal/dielectric interface from Barnes et al. [148] © 2003 Nature Publishing Group; (d) measured spectrum transmitted under normal-incident white light on to a triangular hole array (170 nm diameter, 520 nm period) milled in 225 nm thick Au film on glass substrate from Genet et al. [150] © 2007 Nature Publishing Group80
- Figure A.2. (a) diagram of 15x15 liquid metal hole array; (b) fabricated EOT optical filter using liquid metal EGaIn embedded in PDMS with hole diameter 357 μm and period of 714 μm with liquid metal thickness of 80 μm and device thickness of 1 mm; (c) measured complex dielectric constants for EGaIn; and (d) plots of transmission profile at different periods (due to applied strain) (left) and shift in anti-resonance (AR) peak due to applied strain; all images from Wang et al. [151] © 2012 Optical Society of America82
- Figure A.3. The n (real part) and k (complex part) of the complex index of refraction for galinstan (calculated empirically) and aluminum from refractiveindex.info [153], data collected from report by Rakić et al. [154]85

Figure A.4. (a) back illuminated plasmonic color filters; (b) SEM micrograph of hexagonal hole array in thin film of aluminum; measured transmission of hole array for (c) red (diameters ranging from 160 nm to 280 nm with period of 420 nm), (d) green (diameters ranging from 120 nm to 240 nm with period of 340 nm), and (e) blue (diameters ranging from 100 nm to 180 nm with period of 260 nm); all images from Yokogawa et al. [147] © 2012 American Chemical Society	86
Figure A.5. (a) graphic depicting the hexagonal array consisting of holes with diameter d , period a , and thickness t ; material properties of the superstrate, substrate, and hole can be PDMS or SiO ₂ ; material properties of the grating is galinstan or aluminum; (b) unit cell of the superstrate, hole, and substrate, along with the unit cell of the hexagonal grating	88
Figure A.6. Simulation example for resting state ($a = 370$ nm, $d = 196$ nm, $t = 150$ nm) PDMS-galinstan-PDMS unit cell for (a) $\lambda = 550$ nm (green) wavelength, which shows partial transmission, and (b) $\lambda = 880$ nm (near infrared) wavelength, which shows no transmission	89
Figure A.7. Transmission spectrum obtained from COMSOL [®] simulations using the RF module. (—◆—) transmittance of “resting” (0% strain) producing resonance peak at 540 nm; (—■—) transmittance of “resting” (25% strain) producing a resonance peak at 610nm and 660 nm overlapping the green peak; (—▲—) transmittance of “resting” (33% strain) producing resonance peak at 690 nm; (---■---) transmittance of the model of the original Yokogawa grating design for green light producing resonance peak at 540 nm, matching that of the PDMS-galinstan-PDMS EOT color filter design	90
Figure A.8. Transmission spectra for hexagonal hole array filters optimized for red ($p = 420$ nm, $d = 240$ nm), green ($p = 340$ nm, $d = 180$ nm), and blue ($p = 260$ nm, $d = 140$ nm).© 2012 American Chemical Society	91
Figure A.9. Outline of process to fabricate liquid metal/PDMS EOT color filter	92
Figure A.10. (a) NLOF2020 hexagonal pillar array fabricated using e-beam lithography (step 4) (b) aluminum hexagonal hole array after liftoff (step 6) (c) hexagonal hole array in silicon (step 8) (d) close-up of hole array in silicon	94
Figure A.11. (a) liquid metal nanodroplet formation after e-beam evaporation of elemental gallium on top of elemental indium on silicon nanohole grating (b) edge view of liquid metal nanodroplets	95

LIST OF TABLES

Table 1.1. Material Properties of liquid metal [19], [20].....	5
Table 3.1. Areal surface roughness parameters obtained from AFM software.	56
Table 3.2. Apparent surface free energy of pristine and plasma-treated polymeric surfaces.	59

CHAPTER 1

BACKGROUND AND MOTIVATION

This chapter provides a brief background and motivation for the three studies involving PDMS that will be presented in greater detail in subsequent chapters. The first section provides a background on guided-mode resonance and the motivation for seeking to improve the quality factor. The second section provides background on gallium-based liquid metals and its properties to better understand the motivations of seeking nonwetting polymer surfaces. The fourth section provides background on liquid-metal microfluidic devices and the motivation for a study on the use of CF_4/O_2 plasma-treated polymer surfaces for pneumatics-based liquid metal microfluidics. The last section presents the research objectives and an outline of this work.

1.1 Background on guided-mode resonance and motivation for improving the quality factor of 2D guided-mode resonance gratings

Guided-mode resonance phenomena arise from the interaction of electromagnetic waves with binary slab gratings. A one-dimensional (1D) binary slab grating is a thin film grating consisting of alternating strips of dielectric materials with high (n_{high}) and low (n_{low}) index of refractions, typically with a superstrate (n_{sup}) and substrate (n_{sub}) (Figure 1.1a). A two dimensional (2D) binary slab grating consists of a unit cell, typically a high index of refraction material (n_{high}) of a certain shape (typically a disc with diameter d and thickness t) embedded in a low index of refraction material (n_{low}), that is repeated along two dimensions to create a planar binary grating (Figure 1.1b).

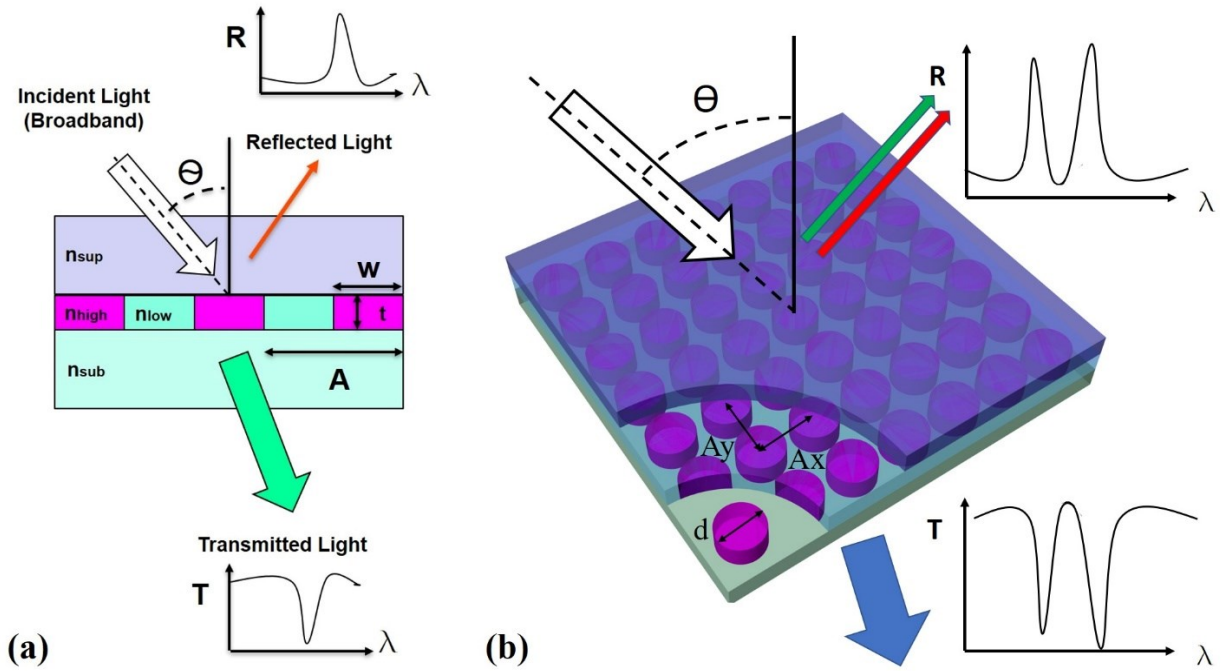


Figure 1.1. Guided-mode resonance phenomenon as broadband light interacts with a binary slab grating waveguide. (a) Diagram depicting a 1D binary grating, (b) diagram depicting a 2D binary (or “solid disc”) grating. Note: “sup” stands for “superstrate” and “sub” stands for “substrate.”

A binary grating slab-waveguide is designed similarly to how fiber optic core with cladding is designed, where the index of refraction is chosen such that:

$$n_{grating, effective}(n_{high}, n_{low}) \geq n_{superstrate}, n_{substrate} \quad (1)$$

These types of binary slab gratings, like the fiber optic cable, have modes for which an electromagnetic wave can be sustained within the high index portion of the grating. Due to the alternating index of refraction of the binary grating, some of these modes are “leaky”, or radiative, causing the grating to have sharp resonance peaks in their reflection or transmission spectrum. By selecting specific grating parameters and materials, one can design a binary slab grating to have a specific resonance peak. The theory and design of such binary slab gratings were developed in 1980s and 1990s by Gaylord and Moharam [1], Wang [2], Magnusson [3] and

Tibuleac [4] and subsequent fabrication of such binary gratings, utilizing those designs [5], [6], have verified the theory and design principles. There is no analytical formula to determine the resonance peaks based on a set of input of grating parameters and material properties. Instead computational methods, such as rigorous coupled waveguide theory (RCWA) [7], [8] and more recently, due to the advances in computing performance, finite element analysis packages, such as COMSOL[®], have been developed and these are employed to determine the position, intensity, and profile shape of resonance peaks. These methods are well-established and have provided excellent match to experimental results for a variety of GMR devices [9], [10].

Within the last two decades, GMR gratings found applicability mostly in optics as filters [7], [11], [12], high contrast gratings (HCGs) in vertical cavity surface emitting laser diodes (VCSELs) [13], [14] or in biotechnology to detect bio-analytes [15]–[17]. More recently, GMR grating found application as a strain sensor by embedding a high index material (titanium dioxide, TiO₂) in a translucent elastomer (PDMS) to create a 2D binary slab grating [18]. The grating design currently has a relatively low quality factor ($Q < 100$), which reduces the range of operation of the device. The typical methods used to improve the quality factor is either by adjusting the grating period (A), the duty cycle within a period (w), and/or pick new materials, which changes the effective index of refraction. However, adjusting any of these parameters also changes the resonance peaks of the gratings. If there is an existing grating design with desired resonance behavior and limited material choices, it becomes a difficult task to improve the quality factor of that design. Thus, there is a need to find a method to improve the quality factor that keeps the resonance intensity and position close to the original and also would not require choosing different materials.

1.2 Background of gallium-based liquid metals and motivation for seeking an understanding of the cause of non-wetting property of plasma-treated polymer surfaces for liquid metals

Gallium-based liquid metals are eutectic alloys of gallium, which have the advantages of being an electrically and thermally conductive liquid at room temperatures as well as a nontoxic alternative to mercury [19]–[21]. There are typically two forms of gallium alloys used in research: Galinstan[®] and EGaIn. Galinstan[®] is a ternary alloy that is a patented and trademarked formula consisting of 50-64.9% gallium, 10-24.9% indium and 10-29%% tin, by weight, and is produced by Geratherm MEDICAL AG (Geshwenda, Germany), although slight variations of the percentages are used in the literature as galinstan (without the trademark) with melting points around -19 °C [22]. EGaIn, a binary alloy consisting of 75% gallium and 25% indium, by weight, was first brought to the attention of researchers through the work of Dickey et al. [19] on the properties of EGaIn in 2008. Since then both versions of the gallium-based liquid metals have been the focus of research in stretchable and soft electronics [23], flexible electronics [24], [25], reconfigurable electronics [26], [27], and microfluidic electronics[28], [29]. In this work, galinstan is the liquid metal used, and the basic properties of the liquid metal are given in Table 1.1.

The surface of gallium-based liquid metals are known to form an oxide skin layer in the presence of oxygen [19], [20], [30], [31]. Lui et al. reported that spontaneous oxidation can occur in an environment with oxygen levels above 1 ppm [20], indicating that any gallium-based liquid metal surface instantly oxidizes in ambient air. The other metals, such as indium or tin, do not form oxides as readily as gallium [31]. Gallium in ambient air can form two types of oxide,

GaO₂ (less stable) GaO₃ (more stable), forming a skin layer about 1.9 to 2.5 nm thick [32], and this oxide skin can change the mechanical properties of the liquid metal [33]. Xu et al. reports that the oxide layer imparts a high yield stress to the fluid making it behave closer to a gel or soft solid [34]. Larsen et al. reports that the oxide skin has viscoelastic properties that are dependent on strain history and stored stress in the oxide layer [35]. Ladd, et al. reports that the oxide skin is robust enough to allow 3D printed liquid metal structures Figure 1.2 [33].

Table 1.1. Material Properties of liquid metal [19], [20]

Liquid Metal	Galinstan	EGaIn	Mercury
Electrical Conductivity (S/m)	$2.3 \cdot 10^6$	$3.4 \cdot 10^6$	$1.04 \cdot 10^6$
Thermal Conductivity (W/m·K)	16.5	-	8.541
Surface Tension (mN/m)	507- 534	624	500
Vapor Pressure (Pa)	$< 10^{-6}$ (500 °C)	-	0.1713 (20 °C)
Melting Point (°C)	-19	15.5	-38.8
Boiling Point (°C)	>1300	2000	357
Viscosity (Pa·s)	$2.4 \cdot 10^{-3}$ (20 °C)	$2.0 \cdot 10^{-3}$	$1.5 \cdot 10^{-3}$ (25 °C)
Density (kg/m³)	6440	6280	13534

One key property reported by nearly all works that concern surface oxidized gallium-based liquid metals is that it readily wets almost every surface and that acids (typically HCl) or bases (typically NaOH) can be used to remove the oxide and dewet the liquid metal from the surface. Dickey et al. was among the first to report the use of a 10% HCl solution to remove the surface oxide layer, with the result that any liquid metal in a microfluidic channel was no longer stabilized by the oxide skin and quickly minimized its volume to form a near perfect spherical droplet that no longer wet the surface [19]. Kim et al. reported on the recovery of nonwetting characteristic of galinstan from exposure to HCl vapors when the oxLM droplet was placed in proximity to a piece of paper impregnated with 37% aqueous HCl solution [30]. Thus, it would

seem continually exposing galinstan to HCl vapor can allow the liquid metal to be nonwetting and allow for liquid metal droplet microfluidics, as reported by Li et al. [36]. However, HCl vapors are incredibly caustic, and it would be beneficial to find other ways to prevent surfaced oxidized liquid metals from wetting a surface.

The nonwetting property of CF_4/O_2 plasma-treated polymer surface was discovered as a side effect of etching PDMS using the CF_4/O_2 plasma [37]. The discovery of the property led to the question of what caused the nonwetting property, as well as whether such a plasma treatment could be extended to other polymers. These questions created the motivation for seeking the cause of nonwetting property of the polymer surfaces when exposed to the CF_4/O_2 plasma.

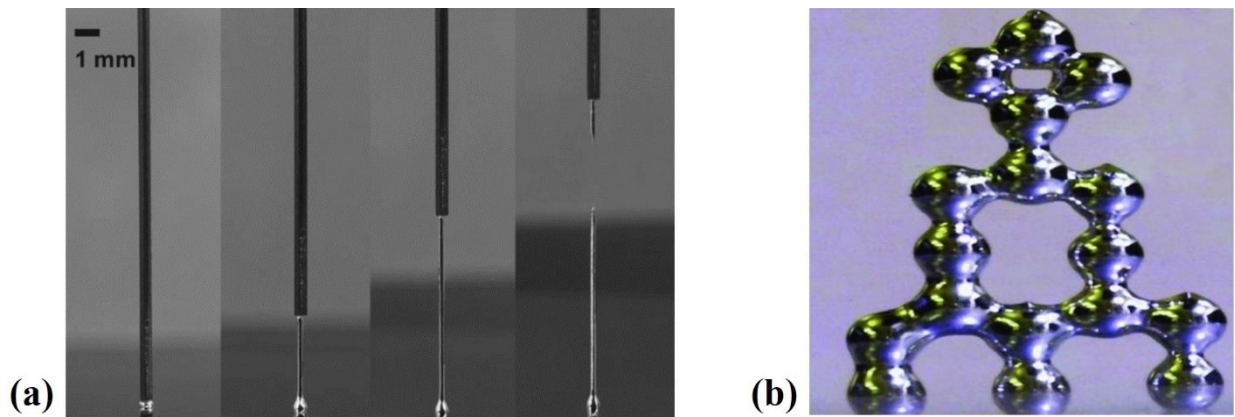


Figure 1.2. Demonstration of the mechanical strength of the surface oxide (a) free-standing liquid metal wires (270 μm), and (b) 3D printed tower of liquid metal droplets, reprinted from Ladd et al. [33] © 2013 Wiley.

1.3 Literature survey on liquid metal microfluidics and motivation for using CF₄/O₂ plasma-treated surfaces for pneumatics-based liquid metal microfluidics

The earliest known report concerning the actuation of a liquid metal droplet is the work by Simon et al., in 1997, of a microrelay that actuates a mercury microdrop using pressurized deionized water all within a 10 μm wide v-groove channel etched out of silicon [38]. The water was heated to create a vapor bubble that increased the hydrostatic pressure enough to move the droplet. In 1998, Lee et al. reported liquid metal actuation using continuous electrowetting, which involves controlling the surface tension of a liquid metal (mercury) microdroplet in a channel filled with electrolyte by placing an electric potential across the channel [39]. Shortly thereafter, the electrostatic actuation, in air, of a mercury droplet on a grounded electrode towards a charged electrode was reported in 2002 [40]–[42].

In 2003, the Office of Scientific and Technical Information (OSTI) published its report [21] on the safety of gallium in the laboratory for magnetic fusion research, which found galinstan to be nontoxic and safer than mercury, and chose galinstan as the liquid metal of choice for research purposes. Since then research in liquid metal microfluidics moved slowly from primarily using mercury to primarily using gallium-based liquid metals.

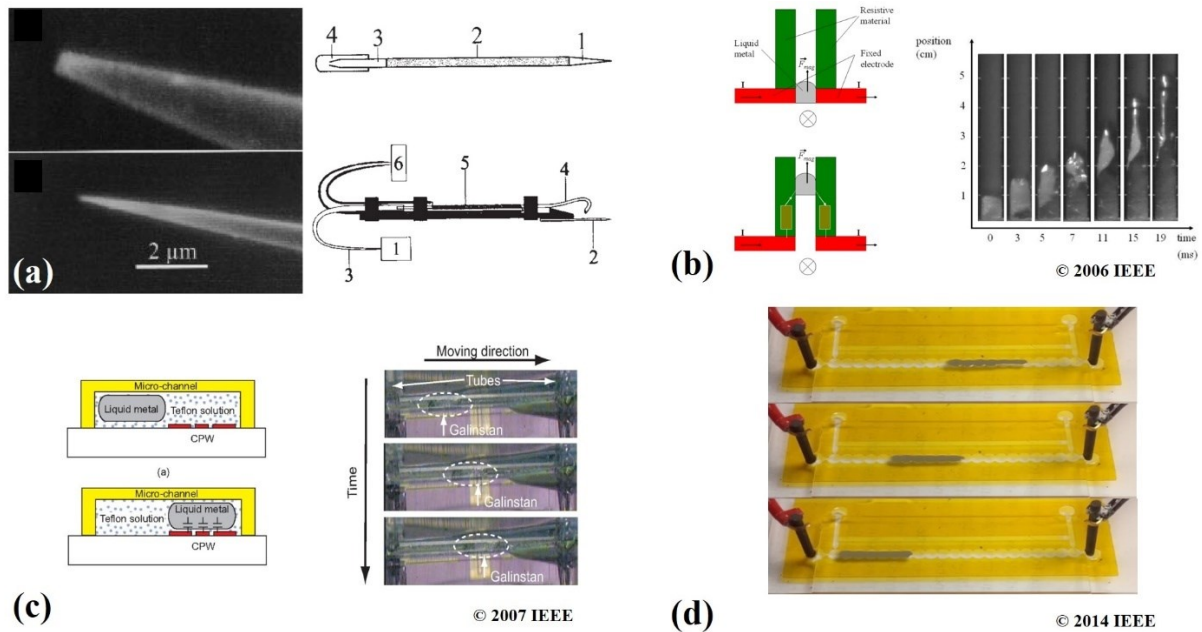


Figure 1.3. (a) Galinstan[®] femtosyringe, reprinted from Ref. [43] © 1999 Nature Biotechnology; (b) Actuation of liquid metal droplet via magnetic repulsion, reprinted from Ref. [44] © 2006 IEEE; (c) hydraulic actuation of liquid metal droplet in Teflon[®] solution reprinted from Ref. [45] © 2007 IEEE; (d) continuous electro-wetting of liquid metal droplet in basic electrolyte solution reprinted from [46], © 2014 IEEE.

Gallium alloy liquid metals first appeared in microfluidics research in 1999 in the seminal paper by Knoblauch et al. [43] about a Galinstan[®] expansion femtosyringe that filled a ~0.6 mm borosilicate glass capillary with the liquid metal and used its thermal expansion properties to inject femtoliter-volume samples into living cells (Figure 1.3a). In 2006, Niayesh et al. demonstrated the actuation of a liquid metal droplet using the magnetostatic repulsion. The liquid metal droplet was placed next to magnetic pole on top of two parallel conductive graphite rods (Figure 1.3b) and when high current was passed through liquid metal droplet via the graphite rods, the current through the droplet generated a magnetic field that was repulsed by the magnet, which move the droplet along the graphite rods. Chen et al. [45], in 2007, actuated a

Galinstan[®] droplet embedded in Teflon solution by pumping in more solution (Figure 1.3c). Gough et al. , in 2014, demonstrated electrical actuation of a galinstan liquid metal slug immersed in an electrolyte (1% NaOH) [46]. The electrical actuation is called continuous electrowetting (CEW) and involves applying an AC voltage at the end points of the solutions (Figure 1.3d). These examples represent actuation of liquid metal in a fluid primarily to prevent the liquid metal from adhering to the channel surface.

In the 2010s, there were developments toward making nonwetting surfaces for liquid metal actuation. In 2012, Kim et al. [47] developed a 3D lyophobic tunnel consisting of fluoropolymer coated micropillars that created a nonwetting surface for a liquid metal droplet (Figure 1.4a). In 2013, Li et al. [47] used HCl vapors that diffuse from adjacent aqueous HCl-filled channels to remove the surface oxide from galinstan droplets in the center channel to prevent it from sticking to the PDMS surface (Figure 1.4b). Li was able to pneumatically actuate the deoxidized liquid metal droplet with air pressure difference. Joshipura et al. [48], in 2018, used a Neverwet[®] coating, which is superhydrophobic due to submicron surface roughness, to create a nonwetting channel for liquid metal (Figure 1.4c) though no pneumatic actuation of droplets was demonstrated. Finally, in 2019, Chen et al. [49] discovered that evaporated gallium creates a coating that is nonwetting to liquid metals and demonstrated pneumatic actuation in an open channel made from gallium thin film coated on a PDMS surface (Figure 1.4d). Compared to a single treatment 120 s CF₄/O₂ plasma treatment to create a nonwetting surface, these methods are considerably more complex. Furthermore, as detailed in Chapter 3, the CF₄/O₂ plasma treatment can be extended to polymers beyond PDMS without the need of a special coating, exposure to

caustic vapors, or additional fabrication steps, giving it a distinct advantage over these other methods.

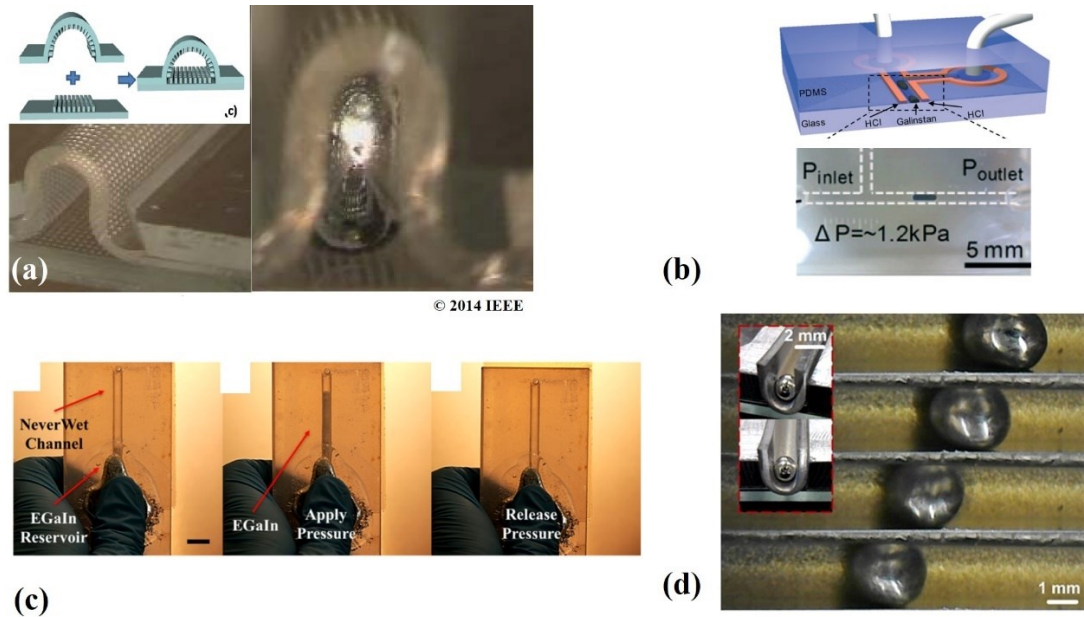


Figure 1.4. (a) 3D lyophobic micropillar tunnel, reprinted from Ref. [47] © 2012 IEEE; (b) Pneumatic actuation of HCl-vapor deoxidized liquid metal droplet in PDMS, reprinted from Ref. [36] © 2014 American Chemical Society; (c) Neverwet coating as nonwetting surface for liquid metal, reprinted from Ref. [48] © 2018 American Chemical Society; (d) Gallium thin film coating on PDMS channel creates nonwetting surface that allows pneumatic actuation of liquid metals, reprinted from Ref. [49] © 2019 American Chemical Society.

There have been several examples of liquid metal droplet generation reported in literature. In 2012, Hutter et al. [50], demonstrated liquid metal droplet generation using aqueous polyethylene glycol (PEG) solution and silicone oil (Figure 1.5a). This method relies on a slip layer of the fluid between the surface of the oxidized droplet and the surface the channel. Khan et al. [51] also reported a similar slip layer formed by water between the oxidized droplet and a glass capillary tube that allowed actuation of the droplet. In 2014, Kim et al. [52] generated deoxidized galinstan droplets by subjecting the liquid metal at the orifice to HCl vapors via an

HCl-impregnated paper surrounding the orifice (Figure 1.5b). Li et al. [36] also used HCl vapors to generate deoxidized liquid metal droplets within a PDMS channel.

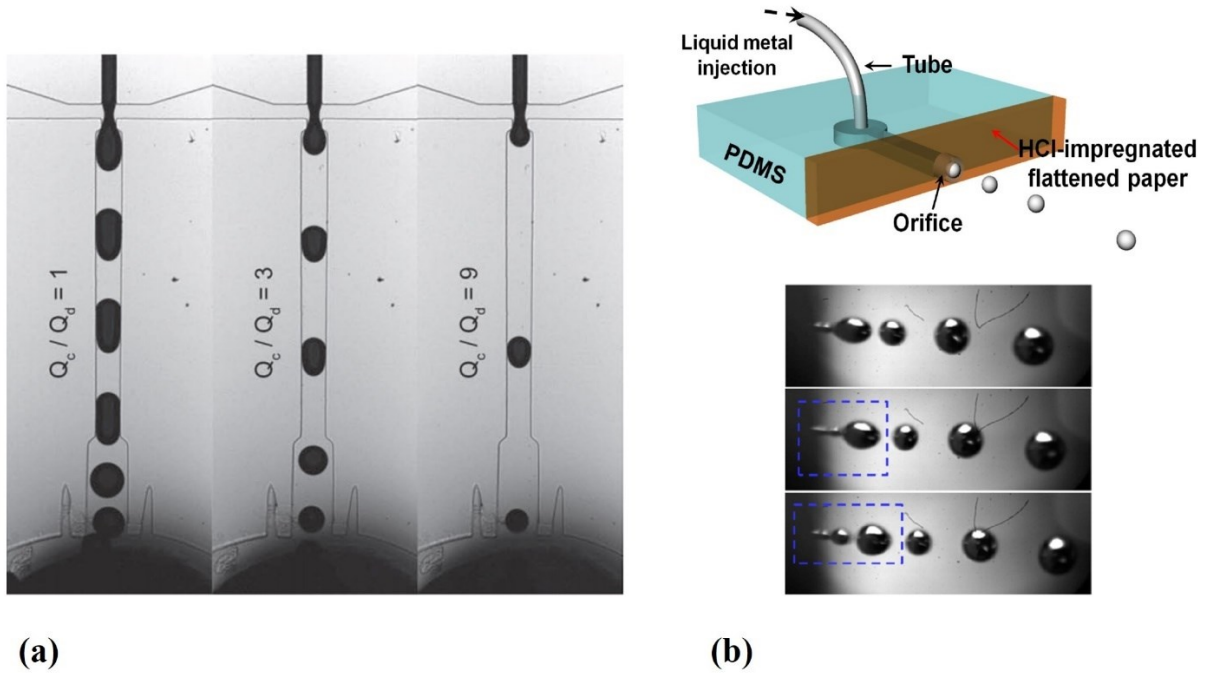


Figure 1.5. (a) liquid metal droplet generation in PEG fluid [50] © 2012 IEEE; (b) deoxidized liquid metal droplet using HCl-impregnated paper. © 2012 IEEE.

Li. et al. [53] is the only paper that could be found that reports successful pneumatic actuation of surface-oxidized liquid metal droplet in a surface roughened PDMS channel. The PDMS channel was roughened by exposure to 89% H_2SO_4 for 90 s to create a nonwetting surface for surface-oxidized liquid metals.

Based on the literature survey above there appears to be very little research in the specific area of pneumatic generation and actuation of surface oxidized liquid metal droplets. The reason for this is, as discussed in Section 1.2, seems to be the adhesive nature of the surface oxide.

Thus, there is motivation, based on the nonwetting property of CF_4/O_2 plasma-treated surfaces,

to do a feasibility study that involves fabricating closed channels made from such nonwetting surfaces and test whether surface-oxidized liquid metal droplets can be generated and actuated within the nonwetting channels.

1.4 Research objectives and chapter outline

For each of the three studies, a research objective was formulated based on their respective backgrounds and motivations, and results from completing those objectives are presented in a single chapter.

For the study on improving the quality factor of GMR gratings, a research objective was formulated to present a simulation study on the effect of a novel design rule on the quality factor of a 2D GMR grating. **Chapter 2** meets this objective by investigating how the design rule affects the quality factor of a previously-studied design for a 2D GMR strain sensor. The chapter first provides a literature survey of GMR gratings and on some methods for improving quality factor. Second, the slotting design rule is explained, the design criteria are chosen, and a new slotted strain sensor design is developed. Lastly, both the original and the new slotted strain sensor designs are analyzed using well-established finite element analysis methods with the results showing a 6-fold improvement in the quality factor while largely retaining the same resonance positions, intensities, and material choices.

For the study on the cause of nonwetting property of CF_4/O_2 plasma-treated polymer, a research objective was formulated to conduct a surface analysis study that seeks to understand why CF_4/O_2 plasma-treated polymers exhibit a nonwetting property towards surface-oxidized gallium-based liquid metals. **Chapter 3** meets this objective by characterizing the surface of the polymers using various surface analysis methods and using the collective results to explain the

cause of the nonwetting property. First, a literature survey of the various methods used to counteract the wetting nature of oxidized liquid metals is provided. Contact angle goniometry, X-ray photoelectron spectroscopy (XPS), and atomic force microscopy (AFM) analyses are used to characterize the nonwetting, chemical properties, and physical properties, respectively, of each polymer surface. Apparent surface free energy analyses were performed to determine the surface energy components of each surface. Each characterization method's results were analyzed separately, and were collectively used to support the conclusion that the surfaces are nonwetting primarily due to the creation of a Cassie-Baxter state due to increase in surface roughness.

For the study on the feasibility of droplet generation and actuation in CF_4/O_2 plasma-treated channel, a research objective was formulated to fabricate and conduct droplet actuation and generation experiments on closed channels made from CF_4/O_2 plasma-treated PDMS.

Chapter 4 meets this objective by providing a study that shows that pneumatic generation and actuation is infeasible due to the role the surface oxide plays in determining the droplets shape within the channel. First, the design choices and experimental setup for droplet generation and actuation is provided. Next, the limitations of plasma-treated PDMS in context of fabrication closed channels are discussed, and modified channel designs for droplet generation and actuation are made based on those limitations. The null results of liquid metal droplet generation and actuation are presented, and evidence indicating that the surface oxide is the primary cause of the null results is discussed.

Lastly, **Chapter 5** summarizes the major results of each study and discusses the future directions of each work.

CHAPTER 2

AXIALLY-ANISOTROPIC HIERARCHICAL GRATING 2D GUIDED-MODE

RESONANCE STRAIN-SENSOR¹

As mentioned in §1.1, guided-mode resonance (GMR) strain sensors are planar binary gratings that have fixed resonance positions and quality factors decided by material properties and grating parameters. If one is restricted by material choices, the quality factor can only be improved by adjusting the grating parameters. This chapter reports on a new method to improve quality factor by applying a slotting design rule to a grating design. It investigates this design rule by first providing a theoretical analysis on how it works and then applying it to a previously studied 2D solid-disc GMR grating strain sensor design to create a new slotted-disc GMR grating design. Finite element analysis is conducted to obtain reflection spectrum results that show the new design produces resonances with at least a 6-fold increase in quality factor over the original design and more axially-symmetric sensitivities. Lastly, we discuss the applicability of the slotting design rule to binary gratings in general as a means of improving grating performance while retaining both material and resonance position choices.

2.1 Introduction

Strain sensing has numerous applications, from concrete structures [54] to biomechanics and robotics [55], in which the displacement of a deformable material under a force needs to be

¹ © 2019 S. Babu and J.B. Lee. This chapter contains portions reprinted with permission from: Babu, Sachin, and Jeong-Bong Lee. "Axially-anisotropic hierarchical grating 2D guided-mode resonance strain-sensor." *Sensors* 19, no. 23 (2019): 5223.

measured. While there are several physical phenomena (piezoresistivity, piezoelectricity, capacitance) that can be used for measuring strain, of which piezoresistivity is currently the dominant form [56], a large number employ optical phenomena, due to smaller device size, low power consumption, high sensitivity, large bandwidth, biocompatibility, and immunity to electromagnetic interference [57]. The typical optics-based strain sensor is the fiber optic strain sensor, of which there are many variants, each of which exploit different optical phenomenon such as attenuation, fluorescence, luminescence, interference, to name a few [57]. Of these, fiber optics using interference, specifically Bragg gratings, are the most prevalent. While fiber Bragg gratings are highly sensitive - capable of microstrain resolution - they have high stiffness that limit range of operation and require direct fiber optic coupling to a detector.

Guided-mode resonance (GMR) is a phenomenon that occurs when electromagnetic radiation incident upon a binary dielectric grating becomes coupled to the leaky (radiative) waveguide modes of that grating [1], [2]. Depending on the grating design, these leaky modes allow resonance bandwidths to be quite sharp, often going from near-unity transmission to near-unity reflection (or vice versa) over a narrow range of wavelengths. The design criteria to achieve such resonances are based on grating parameters and material permittivity choices. Given the wide range of fabrication feature sizes and a large selection of dielectric materials to choose from, GMR devices can be fabricated to operate over a variety of wavelength spectra that are of interest.

GMR theory [3], [4], [58] was initially applied to design all-dielectric high quality factor optical filters out of a single thin film binary grating with a substrate and superstrate. The theory was eventually implemented to fabricate filters that were designed to have reflection (or

transmission) resonance peaks in the visible [11], infrared [7], [59], and giga-hertz ranges [12]. The applicability of GMR to such a wide range of wavelengths is due to the geometric scalability of the grating design parameters [60]. More GMR applications started appearing in areas involving vertical-cavity surface-emitting lasers (VCSELs) [13], [14], tunable filters [61], and microscale optical elements such as absorbers [62] and focusing lenses [9]. GMR has also found application in the area of solar technology, in which gratings are designed to trap incident solar rays [63], [64].

In the area of biosensing, GMR has been used with great success to detect a variety of analytes. Based on the principle that the analyte deposited on the GMR grating will slightly alter the refractive index consequently resulting in a measurable shift in the resonance peak, GMR biosensing can be used to detect extremely small quantities of analyte. It has been used to detect a variety of analytes from pollutants in water [65] to proteins such as biotin [15], biomarkers for ovarian cancer [16] or biomarkers for acute myocardial infraction [17]; it also has been used to detect various solvents such as methanol, ethanol, 2-propanol, and cyclohexane [66].

More recently, the GMR phenomenon was found to be applicable towards creating high-sensitivity pressure and strain sensors [67], [68]. These sensors show great promise for measuring strains of soft materials, such as skin or muscle, offering a larger range of operation and more remote methods of measurement. Unlike most GMR-based devices, which typically use rigid crystalline dielectric substrates, GMR pressure and strain sensors require more compliant substrates to allow pressure or strain sensing over large ranges. PDMS, a polymer with high transmissivity [69], [70] and high elasticity [71], has been used as a compliant substrate for implementing various GMR pressure and strain sensors [72]–[74]. PDMS was initially suggested

as a substrate for microfluidics and biotechnology applications [75] and has since been ubiquitously used in those fields. Thus, there is great advantage in developing GMR-based sensors using this material.

Foland and Lee [18], [76] were the first to design and fabricate a 2D highly compliant GMR strain sensor by embedding a square array of TiO₂ discs in PDMS elastomer. The planar array of TiO₂ discs and PDMS form a binary grating with PDMS as the substrate and air as the superstrate to create a 2D GMR grating. When light from a broadband source is normally incident on the grating, two resonant peaks are reflected back. In order to generate two non-overlapping near-unity reflection peaks, the pitches between the discs along the orthogonal planar axes (Z and Y, in this case) are required to be asymmetric ($\Lambda_Z \neq \Lambda_Y$). If a uniform strain is applied along one axis, say the Z-axis, there is a uniform displacement in the grating pitch whose grating vector is along the Z- axis, and this displacement results in a shift in the resonant peak for that axis, called the Z-axis peak. A strain applied along the Y-axis similarly results in a shift in the Y-axis peak. Considering TiO₂ is a thin film crystalline dielectric with elastic modulus of about 65GPa [77], it has a negligible strain when compared with PDMS, which has an elastic modulus of about 750kPa [78]. Thus, under applied strain, of the grating parameters (Λ_Z , pitch along Z-axis; Λ_Y , pitch along Y-axis; d, disc diameter; t, disc thickness; disc permittivity $n_{\text{TiO}_2} = n_H = 2.35$; and substrate and grating permittivity $n_L = n_{\text{PDMS}} = 1.4$) one should expect only the GMR grating pitches to change. Under Z-axis strain, the Z-axis pitch, Λ_Z , should increase; while under Y-axis strain, the Z-axis pitch, Λ_Z , should increase. Since PDMS is highly compliant, with a Poisson ratio nearly 0.5 [78], the strain applied to one axis does not affect the other much;

though there is some discernable shift. Consequently, the two reflection peaks can be said to move largely independently of each other, allowing simultaneous measurements of axial strains.

The device, however, suffers from a relatively low quality factor ($Q < 100$), and unequal axial sensitivity due to the asymmetric pitch requirement. To improve the quality factor of this sensor, one can either pick different materials or adjust the grating design [3]. For this grating, one cannot choose to pick different materials, since the elastic and optical transparency of PDMS is required for the large strain sensing operating range and GMR, respectively; and an alternative dielectric material with a high and stable index of refraction over the desired wavelength range similar to TiO_2 is hard to find. Thus, one must approach improving the quality factor of this GMR grating strain sensor by adjusting the grating design.

There are not too many parameters to adjust in a 2D square-array-of-discs grating design. Apart from the radius of the discs, the thickness of the discs, replacing discs with a different shape, changing grating pitch, or eliminating layers [79] there is no other parameter one can fine tune. There are several papers that report improving GMR quality factor through adjusting these grating parameters. Fan et al. theoretically investigated reducing the radii of holes of a slab photonic crystal and found the quality factor generally increases by at least a factor of 23 if the radius is reduced to a quarter of the original [80]. However, Pottier et al. reports that while reducing radius does increase quality factor, it also severely reduces the peak intensity [81]. Fattal et al. simulated the role of slab grating thickness on quality factor and found that reducing the thickness of the grating (from 200nm to 10nm) improved the line width significantly, but their result aren't easy to quantify; furthermore, they admit such grating thicknesses would be too difficult to fabricate over large areas with current limitations of technology [82]. Andreani et

al. show that replacing a circular shape with a triangular shape increases the Q-factor by less than 2% [83], essentially a negligible improvement in quality factor. Lastly, increasing the grating pitch is a reasonable method to improve quality factor, however adjusting grating pitch also affects the resonance positions dramatically and can push the grating into resonance-free ranges [3]. If one requires to place resonances in easily-measurable wavelength ranges such as in the visible or NIR regimes, adjusting the grating pitch to achieve higher quality factor is not an option.

One approach to altering grating parameters of GMR gratings not found in literature is to replace the high-index disc itself with a grating. This grating-within-a-grating, or hierarchical grating, approach offers a method to improve the quality factor of a GMR grating through lowering the effective refractive index and provides a new grating design parameter that allows one to control the duty cycle of the sub-grating. By adjusting this duty cycle one can control the proportion (or fill factor) of the sub-grating allowing one to fine-tune the refractive index of the high-index part of the grating while keeping all other aspects of the grating the same. This hierarchical grating approach can be codified as a design rule (called the “slotting design rule”) wherein the high index part of a GMR grating is slotted to form a grating. The hypothesis is that the slotting design rule, when applied to a GMR grating, should improve the quality factor; however there may be unexpected benefits and side effects. In this paper, we apply this slotting design rule to a 2D guided mode strain sensor design by Foland and Lee [18] to create an axially-anisotropic hierarchical 2D GMR grating strain-sensor design and show that it has an improved quality factor (by a factor of 6) and more symmetric axial sensitivity.

2.2 Methods

2.2.1 Design of Slotted-Disc GMR filters

The impetus to use slotted disc design came from trying to understand the role of grating parameters and material permittivities on the quality factor of the resonance peaks. The quality factor, Q , is defined as:

$$Q \equiv \frac{f_r}{\Delta f} = \frac{\lambda_H \lambda_L}{\lambda_r} \frac{1}{\Delta \lambda} \propto \frac{1}{\Delta \varepsilon} \quad (1)$$

where f_r is the resonance frequency; Δf is the resonance width (the full-width half-maximum); λ_r is the resonance wavelength or position; and $\Delta \lambda = \lambda_H - \lambda_L$, where λ_H and λ_L are the wavelengths on either side of the resonance wavelength that are at half the peak reflectance values of the resonance peak.

According to works done by Magnusson et al. and others [2]–[4], [58] the linewidth of a resonance peak, $\Delta \lambda$, is proportional to the modulation index, $\Delta \varepsilon = \varepsilon_H - \varepsilon_L = \sqrt{n_H} - \sqrt{n_L}$, and this relationship is noted on the right hand-side of Equation 1. Thus, one can improve Q , for a given resonance position, λ_r , by lowering the modulation index. One could attempt to lower the modulation index by selecting two different grating materials that are closer in permittivity values or by creating nano-composites [84]. However, this introduces additional steps to the process flow and may require additional tools and testing. With the slotting design rule one would retain the same material choices and only have to alter a binary grating design.

Additionally, changing materials may not always be an option. Some GMR strain sensors are limited to selected materials due to restrictions of resonance wavelength range, and/or requirements of transparency, elasticity, and biocompatibility, such as the 2D GMR strain sensor.

For these reasons, there is value in finding a solution that lowers the modulation index while retaining material choices.

The solution can be found by studying the effective index of refraction of dielectric gratings, which, according to effective medium theory [85], is the average permittivity that can be assigned to the grating for modes with wavelengths much greater than the grating pitch. One can now consider creating a slotted disc by replacing the high index part of the larger grating with a sub-grating composed of alternating slivers of the same high permittivity and low permittivity material. Applying this concept, one can replace the solid TiO₂ discs (Figure 1.1a) with that of a TiO₂/PDMS disc grating or slotted TiO₂ discs (Figure 1.1b). The modulation index can then be tuned over the range of n_L to n_H by adjusting the duty cycle q of the disc grating. Lowering the duty cycle reduces the modulation index, which should result in an improvement of the quality factor. Thus, one can now improve quality factor by having some measure of control on the effective index of refraction of the high-index part of binary gratings.

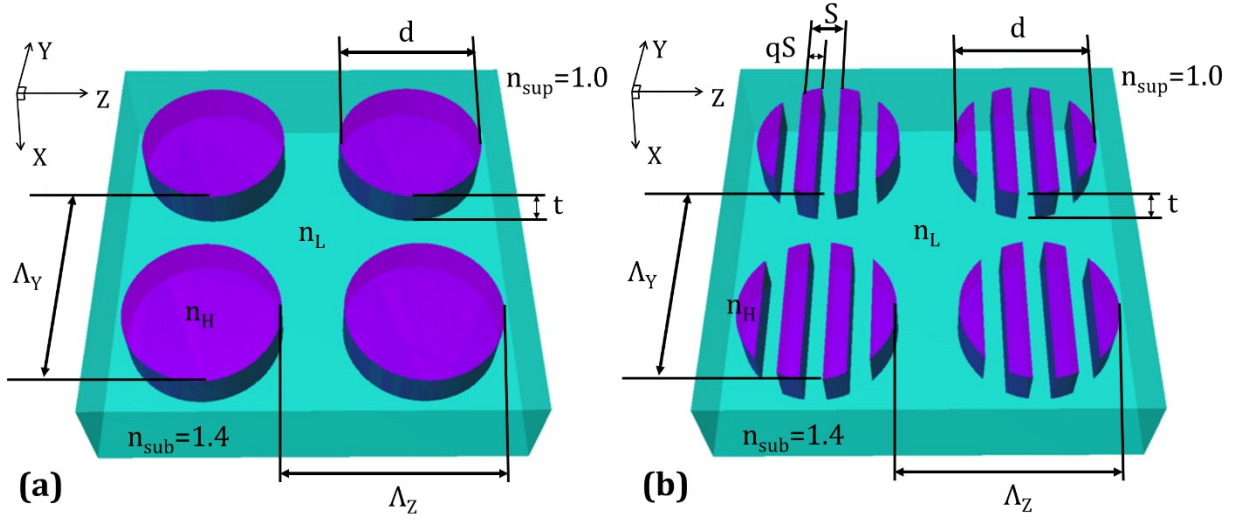


Figure 2.1. Design of 2D GMR grating strain sensor. (a) Solid-disc GMR reflection filter, consisting of discs of TiO_2 embedded in PDMS; $\Lambda_Z=560\text{nm}$, $\Lambda_Y=480\text{nm}$, $t=200\text{nm}$, $d=420\text{nm}$, $n_H=2.35$, $n_L=1.4$, $n_{\text{sup}}=1.0$, $n_{\text{sub}}=1.4$. (b) Slotted disc GMR reflection filter, a grating-within-a-grating device, consisting of slotted-discs of TiO_2 embedded in PDMS; $\Lambda_Z=\Lambda_Y=480\text{nm}$, $t=200\text{nm}$, $d=420\text{nm}$, $S=120\text{nm}$, $q=0.5$, $n_H=2.35$, $n_L=1.4$, $n_{\text{sup}}=1.0$, $n_{\text{sub}}=1.4$.

2.2.2 Axially Anisotropic Refractive Index

Slotted-disc gratings do not have an isotropic index of refraction, like the solid-disc gratings do. Instead, these have an axially-anisotropic index of refraction, and it can be understood by studying effective medium theory (EMT). In EMT, the slotted disc can be treated as a binary subwavelength grating, which has been well studied [86]–[88]. For a binary subwavelength grating with pitch S , fill factor q , and thickness t , with index of refractions n_H and n_L (Figure 2.2), EMT gives the approximate values of the effective indices of refractions to be [87]:

$$n_{\parallel} = [n_H^2 q + n_L^2 (1 - q)]^{1/2} \quad (2a)$$

$$n_{\perp} = [(1/n_H^2) q + (1/n_L^2) (1 - q)]^{-1/2} \quad (2b)$$

where \parallel and \perp denotes the electric field, \mathbf{E} , of the incident light parallel to the binary grating and perpendicular to the binary grating, respectively. In this work, the E-field is always kept perpendicular to the grating vector.

While there are more accurate methods of calculating effective permittivities, Equations 2a and 2b provide estimates accurate enough for designing subwavelength gratings. Lalanne et al. [85] do provide a more accurate method for calculating the effective permittivities using 2D-RCWA (rigorous coupled wave analysis), which was confirmed by Kikuta et al. [89], however it would be quite difficult to describe geometrically-complex 3D structures such as the slotted-disc gratings and implement it in 2D RCWA code.

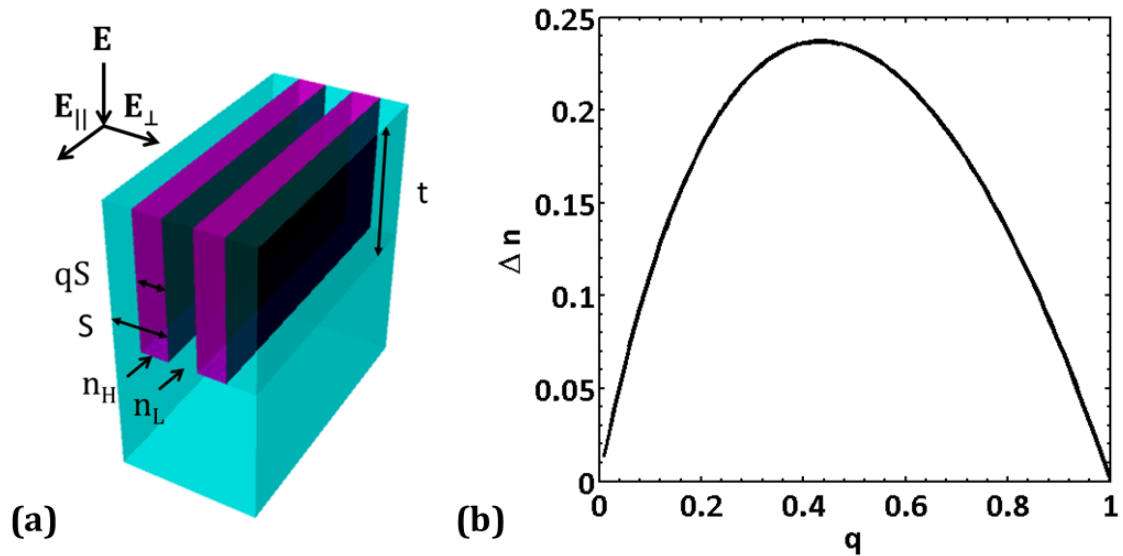


Figure 2.2. (a) Binary grating with PDMS substrate and air superstrate. The grating parameters are $S=120\text{nm}$, $q=0.5$, $n_H=2.35$, $n_L=1.4$, $n_{\text{sup}}=1.0$, $n_{\text{sub}}=1.4$. (b) Plot of $\Delta n = (n_{\parallel} - n_{\perp})$, vs. q ; for $q = 0.5$, $n_{\parallel} = 1.93$ and $n_{\perp} = 1.70$, and $\Delta n = 0.23$.

Lalanne et al. [90] also found that as the thickness-to-wavelength ratio, t/λ , approaches zero the values of the actual refractive index deviates rapidly from those predicted by Equation 2. However, their analyses show that for 2D gratings with t/λ values roughly 0.125 and above, the

effective permittivities are very close to that predicted by Equation 2. For our device, the operating wavelength range is 600nm-1100nm, and t is 200nm, giving us a minimum t/λ ratio of about 0.33, making Equation 2 nearly as accurate as the 2D-RCWA method. For these reasons, there is no need to use the 2D-RCWA method and one can choose to use Equation 2 to calculate effective index of refraction for subwavelength gratings.

Lastly, while Equation 2 is meant for rectangular-shaped binary gratings, it can be used as a rough measure of the expected effective permittivities of the disc grating for the purposes of choosing an optimal q .

2.2.3 Choosing q and S

Figure 2.2b shows how one can choose a Δn based on a choice of fill-factor q . $q = 0.5$ was chosen in order to have a large difference between n_{\parallel} and n_{\perp} (these are the axially anisotropic indices of a slotted disc.). Having such a large difference is needed to create distinct non-overlapping resonance peaks. This is because the closer n_{\parallel} and n_{\perp} are to each other, the closer the resonance positions are to each other, making them harder to resolve. Note that the anisotropic refractive indices ($n_{\parallel} = 1.93$ and $n_{\perp} = 1.70$) are lower than $n_{\text{TiO}_2} = 2.35$, resulting in two modulation indices, $\Delta\epsilon_{\parallel}$ and $\Delta\epsilon_{\perp}$, that are lower than that of the original solid-disc grating, and, as a result of the lowering, should produce resonance peaks that have higher quality factor than the original grating. Note that the $\Delta\epsilon_{\parallel}$ applies to the axial direction parallel to the larger grating (Y-axis) and $\Delta\epsilon_{\perp}$ applies to the axial direction perpendicular to the larger grating (Z-axis) (see Figure 2.1b). For a solid-disc GMR filter device having a disc diameter of 420nm, a slotting pitch $S = 120\text{nm}$ was chosen, and with $q = 0.5$, $qS = 60\text{nm}$. This more than meets the criteria of

having the slotted-disc grating pitch be less than half the wavelength of the incident radiation (600nm-1100nm) such that effective medium theory applies [87].

2.3 Results

2.3.1 3D FEA simulation

From the slotting parameters chosen above, one can now model the solid-disc and slotted-disc 2D GMR gratings using finite element analysis (FEA) to obtain reflection spectra. This method was previously shown to be equivalent to the well-established RCWA method [8], [91] for GMR gratings in Folland et al. [10]. All models of both 2D GMR gratings for this paper were implemented using COMSOL[®]. In the models, a unit cell of the 2D GMR grating was implemented using Floquet periodicity for axial boundary condition matching. The unit cell was set up as a two-port system, with an input port acting as a source of TE (transverse electric) or TM (transverse magnetic) monochromatic light incident along the normal of the 2D grating plane from the top, and an output port of transmitted waves exiting from the bottom (Figure 2.3). After assigning material properties to the grating structures of the unit cell and simulating this two-port system over a range of wavelengths, the $|S_{11}|$ -parameter was retrieved over the range of wavelengths (i.e. the reflectance spectrum of the device).

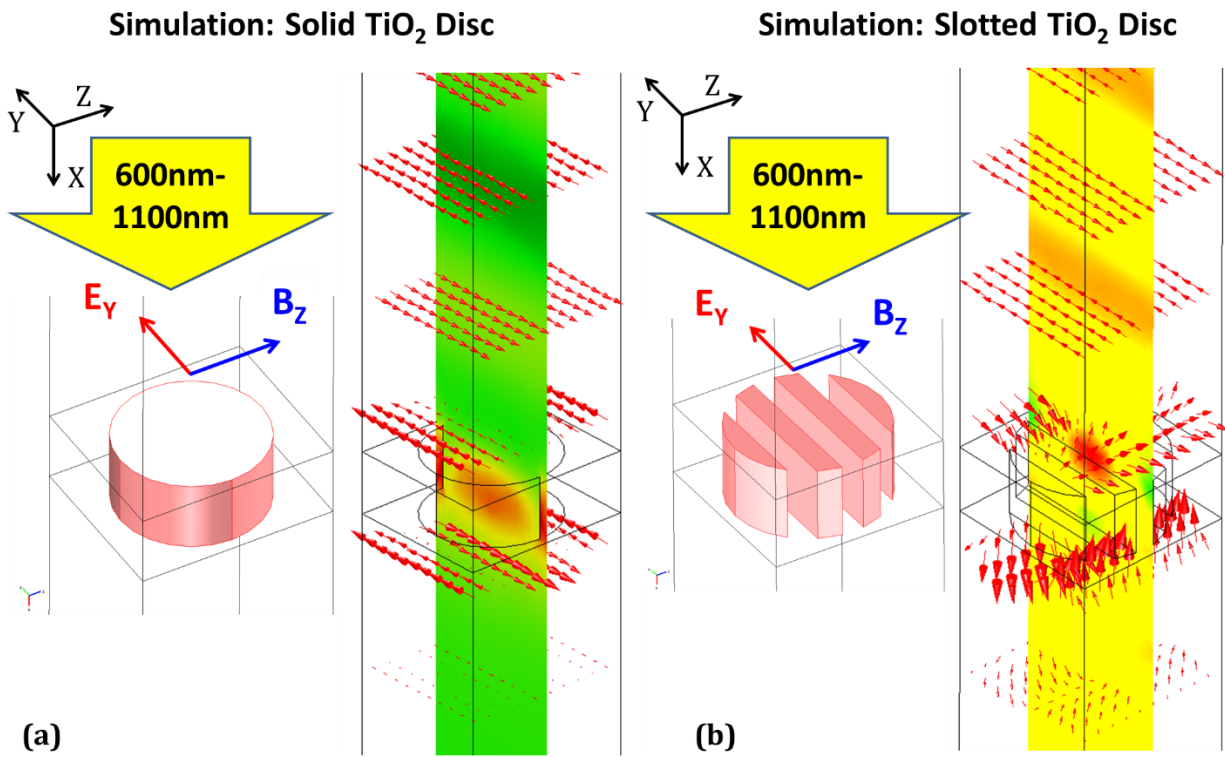


Figure 2.3. COMSOL[®] simulation of (a) solid disc GMR filter device using parameters in Figure 2.1a (b) slotted-disc GMR filter device using parameters in Figure 2.1 b.

Several FEA models were constructed based on the parameters noted in Figure 2.1 caption for both the solid disc and slotted disc devices. Some of these models are rest models, which represent 0% strain, and other are strained models, which represent a unit cell with increased pitch due to the applied strain in either in the Z- or Y-axis direction, but not both simultaneously. In total, ten strained models were created: five models to represent 5%, 10%, 15%, 20% and 25% strains along the Z-axis, and another five to represent strains along the Y-axis. Of the two materials, TiO₂ experiences negligible strain when compared with PDMS. For solid-disc grating under strain, the PDMS surrounding the discs will experience the strain; thus, the only grating parameter affected by strain are the GMR grating pitches (Λ_z and Λ_y). This effect was confirmed by simulation and experiment by Foland et al. [18]. For slotted-disc grating

under strain, both the PDMS surrounding and in-between the slotted-discs will experience the strain; thus the grating parameters affected by strain are the GMR grating pitches (Λ_Z and Λ_Y) and the sub-grating pitch (the duty cycle, q). The strain experienced by PDMS within the slotted-discs were separately simulated using COMSOL[®]'s stress-strain module (Figure 2.4a). The simulations show that the effect of the strain increases the spacing between the slots, an example of which is shown in Figure 2.4b. Using these stress-strain simulations, the new spacings of the slotted-discs for a given strain were calculated and implemented in to the 2-port FEA model for that specific strain (Figure 2.4c, d) as the new sub-grating pitch.

The reflectance spectra from both the rest and strained models are plotted in Figure 2.5 (a-b for solid-disc; c-d for slotted-disc) for only the 0%, 5%, 15% and 25% strains along both Z and Y axes; the 10% and 20% plots were excluded for clarity. Note that 'Y-peak' denotes the peak that shifts under Y-axis strains, and 'Z-peak' denotes the peak that shifts under Z-axis strains.

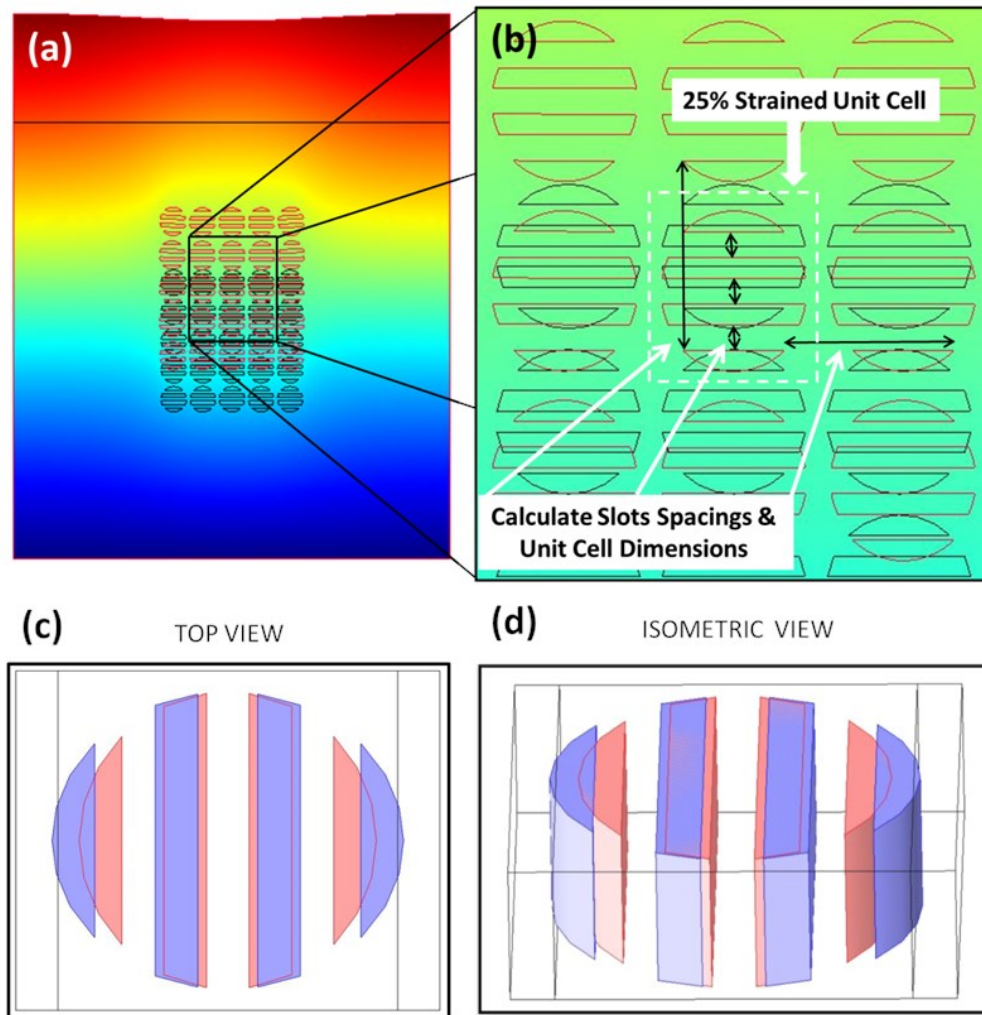


Figure 2.4. (a) COMSOL[®] stress-strain simulation of slotted-disc for 25% Z-axis strain; (b) close-up view of center 25% Z-axis strained unit cell ; resting slotted disc (pink) and 25% Z-axis strained slotted disc (purple) in (c) top view, and (d) isometric view, used for the 2-port FEA model.

2.3.2 Sensitivity Study Results

The sensitivity vs. strain plots were derived from COMSOL[®] simulation reflectance plots for 0-25% strain in steps of 5% strain. The sensitivity was calculated by taking the ratio of the change in resonance peak position to the change in strain. Figure 2.6a presents the results for the

solid-disc GMR grating design; Figure 2.6b presents the results for the slotted-disc GMR grating design.

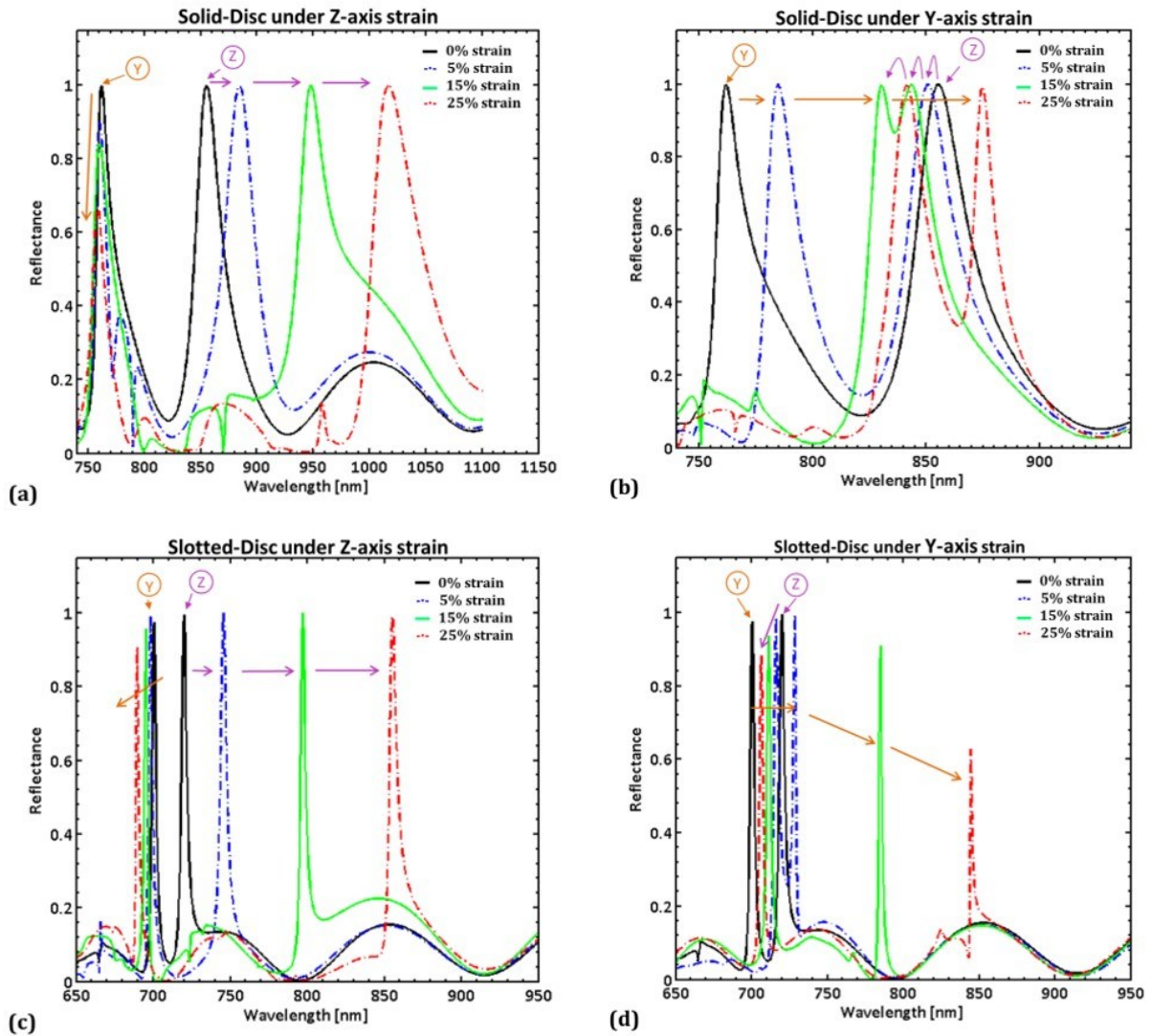


Figure 2.5. Reflection spectrum obtained from COMSOL[®] simulations using the RF module. The ‘Y-peak’ denotes the peak that shifts under Y-axis strains, and ‘Z-peak’ denotes the peak that shifts under Z-axis strains. (a) solid-disc under Z-axis strain; Note the drop in Y-peak reflectance. (b) solid-disc under Y-axis strain; note the Y-peak partially the Z-peak around 15% strain, and move past it at 25% strain. (c) slotted-disc under Z-axis strain; note the drop in reflectivity of the Y-peak. (d) slotted-disc under Y-axis strain; there is a significant drop in Z-peak reflectance.

For solid-disc grating, under Z-axis strain, the Z peak has an average sensitivity of 6.34 nm/% with a standard deviation of 0.31 nm/%, while the Y peak has an average of -0.23 nm/% with standard deviation of 0.12 nm/%. Under Y-axis strain, the Y peak has an average sensitivity of 4.64 nm/% with a standard deviation of 0.25 nm/%, while the Z peak has an average of -0.64 nm/% with standard deviation of 0.22 nm/%.

For slotted-disc grating, under Z-axis strain, the Z peak has an average sensitivity of 5.19 nm/% with a standard deviation of 0.14 nm/%, while the Y peak has an average of -0.35 nm/% with standard deviation of 0.09 nm/%. Under Y-axis strain, the Y peak has an average sensitivity of 5.67 nm/% with a standard deviation of 0.13 nm/%, while the Z peak has an average of -0.59 nm/% with standard deviation of 0.12 nm/%.

2.3.3 Quality factor study results

The quality factor vs. strain plots (Figure 2.6c and 2.6d) were derived from COMSOL[®] simulation reflectance plots for 0%-25% strain in steps of 5% strain. The quality factor is found by using a peak finding algorithm to find the wavelengths of any peaks with above 50% reflectance. After finding the peak wavelengths, the algorithm uses the reflectance spectrum data again to determine the full width half maximum (FWHM), or $\Delta\lambda = \lambda_H - \lambda_L$, at the peak locations. From the peak wavelength and the FWHM one can calculate the quality factor of the peak using Equation 1.

For the solid-disc grating, under Z-axis strain, Figure 2.6c shows the Z-peak quality factor starts close to 30 at 0% strain, and tends to decrease with strain; the Y-axis peak quality factor rises for 5% strain, dropping slightly at 10% strain, falling more due to peak-widening from the overlap with the Z-axis peak at 15% strain (see Figure 2.5a), rising again at 20% strain

as it moves out of overlap, then falling again as its reflectance peak intensity drops, which increases the FWHM. Under Y-axis strain, the Y-axis peak quality factor is 40 at rest and monotonically increases in value from 0% strain to 10% strain. The quality factor then lowers in value due to overlap with the Z-axis peak at 15% strain but rises as it moves out of overlap at 20% strain, eventually increase to the highest value at 25% strain.

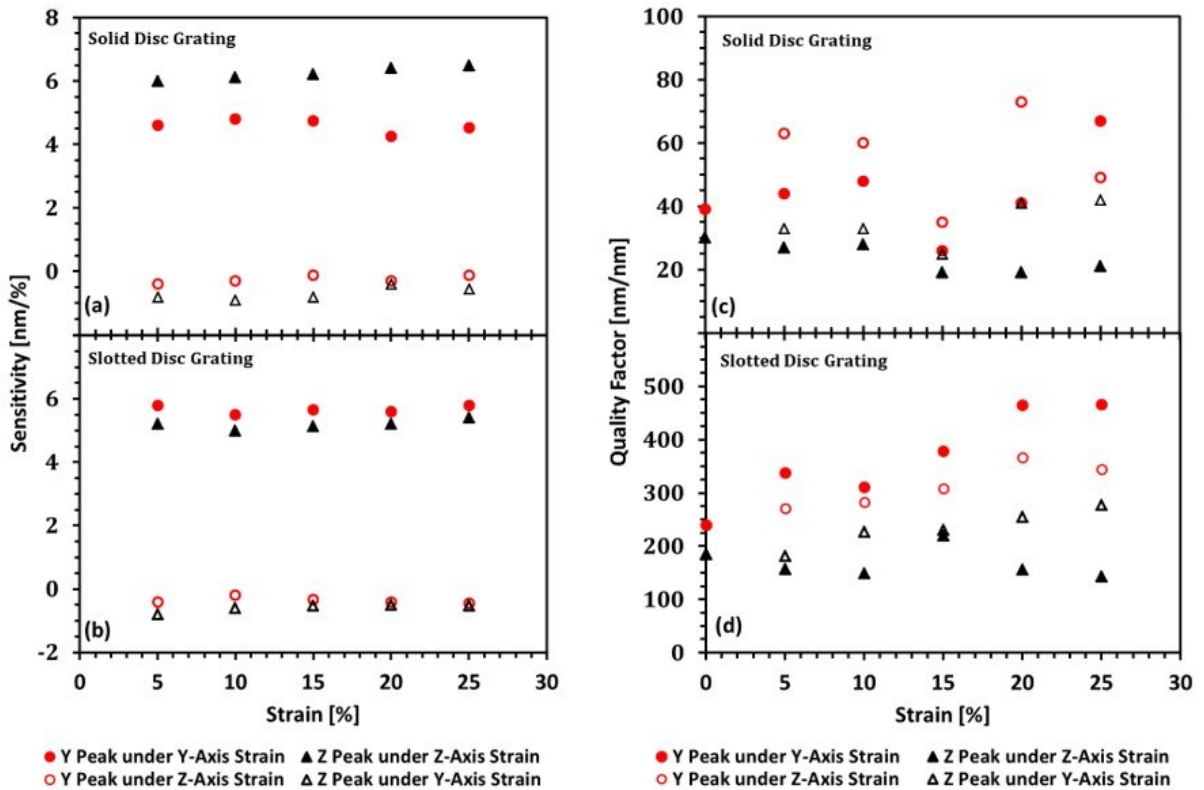


Figure 2.6. (a) Sensitivity vs. strain for solid-disc grating. (b) Sensitivity vs. strain for slotted-disc grating. (c) Quality factor vs. strain for solid-disc grating. (d) Quality factor vs. strain for slotted-disc grating.

For the slotted-disc grating, under Z-axis strain, Figure 2.6d shows the Z-peak quality factor is about 185, around a factor of 6 increase above the quality factor for the same in peak for the solid-disc grating. As strain is increased, the quality factor drops at 10% strain. There is a

sudden rise in the quality factor to 220 at 15% strain before it drops again to below 200 for 20% and 25% strains. The Y-peak, under Z-axis strain, starts, at 0% strain, with a quality factor at 240, about a factor of 6 increase above the quality factor for the same peak for solid-disc grating, and monotonically increases, reaching 302 at 25% strain. Under Y-axis strain, the Y-peak, at 0% strain, has a quality factor of about 240 also, that rises slightly for 5% strain, then falls slightly for 10% strain, before rising in value as strain increases from 10% to 25%. Under the same Y-axis strain, the Z-axis peak quality factor is 185, at 0% strain, lowers slightly at 5% strain, rises slightly at 10% strain, lowers slightly again at 15%, before rising for the remaining strains.

2.4 Discussion

The slotting design rule was hypothesized to improve the quality factor of the 2D GMR grating without having to pick new materials or change grating pitch (to preserve resonance position). The simulation results clearly show that, under no strain, there is at least a 6-fold improvement in the quality factor of all resonance peaks simply by applying the slotting design rule to the solid-disc GMR grating strain sensor design. As mentioned in the theory sections, the slotting design rule works by lowering the effective index of refraction of the high index part of the 2D GMR grating, reducing the modulation index, thereby increasing quality factor. However, there are some additional features that manifest from applying this design rule to the 2D GMR gratings.

Recall that for the solid-disc grating one is required to have an asymmetric pitch ($\Lambda_Z \neq \Lambda_Y$) to generate two distinct resolvable peaks [18]. This is because the high index part of the solid-disc GMR grating has the same index of refraction in both planar-axial directions. If the pitches were kept the same, the resonance would occupy the same position since both axial

directions would have the same modulation index. By applying the slotting design rule to the solid-disc 2D GMR grating, one finds this axial-pitch asymmetry requirement is no longer needed. The slotting rules creates an axially-anisotropic effective index of refraction (i.e. the index of refraction experienced by light traveling along the Z-axis direction is slightly different from that experienced travelling along the Y-axis direction) out of the high index part of the GMR grating. Thus, one can now keep the grating pitches is symmetric ($\Lambda_Z = \Lambda_Y$) and rely on the axially-anisotropic index of the high-index part of the grating to create two resolvable resonance peaks.

When strain is applied, differing behaviors are observed for sensitivity and quality factor. Sensitivity remains largely constant, not varying much in value for strains from 0% to 25% for both solid-disc and slotted-disc gratings. Quality factor, however, is drastically affected by strain. Part of this behavior is due to the close positions of the two resonance peaks, which move in opposite directions under strain, as noted by the arrow in the plots of Figure 2.4 indicating the motion of the peaks under strain. As a consequence, over a small region of strains the peaks overlap, becoming broader, and at some point, overlap completely to become unresolvable. This is the point where the quality factor dips significantly before rising once again as the peaks continue their motion under strain out of overlap. This overlap feature, however, is common to both the solid-disc and slotted-disc 2D GMR grating so cannot be a feature brought about by the slotting design rule. Once past the region of strain that contain the overlap, the quality factor tends to rise for the Y-axis peak under Y-axis strain, and generally drop for the Z-axis peak under Z-axis strain for both solid-disc gratings and slotted-disc gratings. Since this drop in quality factor for the Z-axis peak occurs for both gratings, it also cannot be a feature brought

about by the slotting rule. Thus, while the slotting design rule does increase quality factor overall, it will be affected by other properties and behaviors of the 2D GMR grating strain sensor.

Lastly, one should note that the slotting design rule should be applicable to any grating design that involves binary gratings, which has a high index part and a low index part. The purpose of slotting is essentially to create a parameter by which to have some control over the index of refraction of the high index part of the GMR grating. That parameter is q , which allows control over the duty cycle of the sub-grating that replaces the high index part and also allows a range of values between the high index and low index values. As discussed in the theory part, when q is reduced, this has the effect of lowering the modulation index, which increases the quality factor. This effect is independent of material choice or grating design and is applicable to all binary gratings. Thus, the slotting design rule can be considered as a universal design rule to improve the quality factor of any binary grating.

2.5 Conclusion

A slotting design rule was investigated as a method to improve the sensitivity and quality factor of a 2D solid-disc GMR grating strain sensor. Effective medium theory was utilized to demonstrate the expected improvement in quality factor through reducing modulation index. Grating theory was utilized to show how the slotting design rule can be used as a method for controlling the modulation index, thus providing a means of improving quality factor. The theory was used to design a 2D slotted-disc GMR grating strain sensor. FEA simulations were performed and reflectance spectra were analyzed to show that the 2D slotted-disc GMR strain sensor produces two non-overlapping resonance peaks without needing asymmetric pitches, has

more axially symmetric sensitivities, and yields a 6-fold increase in the quality factor at rest for both resonance peaks. It was also shown, that under increasing strain, the sensitivities remain stable, while the quality factor generally tends to vary dramatically. Lastly, the slotting design rule was shown to be applicable to any binary grating and can be used to improve the performance of such grating in a wide variety of applications.

CHAPTER 3

PLASMA TREATMENT PROCESS TO CONVERT POLYMER SURFACES INTO NON-WETTING SUBSTRATES FOR GALLIUM-BASED LIQUID METALS²

As mentioned in §1.2, liquid metal-based applications are limited by the wetting nature of pristine polymer surfaces towards surface-oxidized gallium-based liquid metals. The work presented in this chapter demonstrates that a 120 s CF₄/O₂ plasma-treatment of polymer surfaces - such as PDMS, SU8, S1813, and polyimide - converts these previously wetting surfaces to nonwetting surfaces for gallium-based liquid metals. Static and advancing contact angles of all plasma-treated surfaces are > 150°, receding contact angles are > 140°, with contact angle hysteresis in the range of 8.2° to 10.7°, collectively indicating lyophobic behavior. This lyophobic behavior is attributed to the plasma simultaneously fluorinating the surface while creating sub-micron scale roughness. XPS results show a large presence of fluorine at the surface indicating fluorination of surface methyl groups, while AFM results show the plasma-treated surfaces have an order of magnitude greater surface roughness than pristine surfaces, indicating a Cassie-Baxter state, which suggests that surface roughness also plays a role in determining the nonwetting property, with surface chemistry making a smaller contribution. Solid surface free energy values for all plasma-treated surfaces were found to be generally lower than the pristine

² This chapter contains portions of text and image from a manuscript currently under peer-review: Babu Sachin, B. Dousti, G.S. Lee, J.B. Lee. "Conversion of polymer surfaces into nonwetting substrates for liquid metal applications." (submitted to ACS journal Langmuir), March 2021.

surfaces, indicating that this process can be used to make similar classes of polymers nonwetting to gallium-based liquid metals.

3.1 Introduction

Eutectic alloys such as eGaIn (75% Ga, 25% In) and galinstan (68.5% Ga, 21.5% In, 10% Sn) have been receiving growing attention in a variety of applications due to their relatively high electrical and thermal conductivity, non-toxicity, and low vapor pressure when compared with other room temperature liquid metals, such as mercury [20]. Compared with solid conductive substrates, such as copper, liquid metals allow the fabrication of conductive structures, at milli [92], micron [93], and sub-micron [94] scales, that can be flexible, stretchable, and deformable while retaining its conductivity. Recent research shows that gallium-based liquid metals have been used to develop soft flexible and stretchable electronics [23], [95], RF (radio-frequency) antennas [27], [96]–[99], switches [100]–[104], frequency selective surfaces [105]–[108], 3D printed structures [33], [52], [109]–[112], and composites [113]–[115].

A common feature of these liquid metal devices listed above is that the liquid metal is not mobile in air. Instead the liquid metal slug is either embedded within the entire volume of the channel or encapsulated in an insulating liquid, with the insulating liquid typically filling the entire volume of the channel [106]. The reason for this is because gallium-based liquid metals are wetting to a variety of materials, and once it fills a channel it is quite difficult to remove [31]. The cause of this wetting property comes from the liquid metal's nature to spontaneously oxidize in ambient air, forming a few nanometers of a thin oxide shell consisting of Ga_2O and Ga_2O_3 [32], and it is this oxide shell that has the property of being strongly adhesive to a variety of materials [31]. This wetting property applies to a wide variety of surfaces, and likely has

hindered progress in applications which require the liquid metal to be nonwetting, such as droplet microfluidics or triboelectric nanogenerators (TENGs) [116]. Thus, developing a quick process that can be applied to a variety surfaces to make these permanently ubiquitously nonwetting to gallium-based liquid metals should help promote the development of applications that take advantage of the nonwetting property.

Several methods have been developed to counter the wetting nature of surface-oxidized gallium-based liquid metals (oxLMs). One method involves removing the oxide layer using caustic agents, such as hydrochloric acid (HCl) [30], [36]. While this method is highly effective, allowing electrochemical actuation methods [117], [118], using such caustic agents will restrict material options, impose extra safety measures, and, due to its reactive and evaporative properties, will need to be replenished over time. Another method involves introducing foreign thin films such as Neverwet[®] [119] or gallium thin films [49], as a coating on elastomeric substrates. Neverwet[®] is suitable for milli-scale patterns, having a reported lowest thickness limit of about 750 μm [119], which limits the feature size of microstructures; additionally, experience has shown that the coating tends to peel from substrates over time. The method of gallium thin film coating allows for ubiquitous nonwetting surfaces; however, the coating is opaque and conductive. This conductive layer may not be compatible with certain electronic and RF applications that require a nonconductive substrate. Multistep fabrication of hierarchical micro/nanoscale structures is another method that has been shown to create a non-wetting surfaces with high contact angles after a C_4F_8 Teflon[®]-like coating is applied on the pillar arrays [29]. However, there is no clear way to apply a similar fabrication method to create such structures on sidewalls for microchannels [47].

Two methods have been reported on making a non-wetting surface for oxLMs through the creation of sub-micron scale roughness over a flat polymer surface. The first method involves the casting of PDMS in black silicon [120] and the second involves exposure of PDMS surface to sulfuric acid [53]. The method of casting PDMS in black silicon to create sub-micron surface roughness is promising, however the process is significantly long (several hours) with no study on whether it can be applied to sidewall features [120]. The method of sulfuric acid exposure by Li et al. can be used to create sub-micron surface roughness by injecting the acid in to pre-made PDMS microfluidic channels and flushing it out with water followed by drying [53]. However, sulfuric acid is yet another caustic material to work with and would require high pumping pressures to inject the liquid into smaller microscale channels, which would risk delamination or bursting of the microfluidic device.

This work shows that exposure to a 3:1 CF₄/O₂ plasma-treatment for 120 s converts polymeric surfaces into visibly smooth, permanent intrinsically non-wetting surfaces for surface-oxidized gallium-based liquid metals. In contrast with other methods, this single step process utilizes no caustic agents or coatings and can be used on a variety of polymers. Four standard polymers, before and after plasma-treatment, are studied by conducting contact angle goniometry along with chemical and physical surface characterizations to determine the underlying cause of the nonwetting property.

3.2 Materials and fabrication

The four polymer materials prepared for plasma-treatment are SYLGARD™ 184 PDMS (Dow Chemical Company, Midland, MI), MicroChem® SU8-2010 (Kayaku Advanced Materials, Inc., Westborough, MA, USA), MicroChem® S1813, and Kapton® tape (3 mils, adhesive on one

side) (DuPont, Wilmington, DE, USA). Each material was chosen as a representative of a class of polymers for which the plasma-treatment could produce similar nonwetting property. PDMS represents the class of silicone polymers, SU8-2010 represents the class of negative photosensitive resists, S1813 represents the class of positive photosensitive resists, and Kapton[®] tape represents polyimides.

To create pristine samples, each liquid polymer was spun on a bare 3" <100> silicon wafer at 3000 rpm for 75 sec. The PDMS polymer was prepared by mixing the pre-polymer and polymerizing agent from the silicone elastomer kit using the standard 10:1 ratio by weight of pre-polymer to polymerizing agent, which was degassed in a vacuum chamber for 1 hour; the mixture was used within 10 min after vacuum desiccation. The other liquid polymers (SU8, S1813) required no prior preparation. After spinning, the PDMS on wafer and was baked in a 95 °C oven for 10 mins. The SU8-2010 on wafer was baked on a 115 °C hotplate for 1 min, and subsequently exposed to i-line (365nm) UV light (900W) for 2 min to ensure crosslinking. The S1813 on wafer was baked on a 115 °C hotplate for 1 min. S1813 was left unexposed. Sections of the polyimide tape were cut and affixed on to bare silicon wafer.

Half of the pristine samples were treated to 120 s of a 3:1 ratio CF₄/O₂ plasma (250 W, 100 mTorr, 3 sccm O₂, 9 sccm CF₄) using a Trion Sirius-T2 RIE Etcher (Trion Technology, Tempe, AZ, USA) to create plasma-treated samples. Enough pristine and plasma-treated samples were created to allow for single measurement of a sample surface. No sample subjected to a measurement was reused.

3.3 Experimental methods

3.3.1 Contact angle measurements

The Drop Shape Analysis System DSA30B (KRÜSS GmbH, Hamburg, Germany) was used to make contact angle measurements using their DSA4 image analysis software. The liquid metal used is galinstan (Ga 68.5%, In 21.5%, Sn 10%) (Changsha Rich Nonferrous Metals Co., Ltd., Hunan, China). The liquid metal was loaded into a SY3601 syringe (4.706 mm diameter, 1.0 mL, Henke Sass Wolf GmbH, Tuttlingen, Germany) with a KRÜSS NE47 needle (0.7mm OD, 38mm long, blunt polypropylene needle). Static and dynamic contact angles of each surface was characterized by dropping ~ 8 μL liquid metal droplets, naturally oxidized in ambient air, on to each surface, which lay on the horizontally leveled stage of the DSA30B system. The capillary length ($k^{-1} = \sqrt{\gamma/\rho g}$) for liquid metal is 2.8 mm, which requires liquid metal droplets to have a radius less than 2.8 mm to avoid the effects of gravity. An 8 μL drop has roughly a 0.9 mm radius, which meets the requirement. Picture or video recordings were made of each droplet, and the DSA4 software's image processing algorithm was used to automatically detect the left and right contact angles and take an average; this average is treated as the contact angle measurement.

Solid surface tension measurements of both the pristine and plasma-treated polymer surfaces were determined from static contact angle measurements using two standard liquids, deionized water (Item# R-950-1, CAS# 7732-18-5, PTI Process Chemicals, Ringwood, IL, U.S.A.) and diiodomethane (CAS# 75-11-6, Sigma, Saint Louis, MO, U.S.A). The static contact angles for 4 μL of deionized water droplets for 4 μL diiodomethane droplets on the polymer

surfaces were measured using the ramé-hart manual goniometer (Model# 50-00-115, ramé-hart, Mountain Lakes, New Jersey, U.S.A.). The capillary length is 2.7 for deionized water and 2.3 for diiodomethane. A 4 μL drop has roughly a 0.7 radius, which meets the requirement for avoiding the effects of gravity when measuring contact angles.

Contact angle (CA) measurements were performed on all four materials, for both pristine and plasma-treated samples, by recording a set of five independent measurements for static, advancing, and receding contact angles. The average and standard deviation of these five measurements were used to estimate the mean contact angle value and the error on it, respectively. No sample surfaces were reused after a single-contact measurement. Only center sections of Si wafers (away from edges), which have the most uniform thickness and uniform plasma exposure, were used. These protocols were followed to ensure that each data point represented the same experimental setup as much as possible.

3.3.2 Surface characterization methods

Chemical characterization of the surface was determined using the PHI VersaProbe II XPS system (Chigasaki, Japan) that has a monochromatic aluminum K Alpha X-ray radiation source (1486.6 eV, 50.2 W) with beam diameter 200 μm at 45° angle in FAT mode. The pass energy for the survey spectrums was 187.85 eV; while the pass energy for high resolution spectra was 23.50 eV. Since the sample surfaces are nonconducting polymers, automated neutralization was used (2 V, 22.0 μA). MultiPak v9 software was used to perform the peak shift-correction on a sample's spectrum to the reference C 1s binding energy (BE) of 284.8 eV; the software was also used for deconvolution analysis of high resolution C 1s peaks. Physical characterization was performed using atomic force microscopy (AFM) by the Jupiter XF Atomic Force Microscope

system (Asylum Research, Santa Barbara, CA), with an AC160-TS cantilever tip, in tapping mode. A 5 μm x 5 μm section was scanned to create images with 256 x 256 pixels for the plasma-treated materials, which has sub-micron features, and images with 512 x 512 pixels for the pristine materials, which has nanometer features. From each 5 μm x 5 μm section, an artifact-free 3 μm x 3 μm region was selected.

3.4 Results and discussion

3.4.1 CF₄/O₂ plasma exposure time study for PDMS³

The effect of duration of CF₄/O₂ plasma exposure on the nonwetting property of PDMS, as indicated by contact angle, was studied. Several PDMS slabs (SYLGARD™ 184 Silicone Elastomer Kit using the standard 10:1 ratio), roughly 105mm long 35mm wide, and 2mm thick, were exposed to a 3:1 ratio CF₄/O₂ plasma (at 250 W, 100 mTorr, 3 sccm O₂, 9 sccm CF₄) for durations of 0 s, 60 s, 120 s, 900 s, and 3,600 seconds. The KRÜSS Drop Shape Analysis System DSA30B (Hamburg, Germany) was used to measure all contact angles using their DSA4 image analysis software. The syringe used was a SY3601 syringe (4.706 mm diameter, 1.0 mL, Henke Sass Wolf GmbH); the liquid metal used was galinstan (Ga 66.5%, In 20.5%, Sn 13%; Smart-Elements GmbH); the needle used for the measurements was the KRÜSS NE47 needle with polypropylene inner tubing with a stainless-steel metal jacket (0.7 mm outer diameter). The resulting data are present Figure 3.1.

³ From Babu, Sachin, and Jeong-Bong Lee. "Plasma-Treated PDMS as Intrinsically Non-Wetting Surface for Gallium-Alloy Liquid Metal Microfluidics." 2020 IEEE 33rd International Conference on Micro Electro Mechanical Systems (MEMS). IEEE, 2020. © 2020 IEEE.

Initially, all plasma-treated PDMS slab exhibited non-wetting property immediately after plasma treatment. However, over a period of days, the slabs with < 120 s exposure time lost their non-wettability property; the slabs with > 120 s exposure retained their nonwetting property permanently. The samples were characterized 7 days after plasma treatment, by which time the transient property was assumed to have stabilized to either a wetting or a nonwetting state. However, samples prepared 6 months later indicated this assumption was incorrect. New 60 s samples did not always return to a wetting state even after 7 days. Instead random areas reverted to a nonwetting surface, while the remaining portions retained the nonwetting property. It seems that plasma treatment under 120 s has unpredictable wetting characteristics from region to region that change at different times. These results indicate that only > 120 s CF_4/O_2 plasma treatment can be trusted to reliably convert a flat polymer surface to a nonwetting surface to oxLM.

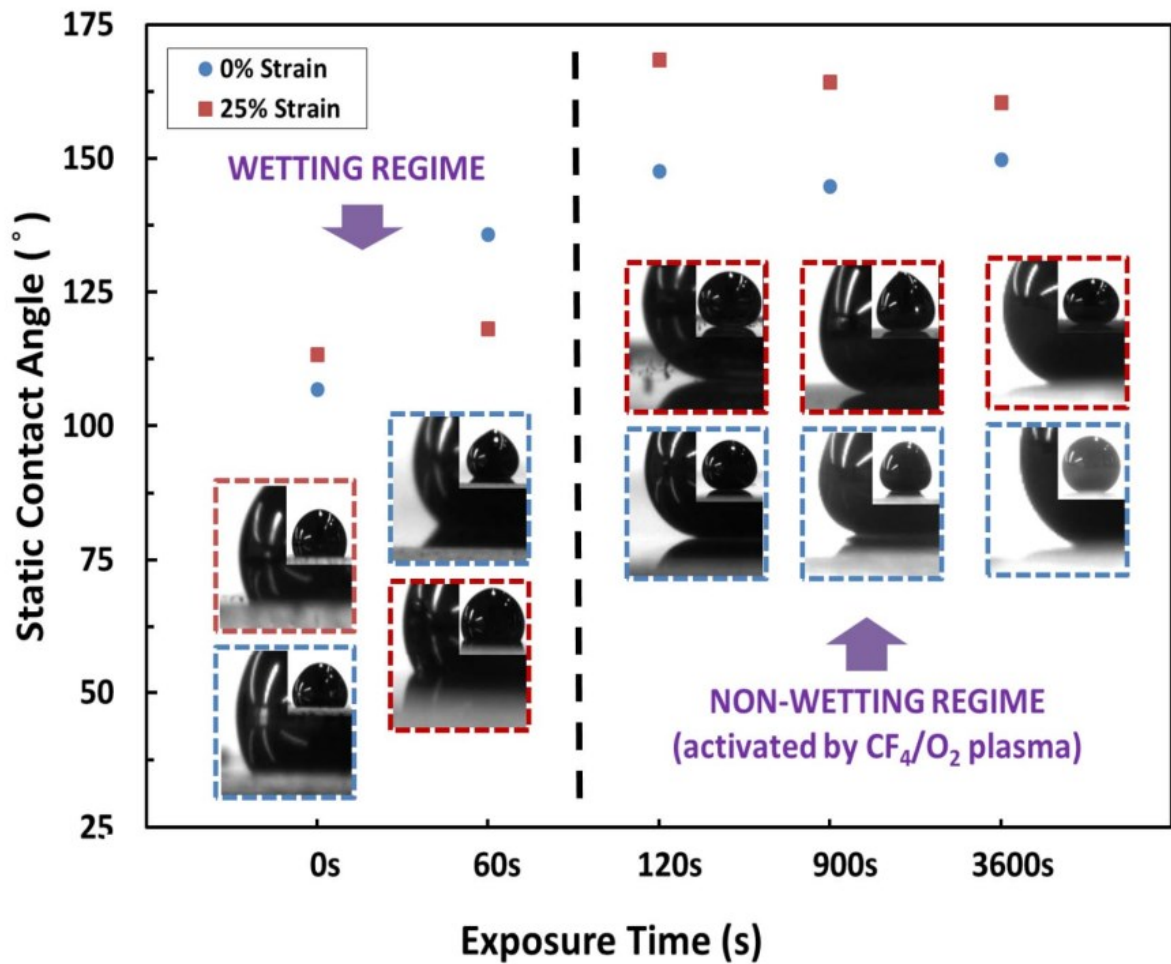


Figure 3.1. Static contact angle vs. exposure time to CF_4/O_2 plasma treatment from Babu et al. [37]. © 2020 IEEE. The authors measure the contact angles using $8\mu\text{L}$ galinstan droplets in ambient air, for both resting (solid circle) and 25% strained (solid square) 2 mm thick PDMS slabs.

Contact angle measurements for different exposure times were also produced for PDMS under 25% strain. The results show that the 25% strain tends to help increase the contact angle. Since the plasma treatment causes surface roughness, it is reasonable to treat the surface as a composite material consisting of air and plasma-treated PDMS. When strain is applied the gaps between peaks increases, in effect air become a larger portion of the composite than the plasma-

treated PDMS, leading to a lower effective surface energy, which leads to a larger contact angle. There is one discrepancy where the contact angle for the strained 60 s plasma-treated PDMS is lower than that of the resting 60 s plasma-treated PDMS (Figure 3.1). Since the DSA4 image processing software is fairly accurate, this is unlikely a measurement error. Instead, it seems likely that the unpredictable wetting states created by the 60 s plasma treatment allow a wide range of contact angles, and that the contact angle measurement for strained and unstrained 60 s plasma-treated PDMS may have an overlapping range of values.

3.4.2 Contact angle measurements of O₂ plasma-treated polymers

The effect of pure oxygen plasma on the nonwetting property was studied for photoresists SU8-2010 and S1813. The study indicates that a 60 s O₂ plasma treatment can convert photoresist surfaces into nonwetting substrates for liquid metal applications. Static contact angles $> 150^\circ$ and contact angle hysteresis (CAH) $< 13^\circ$ of the plasma-treated surfaces indicate a superlyophobic wetting state against the liquid metal.

To fabricate these surfaces, half of the wafers were kept unaltered to represent the “pristine” photoresist. The other half was treated to 60 s oxygen plasma (100 mTorr, 250 W, 12 sccm) to represent the “plasma-treated” photoresist. All wafers-halves were further cut to 1 cm wide sections for use in contact angle goniometry. The resulting static contact angle data is presented in Figure 3.2 and the dynamic contact angle data is presented in Figure 3.3.

The results of Figure 3.2 indicate a high contact angle ($> 150^\circ$) indicated that the O₂ plasma treatment produces a surface that is lyophobic toward liquid metal, sufficient to indicate that it is nonwetting. This is supported by the low contact angle hysteresis (CAH $< 13^\circ$) that

Figure 3.3 shows. The case of this nonwetting property is due solely to the increase in surface roughness, and the formation of a Cassie-Baxter state between the surface and the plasma-treated material. The oxygen plasma treatment did not work for PDMS or polyimide (KAPTON[®]) tape, likely due to the inability of the plasma to etch these polymers well enough to generate the type of surface roughness required to create the nonwetting property.

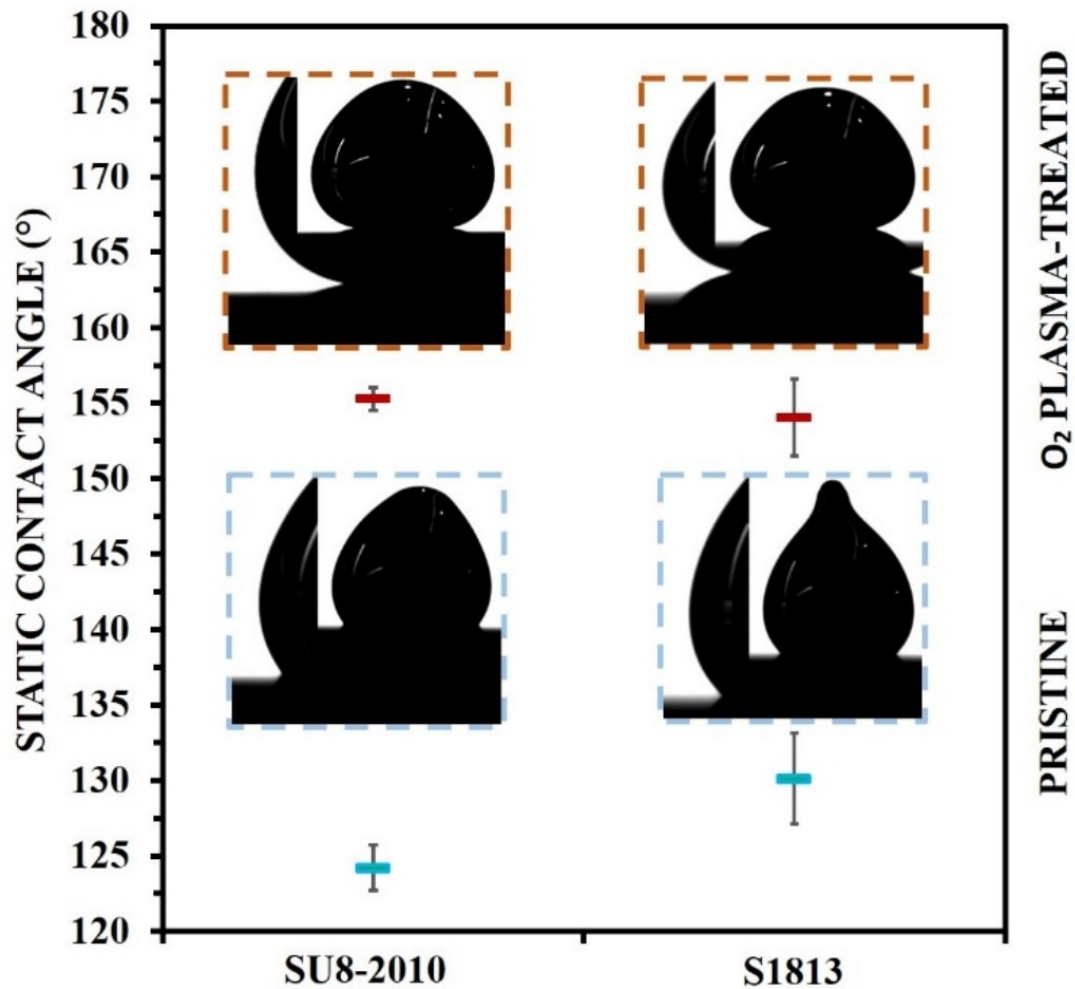


Figure 3.2. Static contact angle measurements of liquid metal droplets on SU8-2010 and S1813, for pristine (green data points, bottom inset figures) and 60 s O₂ plasma-treated (red data points, top inset figures).

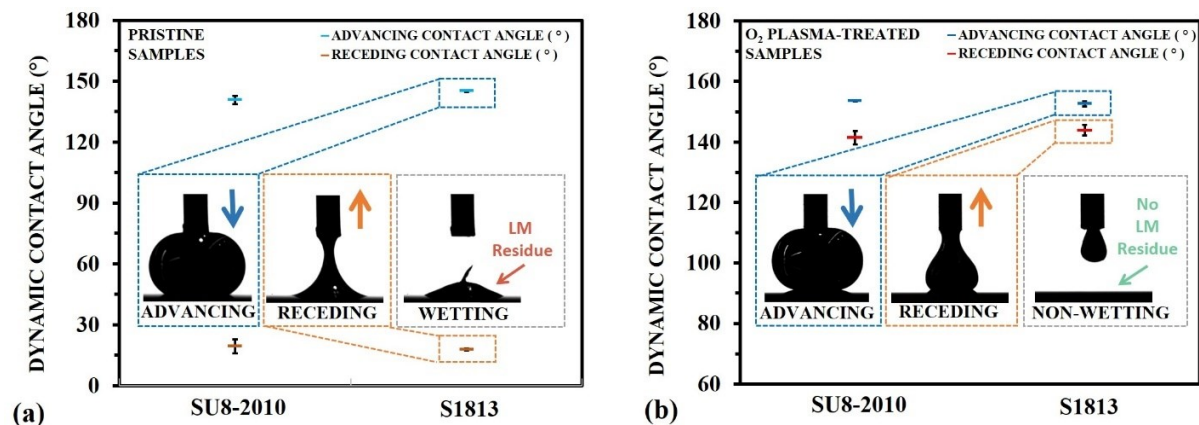


Figure 3.3. Dynamic contact angle measurements of liquid metal droplets on SU8-2010 and S1813, for pristine (left plot) and 60 s O₂ plasma-treated (right plot) surfaces.

3.4.3 Contact angle measurements for CF₄/O₂ plasma-treated polymer

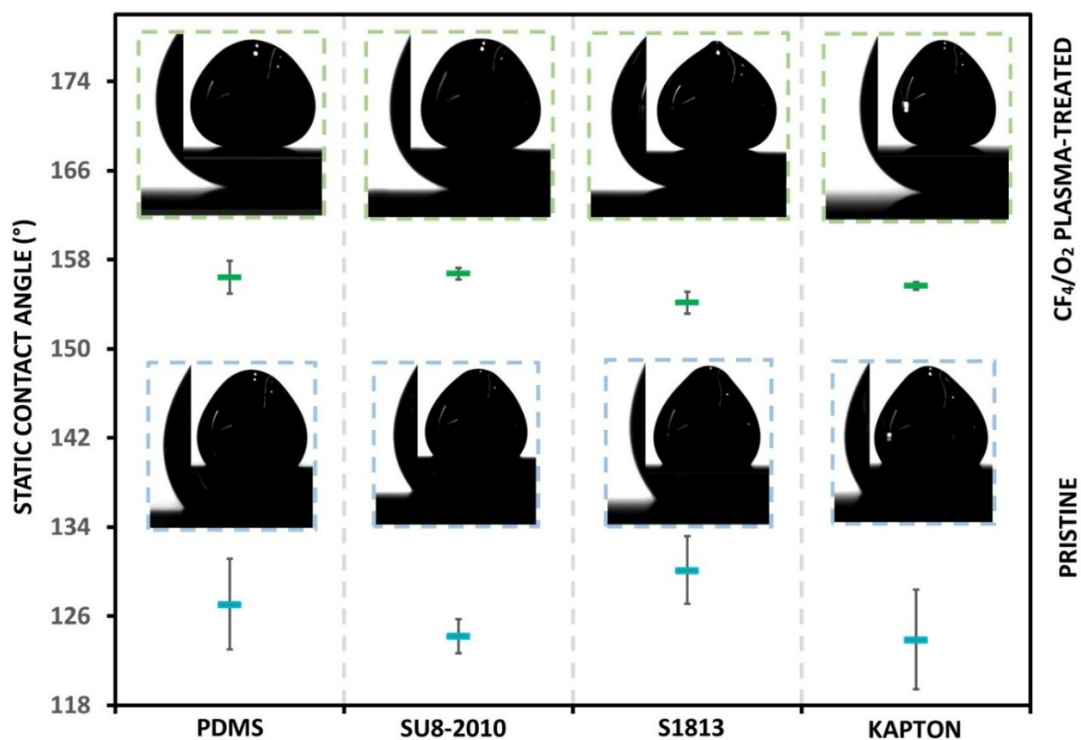


Figure 3.4. Static contact angle measurements of CF₄/O₂ plasma-treated (top) and pristine (bottom) polymer films on silicon wafer using surface-oxidized galinstan droplets. 8 μ L liquid metal droplets were used; all droplet radii are \sim 2 mm.

Static contact angle (SCA) results of 8 μL of sessile surface-oxidized galinstan droplets are shown Figure 3.4. For pristine materials, the CAs range from $123.9 \pm 4.5^\circ$ to $130.1 \pm 3.0^\circ$, a total range of 13.7° (Figure 3.4, bottom). The wide range of angles indicates the different surface chemistry of each material in determining a contact angle. The high contact angles ($> 90^\circ$, typically considered lyophobic) are due to the high surface tension of the liquid metal encased in the oxide skin. For the plasma-treated materials the CAs range from $154.1 \pm 1.0^\circ$ to $156.7 \pm 0.5^\circ$, a range of 4.0° (Figure 3.4, top), demonstrating that all the surfaces are superlyophobic to oxLM.

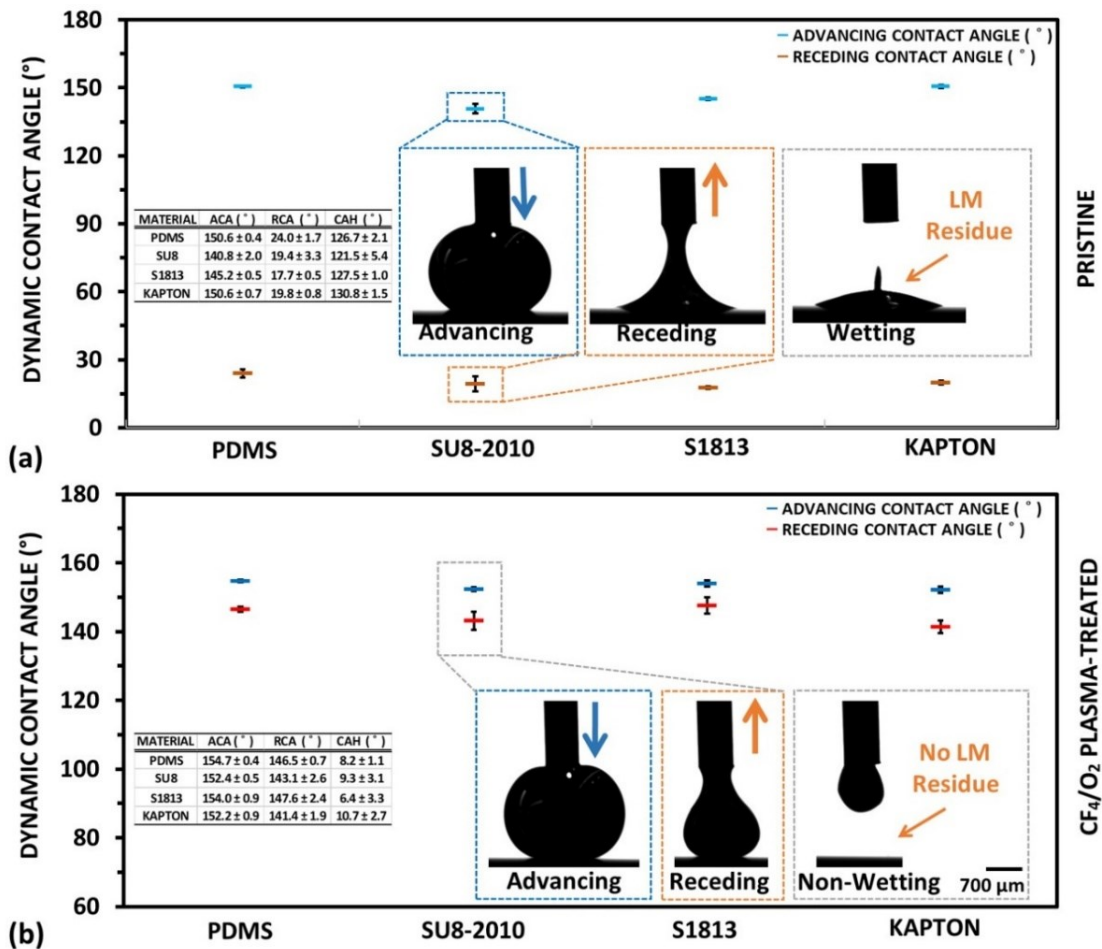


Figure 3.5. Dynamic contact angle measurements for (a) pristine and (b) plasma-treated materials. The vertically downward arrow indicates infusion, the vertically upward arrow indicates withdrawal; LM stands for “liquid metal”.

Dynamic contact angle results are shown in Figure 3.5. For each measurement, the needle was placed 2 mm above the surface. 5 μL of galinstan was infused to form an advancing contact angle line, and 8-15 μL was withdrawn to form a receding contact angle. The liquid metal was withdrawn further to allow it break contact with the surface to test for the nonwetting property by checking if it left any residue. For pristine samples (Figure 3.5a) the advancing contact angles (ACAs) range from $140.8 \pm 2.0^\circ$ to $150.6 \pm 0.7^\circ$, a total range of 12.5° ; the receding contact angles (RCAs) range from $17.7 \pm 0.5^\circ$ to $24.0 \pm 2.1^\circ$, a total range of 8.9° ; the contact angle hysteresis (CAH) ranges from 121.5° to 130.8° , which indicates a highly wetting surface, as demonstrated by the liquid metal residue left on the surface (Figure 3.5a, “wetting” inset). For plasma-treated samples (Figure 3.5b) the advancing contact angles (ACAs) range from $152.2 \pm 0.9^\circ$ to $154.7 \pm 0.4^\circ$, a total range of 3.8° ; the receding contact angles (RCAs) range from $141.4 \pm 1.9^\circ$ to $147.6 \pm 2.4^\circ$, a total range of 10.5° ; the contact angle hysteresis (CAH) ranges from 6.4° to 10.7° , which indicates a highly non-wetting surface, as indicated by the lack of liquid metal residue on the surface (Figure 3.5b, “non-wetting” inset.)

3.4.4 Surface chemistry

XPS measurements were conducted on all samples to determine the changes in surface chemistry that results from CF_4/O_2 plasma-treatment. Figure 3.6, a and b, show the survey for PDMS and SU8, respectively; XPS surveys for S1813 and Kapton are provided in Figure 3.7, a and b, and show similar results. For all surveys, the C 1s, O 1s, F 1s, peaks, if present, are identified; the O KLL and F KLL Auger lines are also identified for clarity. Si 2s and Si 2p peaks are identified for the silicone polymer.

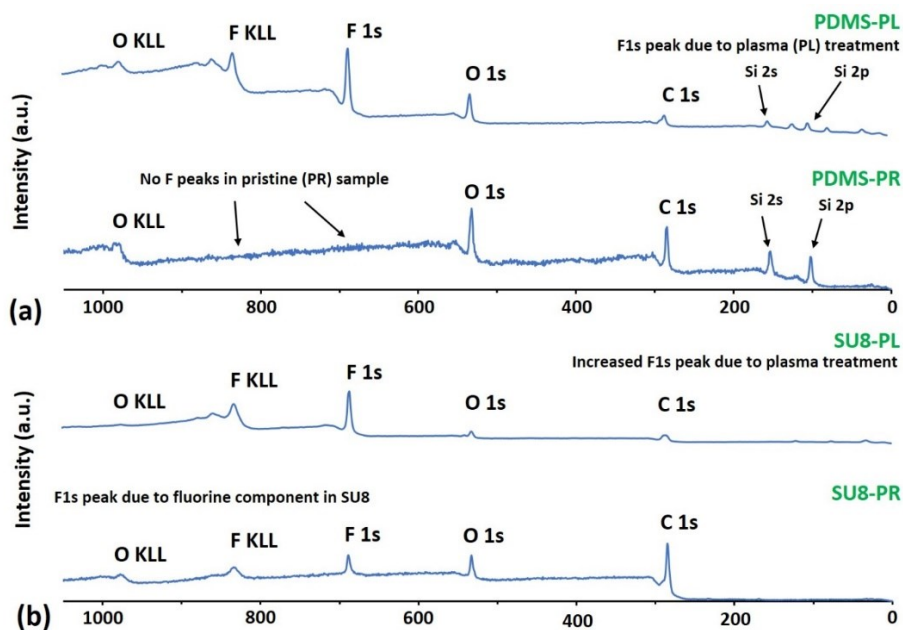


Figure 3.6. XPS survey of (a) plasma-treated (PDMS-PL curve) and pristine (PDMS-PR curve) PDMS; and (b) plasma-treated (SU8-PL curve) and pristine (SU8-PR curve) SU8-2010.

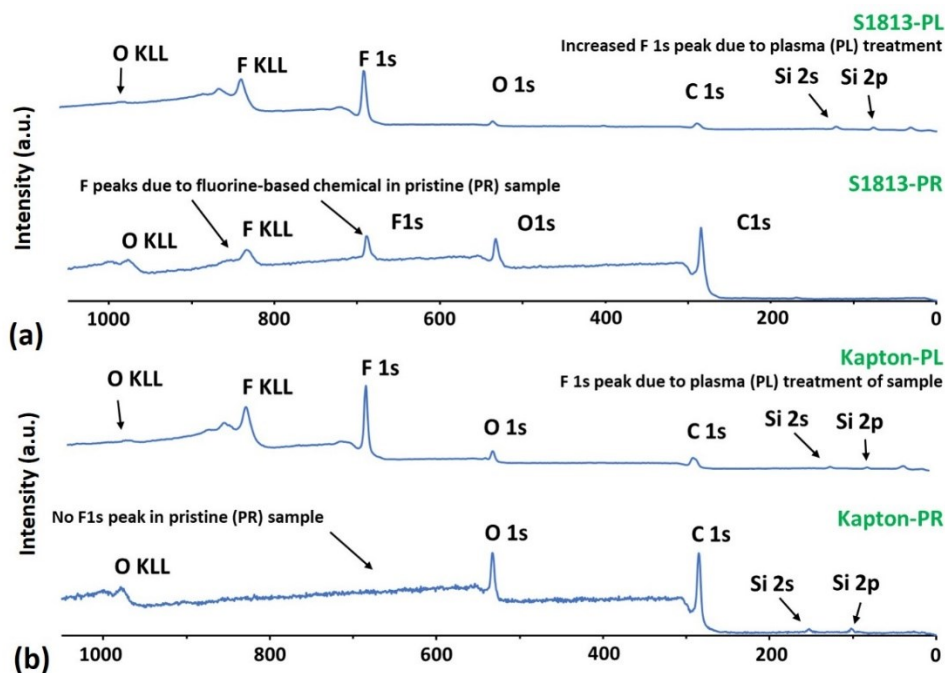


Figure 3.7. (a) XPS survey spectrum of S1813, plasma-treated (top) and pristine (bottom); (b) XPS survey spectrum of Kapton tape (polyimide), plasma-treated (top) and pristine (bottom).

In the pristine PDMS survey, labeled ‘PDMS-PR’ in Figure 3.6a, the C 1s peak corresponds to C-H and C-Si bonds (284.8 eV); there are no C-C bonds in PDMS. The key feature to observe in the survey is the lack of fluorine (F 1s and F KLL) peaks. The plasma-treated PDMS survey, labeled ‘PDMS-PL’ in Figure 3.6a, has the fluorine F 1s and F KLL peaks, indicative of fluorination of the methyl groups in PDMS.

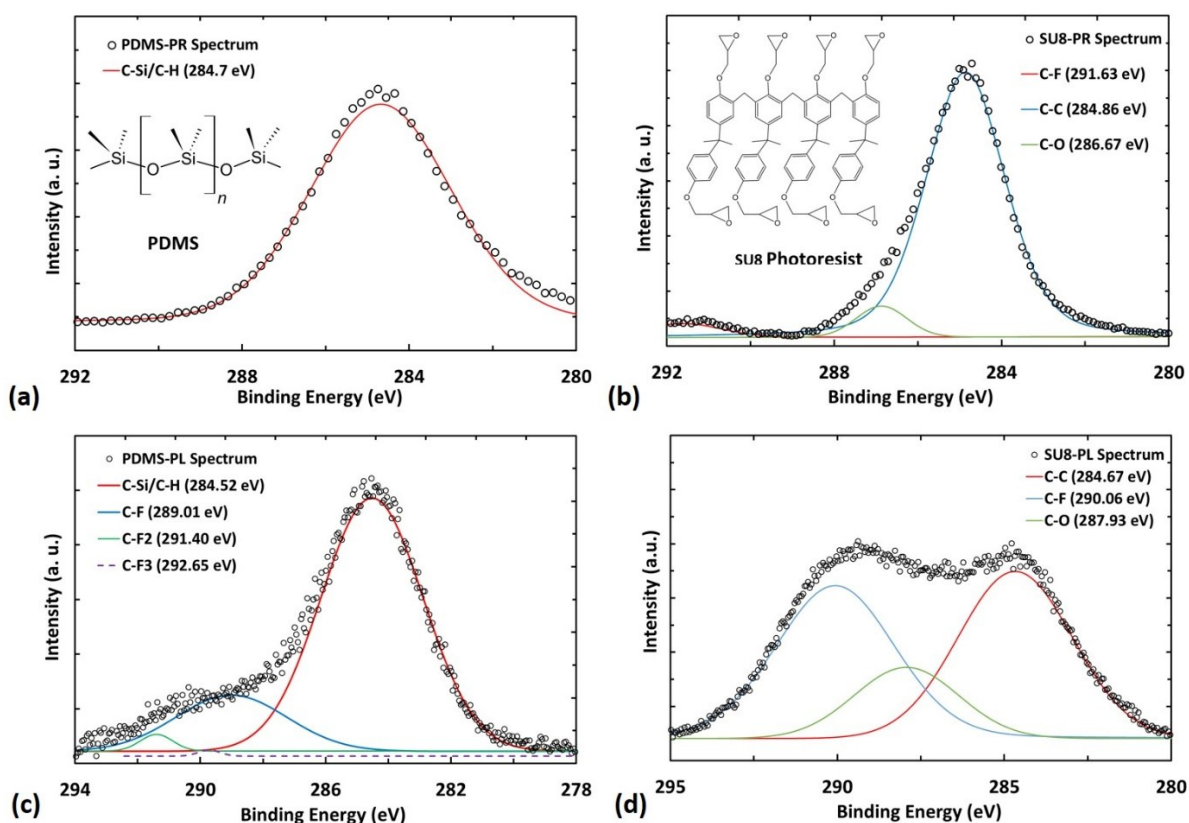


Figure 3.8. C 1s XPS spectra for (a) pristine PDMS (PDMS-PR), the inset is the molecular structure of PDMS (redrawn from Seethapathy et al. [121]); (b) pristine SU8 (SU8-PR), the inset is the molecular structure of SU8 (redrawn from Madou et al. [122]); (c) plasma-treated PDMS (PDMS-PL); (d) plasma-treated SU8 (SU8-PL). The binding energies were obtained from Bratt, et al. [123] and Cordeiro et al. [124].

The fluorination of methyl groups in PDMS has been reported by Manca et al. [125], which studied the effect of CF_4 plasma on the chemistry and topology of PDMS. Based on the findings of that paper, and upon comparing the C 1s XPS spectrum of PDMS-PR (Figure 3.8a) to the C 1s spectra of PDMS-PL (Figure 3.8c), it seems very likely that the $\text{CF}_4:\text{O}_2$ plasma causes different degrees of fluorination (CH_3 to CFH_2 , CH_3 to CF_2H , and CH_3 to CF_3) of the surface methyl groups of PDMS. Additionally, Figure 3.8c shows that the deconvolution of peaks indicates that about 20% of the PDMS surface methyl groups does show some degree of fluorination, most of it likely CFH_2 (blue curve) and CF_2H (green curve).

Figure 3.6b, 3.7a, and 3.8b show that the survey spectra for pristine SU8 (labeled ‘SU8-PR’) and S1813 (labeled “S1813”) already has the fluorine F 1s and F KLL peaks. This is due to the triarylsulfonium hexafluoroantimonate component in SU8, which is the UV sensitive crosslinking initiator mixed in with the SU8 epoxy resin, and a significant amount remains even after UV exposure [126]. However, plasma-treatment of SU8 (‘SU8-PL’) still fluorinates many methylated carbons in the SU8 (likewise for S1813). This can be seen in the larger intensity of the F 1s peak when compared with the C 1s peak (Figure 3.6b, SU8-PL survey and Figure 3.7a S1813-PL), and in observing that the C 1s XPS spectra of SU8-PL (Figure 3.8d) shows that the C-F peak has near equal intensity to the C-C peak.

These results indicate that the plasma-treatment does generally fluorinate the polymer surface which should lower the overall surface energy. Manca et al. [125] clearly demonstrated that a pure CF_4 plasma does indeed lower surface energy of PDMS through chemical modification of the methyl groups by fluorination, and each material has a unique number of methyl groups leading to different amounts of fluorination. However, a CF_4/O_2 plasma-treatment

creates significant surface roughness, which likely reduces the role of chemical modification by reducing contact area of the droplet and the material surface. This is especially the case if the surface roughness produces a Cassie-Baxter wetting interface against liquid metals.

3.4.5 A primer on Young, Wenzel, and Cassie-Baxter state

When characterizing the wetting property of a surface, the contact angle of the liquid droplet wetting the surface can be associated with the interfacial tensions of the liquid, solid, and air, when in equilibrium. This relation is given by Young's equation:

$$\gamma_{SV} = \gamma_{SL} + \gamma_{LV} \cos \theta_{YOUNG} \quad (1)$$

where θ_{YOUNG} is the measured contact angle (Figure 3.9a) and γ_{LV} , γ_{SV} , and γ_{SL} are the interfacial tension of the liquid-air interface, air-solid interface, and liquid-solid interface, respectively. This equation is based on the assumption that the surface is flat and does not have any roughness (Young state).

When surface roughness exists, two types of liquid-solid interfaces are possible. If the liquid wets the rough surface, it is said to be in the Wenzel state. In this state, the area the liquid droplet wets is larger than projected (apparent) area due to the surface roughness; this creates a new contact angle θ_W (Figure 3.9b). Wenzel et al. [127] reported a simple relation to convert the new contact angle to the contact angle that would have been measured without the surface roughness (θ_{YOUNG}) is given by:

$$\cos \theta_W = r \cos \theta_{YOUNG} \quad (2)$$

where $r = \text{Contact Area/Projected area} \geq 1$.

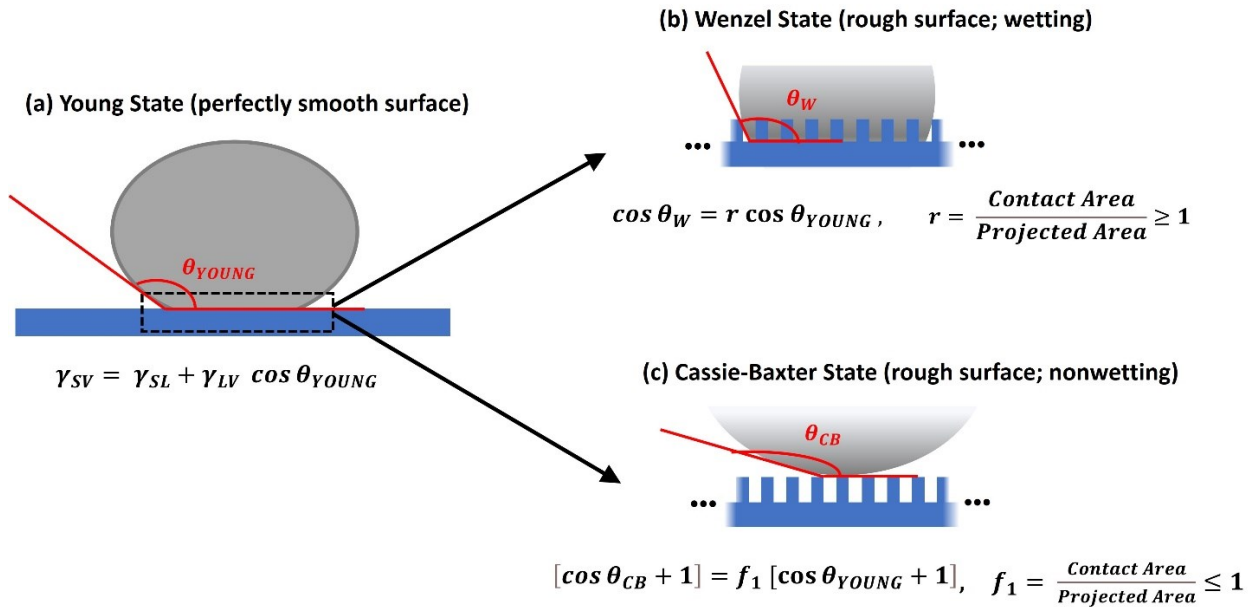


Figure 3.9. (a) Young state and the equation associated with it assumes the surface is perfectly smooth; (b) the Wenzel state and the equation associated with it assumes the surface is rough and that the liquid is contact with more surface area that the area enclosed by the triple contact line between liquid, air, and solid, which leads to more wetting; (c) the Cassie-Baxter state and the equation associated with it assumes the surface is rough and the liquid has partial contact with the surface leading to a less wetting.

The second type of liquid-solid interface for a rough surface is when the liquid does not wet the rough surface entirely, creating a composite surface composed of a combination of the solid and air that results in lesser contact with the solid surface, which create a new contact angle θ_{CB} . This is called the Cassie-Baxter state, and Cassie et al. [128] formulated an equation that connects the new contact angle, θ_{CB} , to the contact angle for smooth surfaces, θ_{YOUNG} , given by:

$$\cos \theta_{CB} + 1 = f_1 (\cos \theta_{YOUNG} + 1) \quad (3)$$

where $f_1 = \text{Contact Area}/\text{Projected area} \leq 1$.

These concepts show how contact angle measurements are related to interfacial energy, and the formulas show that these measurements can be used to measure the surface energy of a

solid surface. These concepts also help to explain how the wetting/nonwetting property is affected by surface roughness.

3.4.6 Surface roughness analysis of pristine and CF₄/O₂ plasma-treated surfaces using AFM

Atomic force microscopy measurements can be used to determine the differences in surface roughness between pristine and plasma-treated materials. Figure 3.10 visually shows the significant increase in surface roughness caused by plasma-treatment of PDMS (Figure 3.11 show the 3D surface plots of S1813 (a,b), Kapton (c,d), and SU8 (e,f), respectively.) The areal surface roughness parameters Sa Sq and Sm were calculated for each material and presented in Table 3.1. Sa is the arithmetic mean of peak heights of a surface and is typically used as a measure of surface roughness; Sq is the standard deviation of the peak heights; Sm is the mean separation between peaks; and r_{AFM} is the Wenzel fraction, which is the ratio of the total surface area of a rough surface to its projected surface area.

Table 3.1. Areal surface roughness parameters obtained from AFM software.

PROCESS	POLYMER	Sa (nm)	Sq (nm)	Sm (nm)	r_{AFM}	Sa:Sm
PRISTINE	PDMS	0.353	0.443	175.0	1.001	0.002
	SU8	0.190	0.238	115.4	1.000	0.002
	S1813	0.222	0.277	135.3	1.000	0.002
	KAPTON	0.639	0.809	099.7	1.002	0.006
PLASMA TREATED	PDMS	136.9	156.9	542.5	2.948	0.252
	SU8	032.2	039.8	385.1	1.390	0.084
	S1813	043.4	054.6	425.9	1.336	0.102
	KAPTON	040.0	050.6	390.6	1.373	0.102

Comparisons of these values can give insight into how much the contact area is reduced. Comparing S_a and S_q show that there is at least an order of magnitude increase in surface roughness in a plasma-treated material compared to a pristine material. S_m values of plasma-treated materials are roughly 3 times greater than that of pristine materials, indicating greater space between peaks.

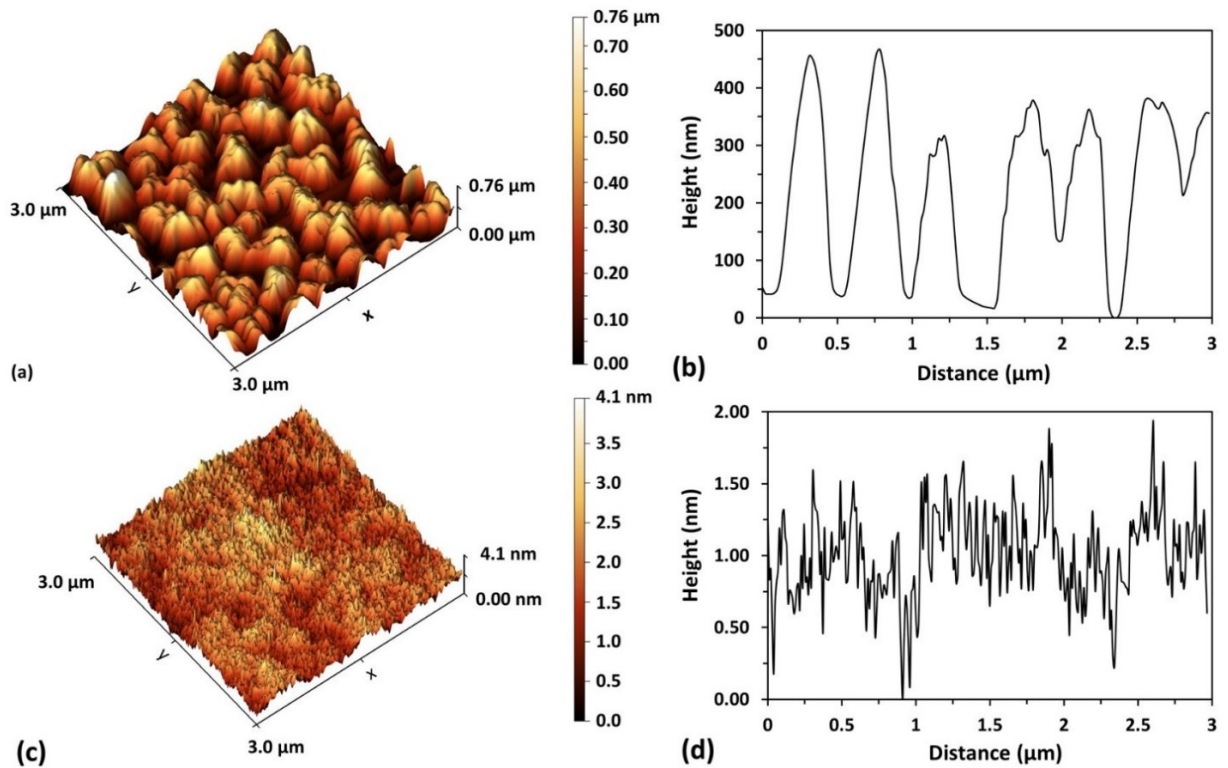


Figure 3.10. (a) 3D surface plot of plasma-treated PDMS and its (b) height profile; (c) 3D surface plot of pristine PDMS and its (d) height profile.

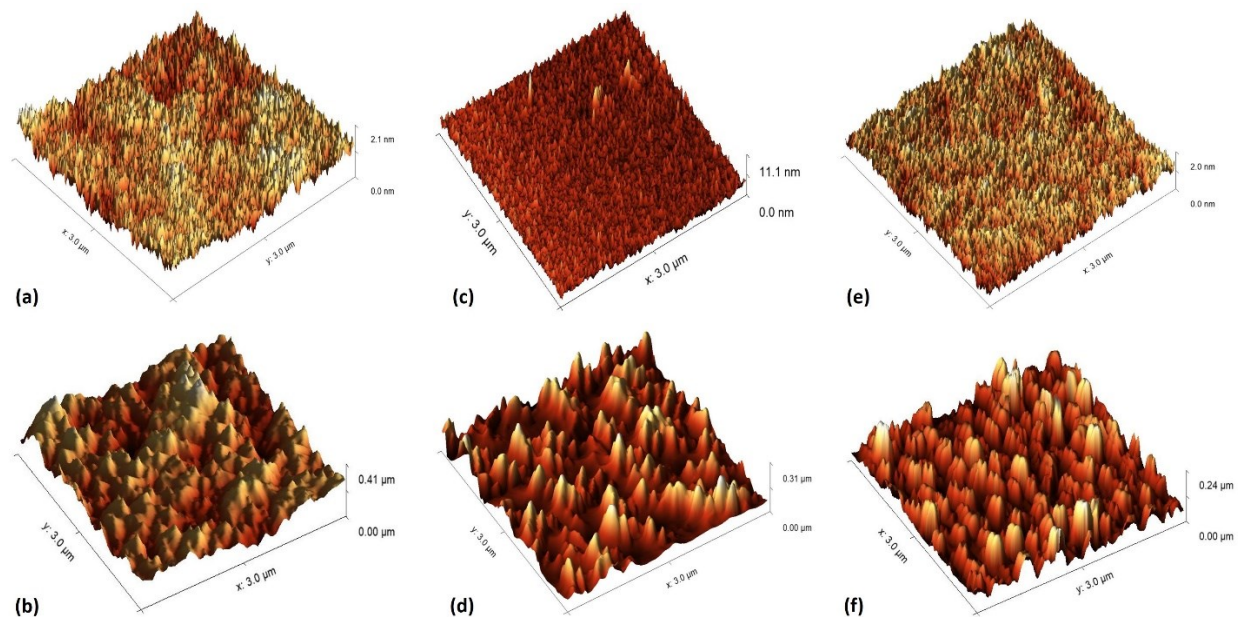


Figure 3.11. (a) 3D surface plot of pristine S1813 and (b) 3D surface plot of plasma-treated S1813; (c) 3D surface plot of pristine Kapton tape and (d) 3D surface plot of plasma-treated Kapton tape; (e) 3D surface plot of pristine SU8-2010 and (f) 3D surface plot of plasma-treated SU8-2010.

Lastly, comparisons of height:width aspect ratios of empty regions, estimated by $S_a:S_m$, of plasma-treated surfaces are roughly two orders of magnitude greater than pristine surfaces. These comparisons collectively indicate a significant amount of material contact area has been replaced with air, and strongly indicates that liquid metal droplets on plasma-treated materials are in the Cassie-Baxter state, and that this drop in material contact area is likely a significant contributing factor to the nonwetting property created by the plasma-treatment process.

3.4.7 Estimating apparent surface free energy

For rough surfaces one typically calculates the apparent surface free energy to understand its wetting behavior[129]–[132]. Calculation of apparent surface free energy is typically done using the two probe liquid method developed by Girifalco and Good [133], [134] for two liquid

systems, and was later used by Fowkes [135], [136] to determine the surface free energy of a variety of surfaces. The method uses a polar and nonpolar liquid to determine the surface free energy using the following equation [137]:

$$\frac{1}{2}\gamma_{LV}(1 + \cos \theta) = \sqrt{\gamma_{SV}^d \gamma_{LV}^d} + \sqrt{\gamma_{SV}^p \gamma_{LV}^p} \quad (4)$$

where γ_{LV} is the surface tension of the liquid, and θ is the measured contact angle. γ_{LV}^d and γ_{LV}^p are the dispersive and polar components, respectively, of the liquid's surface tension. γ_{SV}^d and γ_{SV}^p are the dispersive and polar components, respectively, of the solid's surface free energy. Note that the sum of the dispersive and polar components will give the total surface free energy.

Two standard liquids with well-known dispersive and polar components are used. The two standard liquids used are deionized water and diiodomethane. The dispersive and polar component of deionized water (DIW) are 21.8 mN/m and 51.0 mN/m, respectively, for a total surface tension of 72.8 mN/m [138]. The dispersive and polar component of diiodomethane (DIO) are 50.8 mN/m and 0 mN/m, respectively, for a total surface tension of 50.8 mN/m.

Table 3.2. Apparent surface free energy of pristine and plasma-treated polymeric surfaces.

PROCESS	MATERIAL	Dispersive Component (mN/m)	Polar Component (mN/m)	Apparent Surface Free Energy (mN/m)
PRISTINE	PDMS	25.65 ± 0.38	1.61 ± 0.32	27.26 ± 0.71
	SU8	49.11 ± 0.25	0.07 ± 1.71	49.17 ± 1.96
	S1813	37.54 ± 0.50	1.17 ± 1.60	38.71 ± 2.10
	KAPTON	34.16 ± 0.49	0.07 ± 1.11	34.23 ± 1.60
PLASMA-TREATED	PDMS	20.93 ± 0.27	4.78 ± 1.36	25.71 ± 1.63
	SU8	6.73 ± 0.26	2.43 ± 0.39	9.15 ± 0.65
	S1813	7.04 ± 0.25	1.57 ± 0.36	8.61 ± 0.60
	KAPTON	20.72 ± 0.27	0.00 ± 0.60	20.72 ± 0.87

Table 3.2 provides the calculated values for the apparent surface free energy for each surface. The value for pristine PDMS shows a dispersive and polar component that closely matches the value reported in literature by Owen and Wendt [139] ($\gamma_{SV,PDMS}^d = 21.7$ mN/m and $\gamma_{SV,PDMS}^p = 1.1$ mN/m). After plasma treatment, the dispersive component of the apparent surface free energy reduces and the polar component increases, resulting in a negligible change in the total surface energy. The nonwetting property of plasma-treated PDMS is likely due to the lowering of dispersive forces. Fowkes [135] distinguishes between dispersive forces (purely attractive) from the polar forces and metallic bond forces which can be both attractive and repulsive. A reduction in the purely attractive dispersive forces may be sufficient to prevent wetting of the liquid metal. This is supported by the drastic reduction in the dispersive forces in the other three plasma-treated materials while the polar forces remain relatively low.

3.4.8 Generalizing the process to other polymers

When considering the results that the same plasma treatment is able to convert four different classes of polymers from wetting to nonwetting surfaces, one seeks a common feature responsible for the similar results. One common feature among the four polymers due to the plasma treatment is the surface roughness, which reduces the contact area with the liquid. As previously suggested, the high surface tension of the liquid metal on such a rough surface would naturally create a Cassie-Baxter interface. To further support this claim, SU8 and S1813 surfaces subjected to 60 s O₂ plasma was also shown to be nonwetting indicating that for some materials (PDMS and polyimide were unaffected by oxygen plasma) fluorine plasma is not needed to create a nonwetting surface, and that surface roughness alone is a sufficient condition to create a

nonwetting surface. The evidence suggests that the CF_4/O_2 plasma treatment can be treated as a general method to convert any polymer surface into a non-wetting surface for gallium-based liquid metals by creating a sub-micron surface roughness, allowing a larger number of materials as potential substrates for nonwetting liquid metal applications.

3.5 Conclusion

A brief literature survey indicated that the wetting nature of the oxide skin of gallium-based liquid metals limits the development in liquid metal droplet microfluidics. A simple CF_4/O_2 plasma-treatment for 120s was shown to convert previously wetting polymers to nonwetting surface for surface-oxidized gallium-based liquid metal droplets. Static contact angle measurements for all plasma-treated polymer surfaces were above 150° . Dynamic contact angle measurements showed that the plasma-treated surface yielded low contact angle hysteresis. XPS analyses indicated that the surface undergoes partial fluorination of methyl groups, helping to lowers the surface energy. AFM analyses showed an order of magnitude increase in surface roughness creating a Cassie-Baxter state for the high surface tension liquid metal. Apparent surface free energy calculations show an overall reduction in dispersive forces indicating that the reduction in effective surface area due to Cassie-Baxter state is the cause of nonwetting. Oxygen plasma treatment also produced nonwetting surfaces in S1813 and SU8, indicating surface roughness in a sufficient condition to create nonwetting surfaces for liquid metals. Since this plasma-treatment created nonwetting surfaces from wetting through a physical change of the surface, it is reasonable that this plasma-treatment may be generally used to convert other wetting organic polymers to nonwetting surfaces, which would be useful to explore new liquid metal applications that require nonwetting surfaces.

CHAPTER 4

FEASIBILITY STUDY ON PNEUMATIC ACTUATION AND GENERATION OF SURFACE-OXIDIZED GALLIUM-BASED LIQUID METAL DROPLETS IN NON-WETTING PLASMA-TREATED POLYMER CHANNELS

As mentioned in §1.4, there has been very little research reported on pneumatic actuation and generation of surface-oxidized liquid metal (oxLM) droplets. The reason for this, as explained in §1.2, is due to the wetting nature of oxLMs. It seems reasonable then that any surface not wet by oxLMs would be a good candidate material for making channels in which one could generate and actuate oxLM droplets. The study of CF_4/O_2 plasma-treated polymers in Chapter 3 would suggest that any polymer with such a plasma treatment would make a good candidate. Of the polymers studied in Chapter 3, PDMS seems to be the best option. The photopolymers SU8 and S1813 are too brittle, while Kapton tape does not have enough plastic or elastic property to be formed into a channel, which makes the flexible and elastic PDMS the ideal candidate. The work in this chapter presents a feasibility study on the pneumatic actuation and generation of liquid metal droplets in CF_4/O_2 plasma-treated PDMS channels. First, the experimental design and polymer choice is presented. Next, fabrication methods are presented along with the fabrication limitations encountered when creating the channels. The result of experiments clearly show that the droplet generation and actuation is infeasible, and an analysis is provided to show that although CF_4/O_2 plasma-treatment of polymer surfaces may not be ideal for fabricating closed channels, it is the surface oxide of the liquid metal that prevents pneumatic generation and actuation of oxLMs.

4.1 Channel design choice for droplet generation and actuation

The experimental setup for droplet generation is chosen based on similar works found in literature. As mentioned in §1.4, Li et al. reported a study on both deoxidized liquid metal droplet actuation [36] and oxidized liquid metal droplet actuation [53]. For the deoxidized liquid metal experimental setup, they attached a syringe pump to the inlet of a standard T-junction channel (Figure 4.1a inset) with two adjacent side channels filled with HCl (Figure 1.4b) to allow for HCl vapors to permeate into the center channel and remove any surface oxide from the liquid metal droplet. Li et al. were able to successfully actuate the droplet with enough control to find a relation between the air pressure required for actuation and the volume of droplet (plot Figure 4.1a). For the oxidized liquid metal droplet actuation experimental setup, they used a serpentine T-channel, though the reason for using a serpentine channel was not given. For droplet generation, Song et al. [140] reported that a basic T-junction channel can be used to pneumatically generate and actuate water droplets within a superhydrophobic channel (Figure 4.1b), so the T-junction channel can also be used to test for droplet generation of oxLMs. Thus, the T-junction channel was chosen as the channel type for this feasibility study to test actuation and generation of liquid metal droplets. To make testing simpler, 1D channel was also fabricated, with the idea that a liquid metal droplet can be injected into the channel to perform actuation tests only.

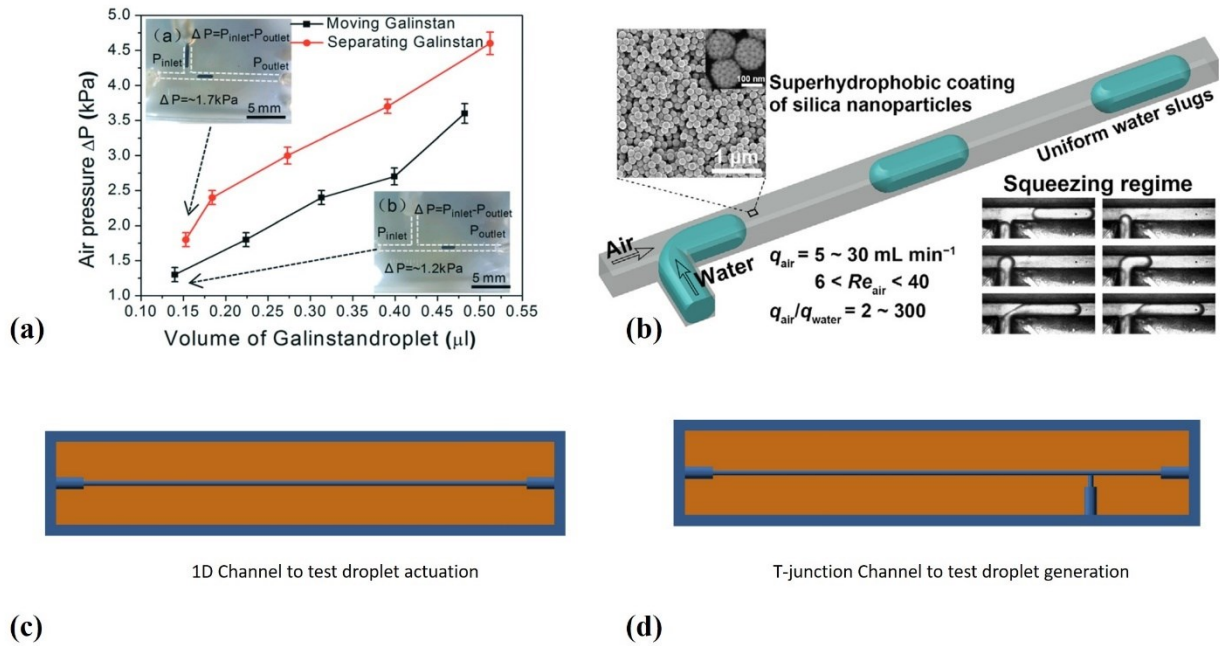


Figure 4.1. (a) HCl-vapor exposed liquid metal droplet in PDMS T-junction channel, reprinted from Ref. [36] © 2014 American Chemical Society; (b) T-junction channel with superhydrophobic surface for generation of uniform water slugs, reprinted from Ref. [140] under Creative-Commons CC-BY license; (c) CAD drawing of 1D Channel; (d) CAD drawing of T-junction channel.

4.2 Experimental setup and fabrication

4.2.1 Experimental setup

To actuate the droplet, a New Era Syringe pump (model# 00266-GB, New Era Pump Systems, Inc. Farmingdale, NY U.S.A.) was used with a Becton-Dickinson (B-D) 3mL air filled syringe (BD Inc, Franklin Lakes, NJ, U.S.A.). Depending in the channel inlet diameter, either Cole-Parmer PTFE #20 AWG or Natural-100 PTFE tubing were used to connect the 3mL syringe to the PDMS channels. To generate droplets, liquid metal was injected by hand at the T-junction using a 3mL syringe with either a blunt large bore needle or a PTFE tubing that matched

the inlet of I-branch. The PTFE tubing was sealed airtight to the syringe or the PDMS channel inlets using a combination of pressure seal, epoxy glue, and a glue gun.

4.2.2 Fabrication of plasma-treated PDMS microfluidic channels

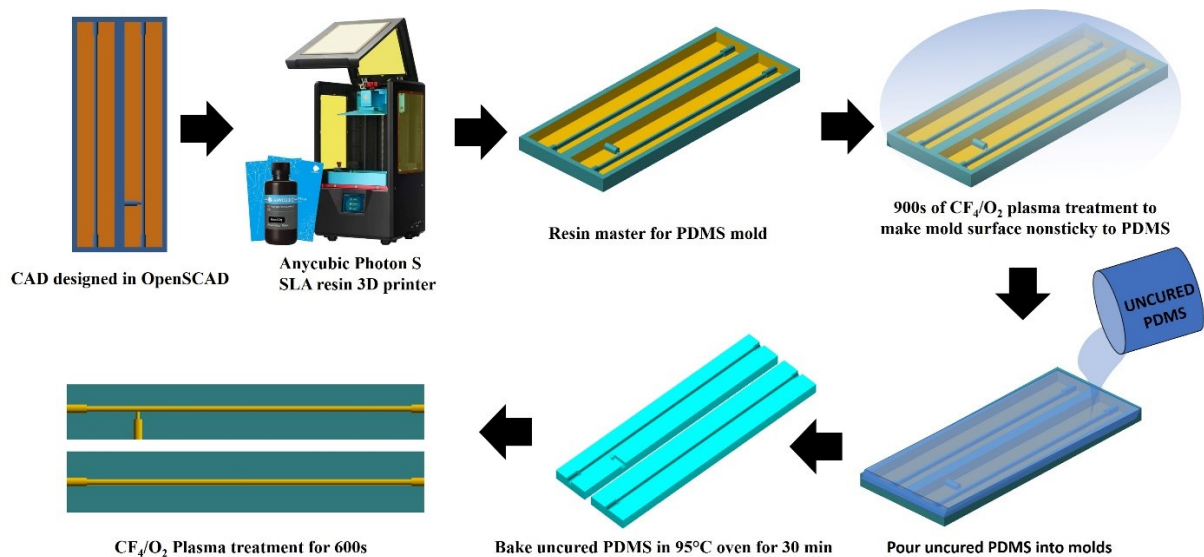


Figure 4.2. Fabrication steps for making a 1D PDMS channel and a T-junction channel.

Fabrication of the PDMS channels begins with creating a 3D CAD model of the master molds (Figure 4.1c and d) using a CAD software, and 3D-printed in UV curable resin (Figure 4.2). The master molds were printed on a Photon S SLA resin 3D Printer at 50 μ m Z-resolution (Arylic, Shenzhen, China) using the clear Arylic UV curable resin. Once the resin master is printed, it is sonicated in acetone for 3 mins, N_2 spray dried, and treated with CF_4/O_2 plasma for 900 s to make the surface non-sticky to PDMS. After the plasma treatment, uncured desiccated 10:1 PDMS mixture is poured into the master molds and baked in 95°C oven for 30 min to fully cure the PDMS. The pristine PDMS channel molds are removed from the master molds using a blade. To create nonwetting channel walls, a CF_4/O_2 plasma treatment is applied

to the channel-side surface of the PDMS molds for 600 s (120 s is good for flat surfaces, but not for channels; more time is needed to render the channels nonwetting.) These PDMS channel molds are the top half of the microfluidic device. To create the bottom half, a large 2mm thick rectangular slab of PDMS was fabricated and treated to 600 s CF₄/O₂ plasma. These two halves will be affixed to each other to create a closed 1D or T-junction channel.

4.2.3 Limitations of plasma-treated PDMS surfaces

Pristine PDMS surfaces have the useful property of being able to bond with itself when its surfaces are briefly exposed to a low power oxygen plasma and brought into mutual contact [141], [142]. However, this property is lost when a CF₄/O₂ plasma treatment is applied to a PDMS surface. A few other methods were tried to bond the plasma-treated surfaces. Hard masks and patterned resists were used to prevent plasma treatment of the non-channel surfaces. The hard mask was unable to prevent the plasma from going underneath and converting the surface to become nonwetting. With patterned resist, aligning masks to PDMS microfluidics structures proved difficult to achieve due to the soft compliant nature of PDMS. Furthermore, the warping of the PDMS surface created cracks in the resist exposing portions of the PDMS surface to plasma, preventing oxygen plasma bonding.

The only solution that allowed affixing plasma-treated PDMS surfaces to each other was to apply a thin coat of uncured PDMS by hand on to the surfaces that required bonding. This method provides two options for bonding. The first is to apply a thin coat of uncured PDMS, immediately bond the sections before it cures, and bake in a 95°C oven immediately for 30mins until cured. The second option is to bake the applied coating before affixing surfaces in a 95°C

oven and then use oxygen bonding to bond the coated surfaces. Due to uneven thickness of the hand-applied coating, the latter method had regions that would leak air. Since this work deals with pneumatics the first option (uncured PDMS as glue) was used to bond the top and bottom halves of the plasma-treated PDMS channel devices (Figure 4.3.)

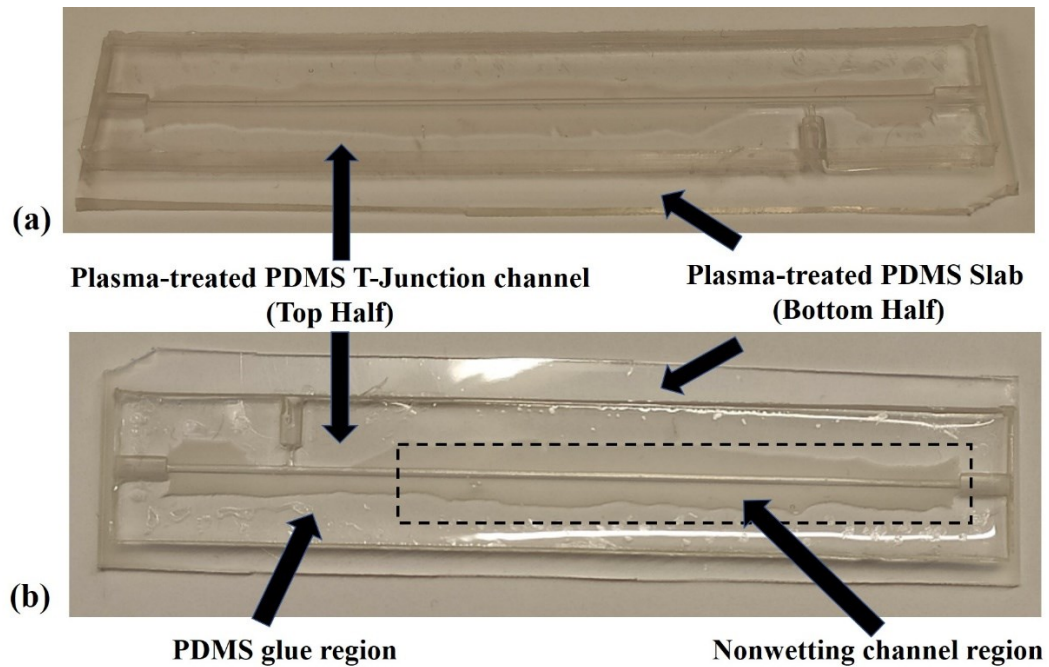


Figure 4.3. PDMS plasma-treated nonwetting T-junction channel (a) isometric view and (b) top view.

4.2.4 Limitations of channel depth and shape

Initially, a square channel profile was used, however it became clear that the plasma had difficulty reaching the corners of the square channel, and liquid metal would wet the corners. Furthermore, for channels that were too deep (> 1 height:width aspect ratios) the plasma would not reach the bottom surface of the channel and these surfaces would be wet by liquid metal (Figure 4.4a and b) if 1 mm or larger. Thus, cylindrical channels, with height:width aspect ratios

slightly less than 1 were chosen. For cylindrical channels there are no sharp corners, allowing the plasma to reach all parts of the channel surface, and making the whole channel surface nonwetting (Figure 4.4c, d, and e). For these reasons, the channel shape was chosen to be cylindrical with a roughly elliptical cross-section (1mm high, 1mm wide).

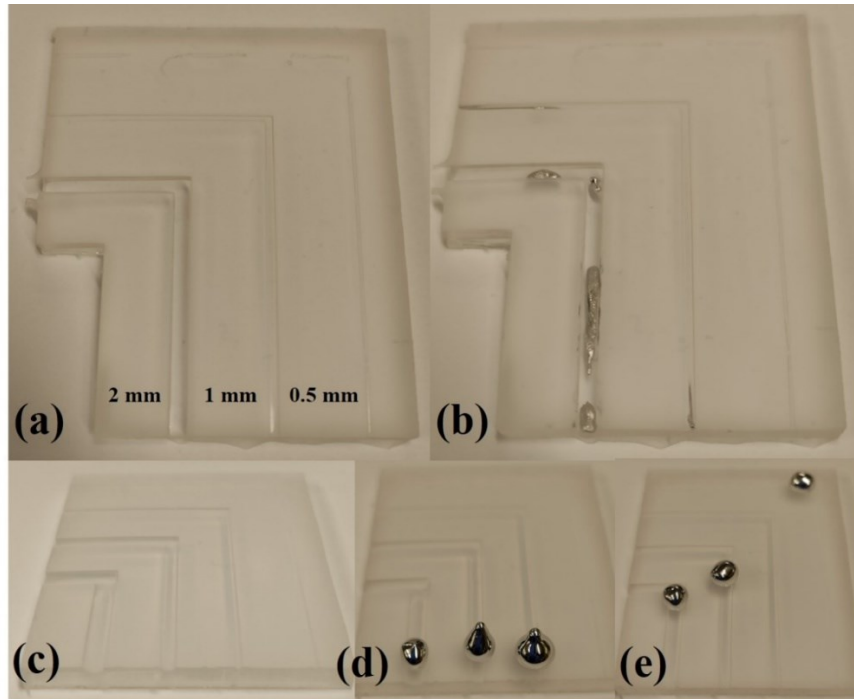


Figure 4.4. 600 s CF_4/O_2 plasma-treated square channels (a) before liquid metal touch test and (b) residue after touch test. 600 s CF_4/O_2 plasma-treated cylindrical channels: (c) before liquid metal touch test, (d) with liquid metal drop on channels, and (e) free movement of liquid metal droplets, demonstrating that plasma treatment is better suited for cylindrical channels than square channels.

4.3 Actuation results

4.3.1 Plasma-treated 1D channels

1D plasma-treated channels were injected with ~13 mm long liquid metal slug. After the PTFE tube was glued to the inlet (see Figure 4.5a) the syringe pump was used to apply an air flow rate of 10mL/min. The results show that actuation was not successful due to deformations in the liquid metal slug that allowed air to pass through (Figure 4.5a and b). To remove the deformations, a small volume of 37% HCl aqueous solution was slowly pumped into the PTFE tube and brought close to the liquid metal slug (Figure 4.9b and c.) As the HCl vapors reach the slug, the deformations on the slug's surface vanish leaving a uniform surface and a slight smaller slug length (~12 mm). One can infer that without the oxide skin, the surface tension is free to minimize the volume of the slug. However, there was still no movement; the slug was not fully deoxidized and still remained deformed enough to let air through.

Next, a plasma-treated PDMS channel was washed with 37% HCl (aq.), and a new liquid metal slug was injected into the channel. In this case, the slug was easily actuated (Figure 4.9d, e, and f) to the slip layer that allows low pressure actuation of the liquid metal droplets. When HCl reacts with gallium oxide one of the by-products is water. This water by-product usually accumulates on the surface of the droplet creating a slip layer that allows the droplet to move with very little pneumatic pressure.

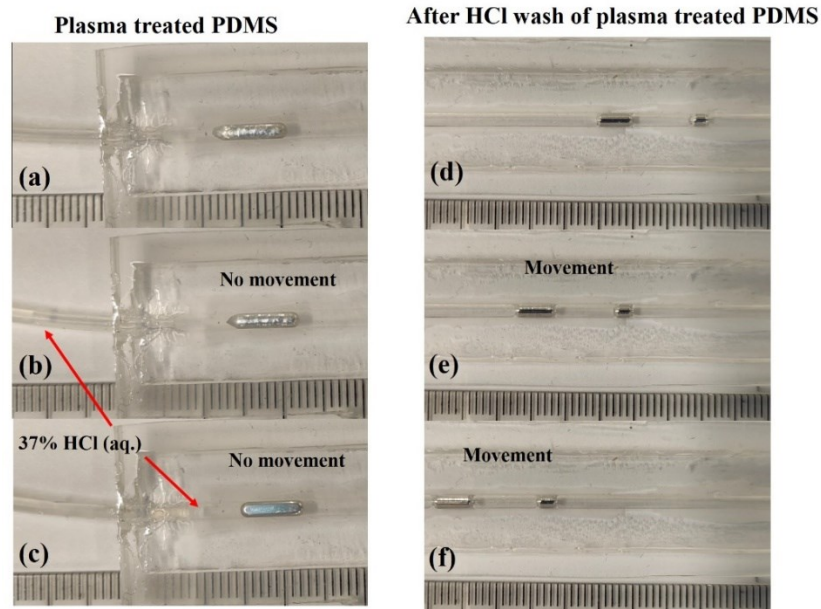


Figure 4.5. (a) surface oxidized liquid metal slug; (b) 37% HCl (aq.) introduced, however slug not moving, air is moving freely around the slug; (c) 37% HCl (aq.) a few mm from slug, still no movement, slug surface oxide has been removed. HCl (aq.) now forms a slip layer and actuation (d-f) is now possible.

4.3.2 Liquid metal droplet generation results

To test droplet generation, a long liquid metal slug was inserted into the main channel via the T-junction to ensure a tight seal between the slug surface and the channel wall to make it difficult for air to flowing past the slug due to any deformations (Figure 4.6a). As more pneumatic pressure was applied, the air pressure built up against the slug. Eventually, the pressure increased until it apparently overcame the oxide layer's mechanical strength causing it to buckle (Figure 4.6b). The buckling caused uneven air pressures within the channel that caused the liquid metal to splatter opening a path to allow free flow of air (Figure 4.6c). Note that the liquid metal in the channel remains in its deformed state due to the mechanical strength of the surface oxide layer, as mentioned in §1.2. The strength of the oxide layer is sufficient to overcome the surface tension forces of the pure liquid metal underneath (Figure 4.7). In this case,

the oxide permanently flattens the liquid metal to the channel floor (Figure 4.7a, and b), and the only way to minimize the surface area of the liquid metal would be to expose it to HCl vapors (Figure 4.7c, and d.)

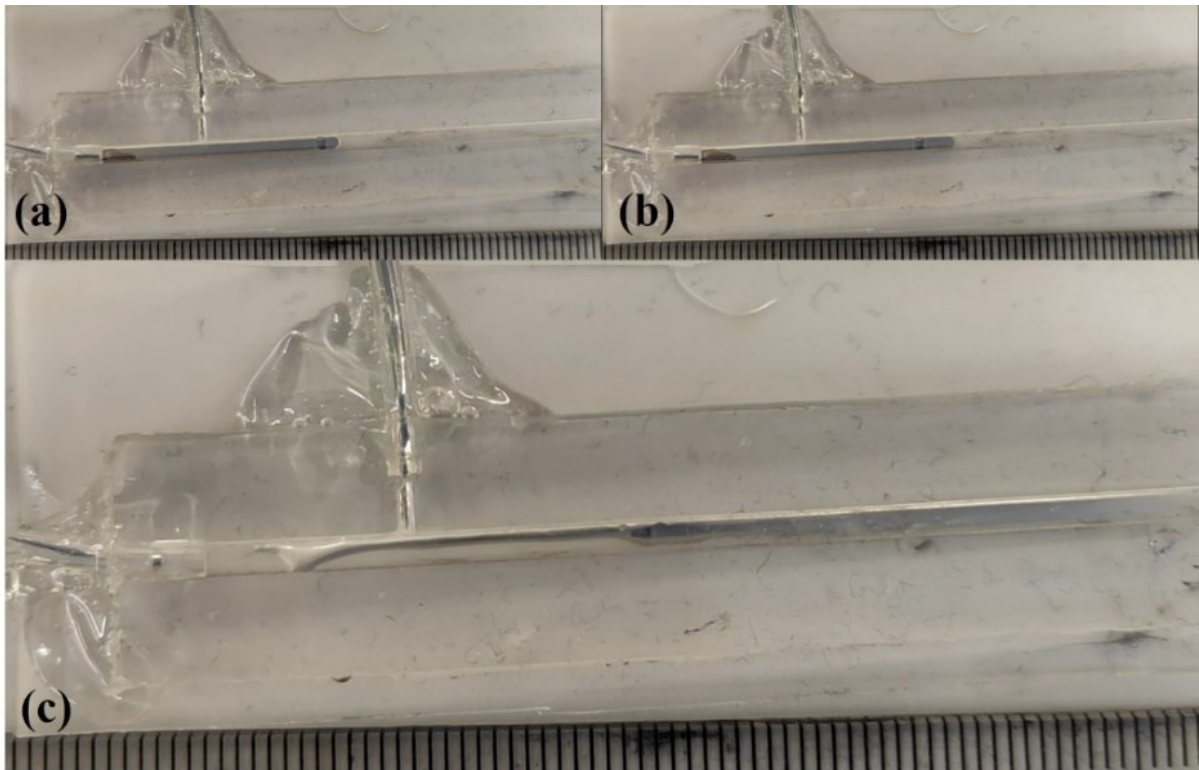


Figure 4.6. (a) a very long liquid metal slug is draw out from the T-junction. As pressure is applied (to the right) the oxide layer buckles (b) with some parts stable and other parts deforming. As pressure builds due to the strength of the oxide layer it reaches a threshold that eventually over comes the strength of the oxide skin and the liquid metal droplet rapidly stretches and deforms until the air can flow without hindrance with in the channel.

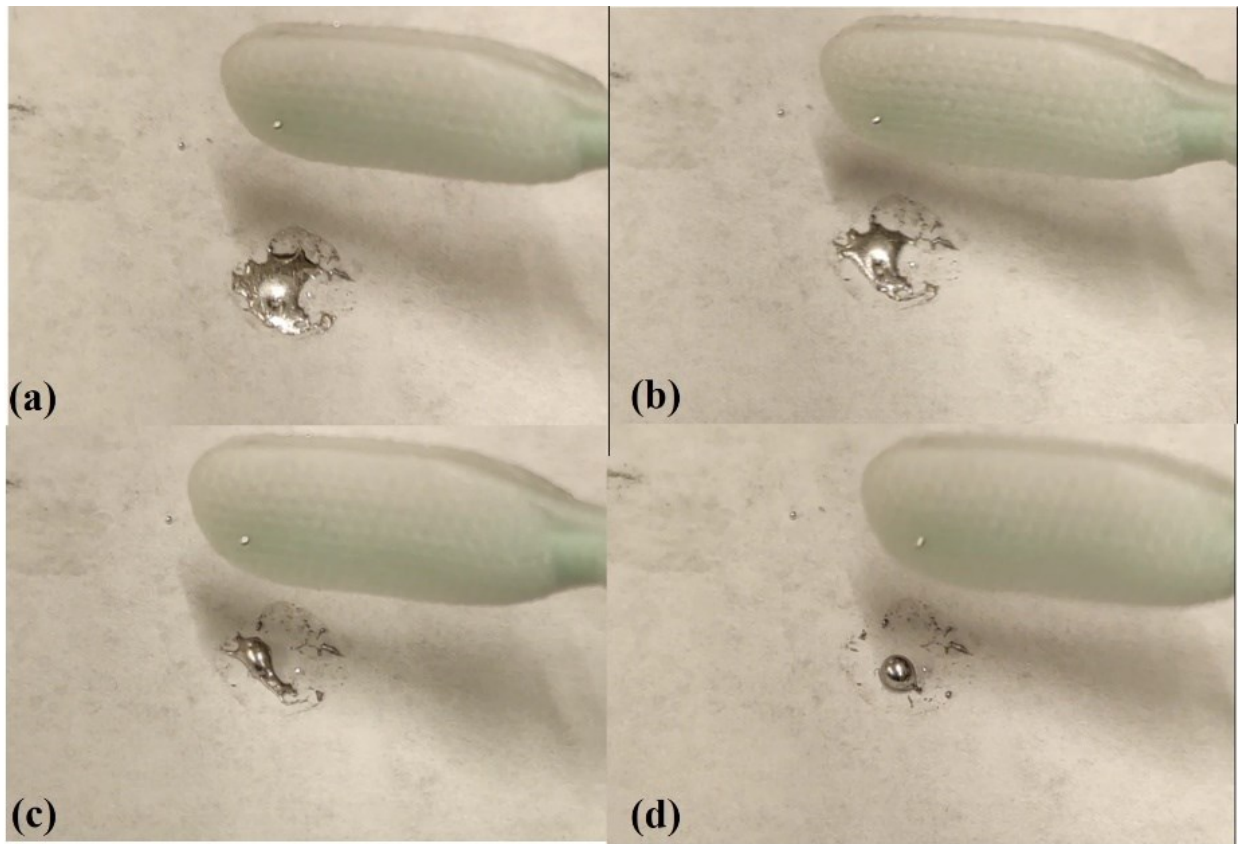


Figure 4.7. (a-d) Demonstration that the mechanical strength of the oxide layer can keep a liquid metal droplet flat, preventing the surface tension forces from forming a uniformly spherical droplet, until the oxide layer is removed by HCl vapors.

4.3.3 H₂SO₄-treated channels results

Li et al. [53] reported actuation of surface-oxidized liquid metal droplets in PDMS channels exposed to 89% H₂SO₄ solution for 90s. The exposure to sulfuric acid creates a hierarchical surface roughness over different orders of magnitude from microscale to millimeter scale (See Figure 4.8). In the supplementary section of the report there are images showing actuation of a surface oxidized liquid metal droplet (Figure 4.9a). However, liquid metal actuation using this method of generating nonwetting PDMS surface could not be replicated

(Figure 4.9b, c, and d). The same issue of the oxide skin flattening out the liquid metal slug and letting air through was encountered.

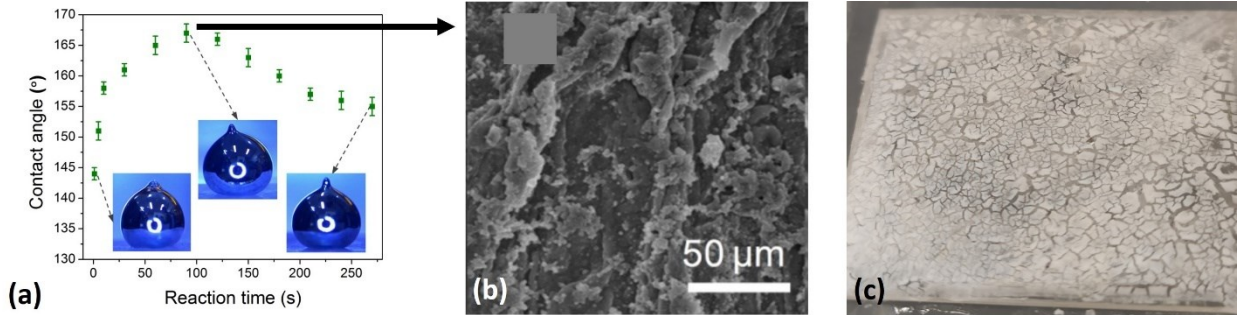


Figure 4.8. (a) contact angle vs reaction time to 89% H₂SO₄ solution, and (b) SEM image of PDMS exposed to 89% H₂SO₄ for 90s; reprinted from Ref. [53] © 2015 American Chemical Society. (c) hierarchical roughness of PDMS surface caused by 89% H₂SO₄ for 90s, fabricated by the author.

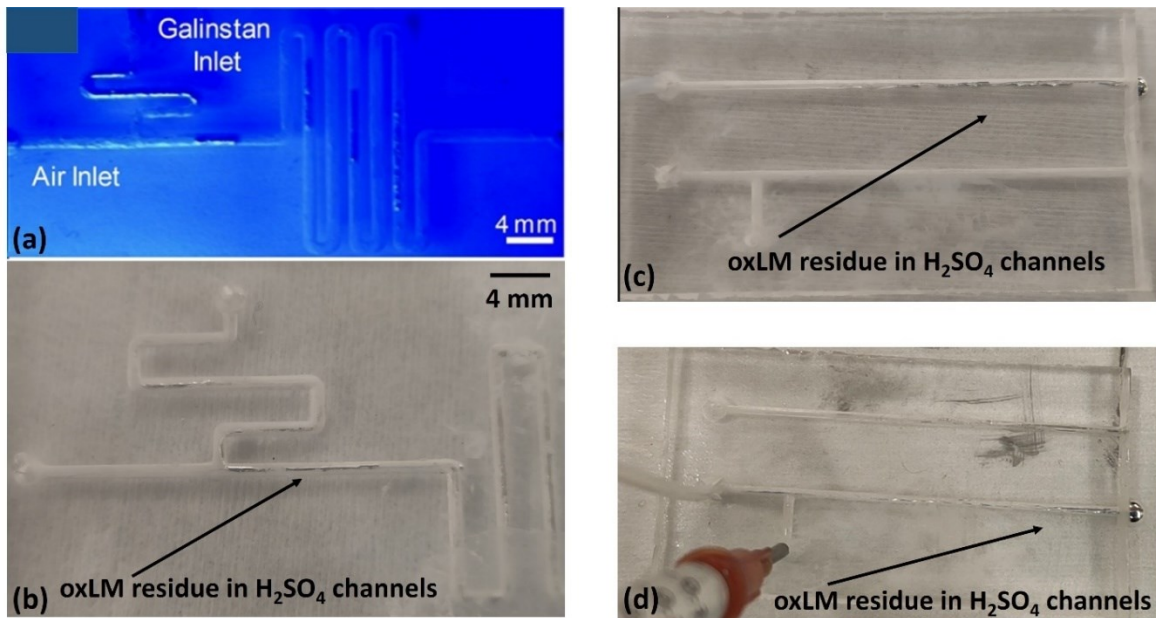


Figure 4.9. (a) serpentine T-junction channel, reprinted from Ref. [53] © 2015 American Chemical Society; (b) replica of 89% H₂SO₄-treated serpentine PDMS channel, with oxLM residue; (c) 89% H₂SO₄-treated 1D channel with oxLM residue, (d) 89% H₂SO₄-treated T-junction channel with oxLM residue.

4.4 Conclusion

The goal of this chapter was to present a feasibility study on whether CF_4/O_2 plasma-treated PDMS channels would allow pneumatically generated and actuated liquid metal droplets. It was demonstrated that both CF_4/O_2 plasma-treated PDMS and H_2SO_4 -treated PDMS channels were not able to generate or actuate surface-oxidized liquid metal droplets, with the single exception for H_2SO_4 -treated PDMS channels reported by Li et al. [53]. Although there were some issues in fabricating closed channels made from plasma-treated PDMS this was not the fundamental issue preventing generation and actuation of oxLM droplets. The experimental results show that the fundamental issue is that the mechanical strength of the oxide skin layer was large enough to overcome the high surface tension of the liquid metal. Under pneumatic forces, the oxLM droplet would simply flatten and remains flat letting the air flow over it. Therefore, it appears that the main obstacle to pneumatic generation and actuation of surface oxidized liquid metal microfluidics, in general, is the surface oxide of the liquid metal itself.

CHAPTER 5

SUMMARY AND FUTURE WORKS

5.1 Summary and conclusions

In this dissertation, various studies were conducted on PDMS-based devices and materials in areas involving strain sensors, plasma-treated surfaces, and liquid metal microfluidics.

In the area of strain sensing, a study was presented on a design rule to improve the quality factor of guided-mode resonance gratings. A research objective was formulated to conduct a simulation study on the effect of a design rule on the quality factor of a 2D GMR grating. This was achieved and presented in Chapter 2. The results of the study show that the slotting design rule, when applied to the strain sensor design, produced at least a 6-fold increase in quality factor and more symmetric sensitivities while roughly retaining the original resonance positions and material choices.

In the area of plasma-treated surfaces, a study was presented on the cause of CF_4/O_2 plasma-treated polymers to become a nonwetting surface toward surface-oxidized gallium-based liquid metals. A research objective was formulated to conduct standard surface analyses to determine the cause of the nonwetting property for various CF_4/O_2 plasma-treated polymers. This research objective was achieved and presented in Chapter 3. The surface analyses collectively show that the nature of the nonwetting property of CF_4/O_2 plasma-treated polymers is primarily due to the surface roughness forming a Cassie-Baxter state with the liquid metal, as well as a small contribution made by the fluorination of methyl groups in the polymer chains, which lowers the surface energy. Collectively, both surface roughness and fluorination were

shown to reduce the dispersive component of apparent surface free energy of the polymer surface.

In the area of gallium-based liquid metal microfluidics, a study was presented on the feasibility of CF_4/O_2 plasma-treated PDMS channels to allow actuation and generation of surface-oxidized gallium based liquid metal (oxLM) droplets. A research objective was formulated to make closed channels out of the CF_4/O_2 plasma-treated PDMS surfaces and attempt to pneumatically generate and actuate surface-oxidized liquid metal droplets. This feasibility study was completed and presented in Chapter 4. The results of the study indicate that actuation and generation of oxLM droplets is not feasible due to the mechanical strength of the surface oxide skin.

5.2 Future works

In the area of strain sensors, the next step would be to continue attempts to fabricate the new device design. Previous attempts at fabricating the slotted 2D GMR grating met with difficulties during deposition, patterning, and etching process. For deposition, a uniformity study may be warranted to verify the thickness does not vary more than a few nanometers over the scale of several millimeters. For patterning, an investigation into methods different from raster patterning, which is the method used by electron beam patterning, will help speed up fabrication times and costs. For the etching process, an investigation into achieving anisotropic etching of titanium dioxide thin films for sub-50nm gratings would help towards fabricating the high index part of the slotted grating.

In the area of plasma-treated surfaces, the next step would be to investigate other plasma treatments that etch polymers enough to increase surface roughness. For example, oxygen

plasma etching of various resists have been known to create increased surface roughness, and these surfaces may prove to nonwetting to liquid metals. Argon plasma are known to physically etch surfaces and a study is warranted to see if argon plasma can create rough surfaces to create a nonwetting surface of liquid metals.

In the area of liquid meta microfluidics, the next step would be to find methods to reduce or eliminate the surface oxide without use caustic materials such a s HCl. Additionally, there should also be investigations into methods that can further lower the surface energy of PDMS or any other material from which one can make microfluidic channels. Development of a such methods would help open new application areas in liquid metal microfluidics.

APPENDIX

TUNABLE EXTRAORDINARY OPTICAL TRANSMISSION

The work presented in this section involves a theoretical study and fabrication approach of a tunable plasmonic color filter using the compliant materials liquid metal and PDMS. First, a brief overview of the extraordinary optical transmission (EOT) as a plasmonic phenomenon is provided and the motivation for a tunable EOT device is presented. Next, the optical properties of the liquid metal galinstan is empirically calculated and compared to optical properties of a similar metal used in EOT plasmonics. The design for a tunable EOT color filter is chosen based on an existing plasmonic device made from the metal with optical properties closely resembling that of galinstan. Based on this design, finite element analysis simulations are performed for the device design for rest and strained states. The results of the simulations are presented and analyzed. Based on the promising results of the simulations, a fabrication approach is presented, and its limitations discussed. Lastly, we conclude by summarizing the results and discussing future work.

A.1 Overview of extraordinary optical transmission (EOT)

Extraordinary optical transmission is the observed phenomenon of the enhanced transmission of light through a periodic array of holes in an otherwise optically thick metallic film (Figure A.1a). It was first reported by Ebbesen et al. [143] that when white light is normally incident on to the surface of a 200 nm thick Ag film (on a quartz substrate in air) consisting of a square array of 150 nm diameter holes with a 900 nm period, a transmission peak was measured with 2x the expected intensity at a wavelength of 1370 nm, nearly 10x the hole diameter.

According to Ebbesen et al., “more than twice as much light is transmitted as impinges on the holes...therefore our results must imply that the array itself is an active element...” [143]. Thus, EOT is about the enhanced transmission of light through a hole much smaller than the resonance wavelength. Since that discovery in 1998, there has been significant progress in the theory and experiment of EOT devices in the subsequent two decades, and a review of these milestones can be found in Rodrigo et al. [144]. In terms of recent applications, EOT has been mainly been employed in areas of chemical sensing [145], optical trapping [146], and color filters (Figure A.1b) [147]. It is in the area of color filters that this work is relevant, and it focuses on designing and fabricating a tunable EOT color filter.

The origin of EOT is attributed to the excitation of surface plasmons (Figure A.1c) [148] from electromagnetic radiation interacting with the free electrons at the metal/dielectric surface. Surface plasmons are collective charge oscillations that create surface bound oscillating electromagnetic fields [145], [149]. An incident photon can excite a surface plasmon only if the photon has the same energy and the same momentum component (the component parallel to the surface) to that of an excitable plasmon. Due to these requirements, normal-incident light, which has no component parallel to the surface, cannot induce surface plasmons. However, a periodic array of holes can diffract normally-incident light, and this diffracted light can have momentum with components parallel to the surface, allowing certain plasmons to be excited based on the geometry and periodicity of the hole array. Genet et al. reports for triangular arrays, such as in Figure A.1d, that the peak position at normal incidence is approximated by:

$$\lambda_{max} = \frac{P}{\sqrt{\frac{4}{3}(i^2 + ij + j^2)}} \sqrt{\frac{\epsilon_m \epsilon_d}{\epsilon_m + \epsilon_d}}, \quad (A1)$$

where P is the period of the array, ϵ_m and ϵ_d are the relative permittivities of metal and dielectric material respectively, and i, j are the scattering orders of the array. However, according to Genet et al. equation A1 does not include the effects of interference among the holes and associated scattering losses, and, as a result, the equation predicts wavelength positions slightly less than those observed.

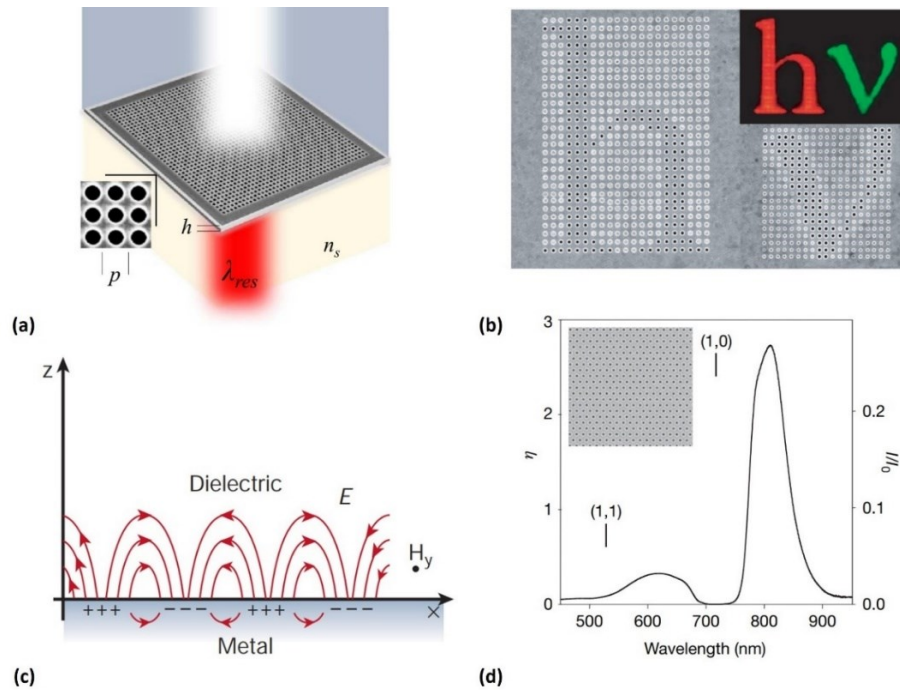


Figure A.1. (a) diagram depicting a metallic hole array on dielectric illuminated by white at normal incidence from Rodrigo et al. [144] © 2016 IEEE; (b) example of EOT from Genet et al. of [150] of two square hole arrays, left array with period 550 nm (red) and right array with period 450 nm (green), in Ag thin film illuminated underneath by white light with transmitted light on the other side © 2007 Nature Publishing Group; (c) diagram of surface plasmon polaritons at metal/dielectric interface from Barnes et al. [148] © 2003 Nature Publishing Group; (d) measured spectrum transmitted under normal-incident white light on to a triangular hole array (170 nm diameter, 520 nm period) milled in 225 nm thick Au film on glass substrate from Genet et al. [150] © 2007 Nature Publishing Group.

Apart from approximately predicting wavelength positions, there is no easy way to analytically determine the intensity profile. Finite element analysis (FEA) methods can provide a

solution to determine the intensity profile and the same reasoning, model, and analysis method used for 2D GMR gratings, described in § 2.3.1, applies. In that FEA model, a unit cell of a 2D grating was implemented as a two-port system, with a top input port acting as a source and a bottom output port for the transmitted waves that exit from the bottom. Apart from changing the grating parameters and material's complex index of refraction the analysis remains the same for a given range of wavelengths. However, there has been no known report on the complex index of refraction values for galinstan, especially for the UV-VIS-NIR region of light, and this will have to be determined in order to perform the simulation.

Recent reports concerning liquid metal plasmonics show there is an effort towards creating plasmonic devices using liquid metal as the material for the hole array grating. In 2012, Wang et al. [151] was the first and only report on the fabrication of a liquid metal-based EOT device operating in the Terahertz (THz) range (Figure A.2). The device was fabricated using the liquid metal EGaIn and PDMS using a basic microfluidic injection process, where the liquid metal is injected into the empty regions of a microfluidic structure made from bonding a flat PDMS sheet to an PDMS sheet with a 15 x 15 array of PDMS pillars with diameter of 357 μ m and period of 714 μ m and height of 80 μ m (Figure A.2a and b). These dimensions correspond to a grating parameter that allow operation in the 0.1 to 0.5 THz range (Figure A.2c), and demonstrates optical tuning by adjusting the period by applied strain (Figure A.2d). To create a similar EOT optical filter that works within the visible region of light – 400 nm (\sim 750 THz) to 700 nm (\sim 428 THz) - the grating parameters would have to be in the submicron scale. This requirement brings with it set of design and fabrication issues that will need to be addressed.

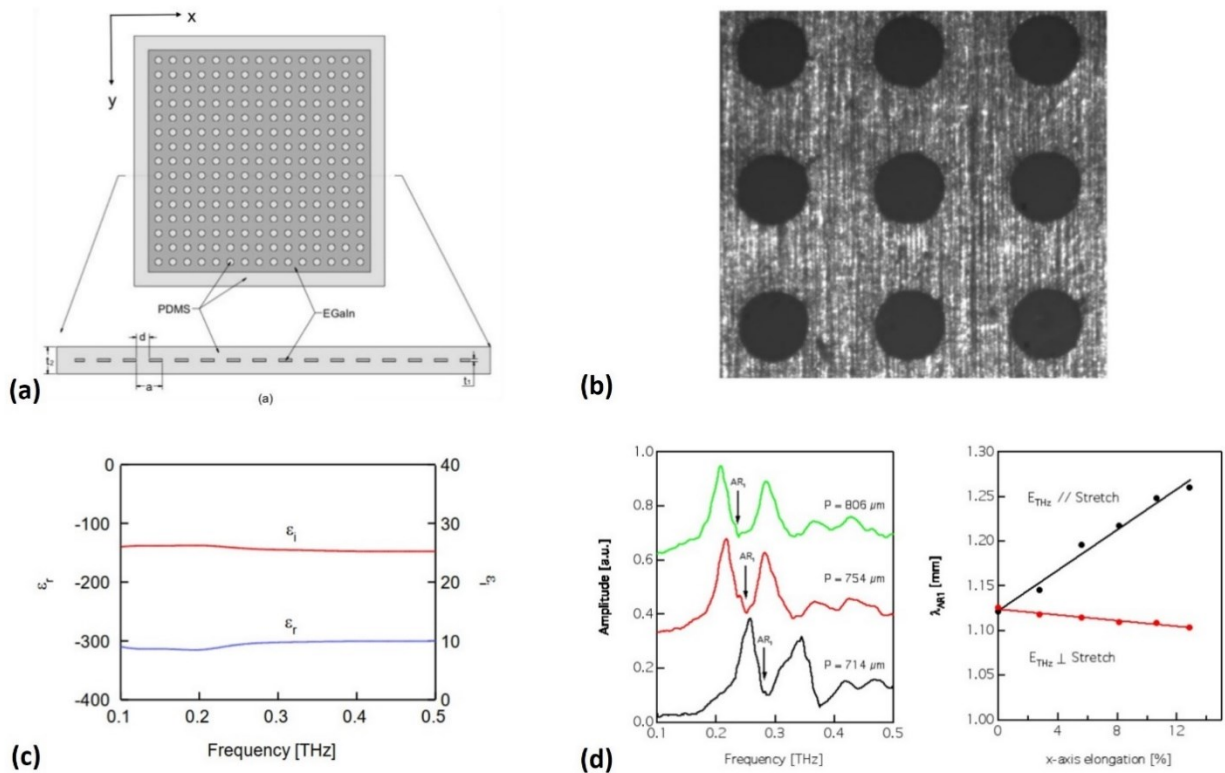


Figure A.2. (a) diagram of 15x15 liquid metal hole array; (b) fabricated EOT optical filter using liquid metal EGaIn embedded in PDMS with hole diameter $357 \mu\text{m}$ and period of $714 \mu\text{m}$ with liquid metal thickness of $80 \mu\text{m}$ and device thickness of 1 mm ; (c) measured complex dielectric constants for EGaIn; and (d) plots of transmission profile at different periods (due to applied strain) (left) and shift in anti-resonance (AR) peak due to applied strain; all images from Wang et al. [151] © 2012 Optical Society of America.

In this work, the complex permittivity of galinstan will be empirically calculated using spectroscopic ellipsometry. This data for galinstan will be incorporated into the material properties of the grating in the simulation model, along with complex permittivity or other metals such as aluminum and gold, so that the accuracy of the simulation can be compared with previously reported EOT-based optical filters. An analysis of the result will support the claim that simulations for devices with new filter designs and material are reasonably accurate. Lastly, an approach to fabrication and its limitation is discussed.

A.2 Complex index of refraction of galinstan

The complex index of refraction ($\tilde{n} = n - ik$) of galinstan was calculated using a Ψ and Δ ellipsometric angles dataset, obtained in the range 350nm to 850nm with 0.6 nm step, at $\varphi = 70^\circ$, using the Sentech 800 automated spectroscopic ellipsometer (SENTECH Instruments GmbH, Berlin, Germany.) The n and k values were calculated by first using the Fresnel equations (A2, A3) obtained from Dieter et al. [152]:

$$A = n_1^2 - k_1^2 = n_0^2 \sin^2(\varphi) \left[1 + \frac{\tan^2(\varphi)[\cos^2(2\Psi) - \sin^2(2\Psi)\sin^2(\Delta)]}{[1 + \sin(2\Psi)\cos(\Delta)]^2} \right], \quad (\text{A2})$$

and,

$$B = 2n_1k_1 = \frac{n_0^2 \sin^2(\varphi) \tan^2(\varphi) \sin(4\Psi) \sin(\Delta)}{[1 + \sin(2\Psi)\cos(\Delta)]^2}, \quad (\text{A3})$$

for each wavelength step, where n_o is the index of refraction of the ambient material surrounding the surface, which, in this case, is air. Next, the following formulas (A4, A5) were used to calculate n and k for each wavelength step:

$$n = \sqrt{\frac{A + \sqrt{A^2 + B^2}}{2}}, \quad (\text{A4})$$

$$k = \sqrt{\frac{-A + \sqrt{A^2 + B^2}}{2}}. \quad (\text{A5})$$

A sample of 10 mm x 10 mm uniformly flat liquid Galinstan[®] is needed to get accurate ellipsometric results. The sample was created by first creating a shallow well in a 3" silicon wafer by etching using the Bosch deep silicon etch (DSE) process. The pattern of the shallow well is 40mm in length and width; the DSE process was performed to obtain a 100 μ m deep etch. A small amount of Galinstan[®] was transferred into the shallow well using a plastic syringe and

gently spread to the edges and corners with a clean plastic swab until a 10mmx10mm uniform flat layer was achieved at the center of the well. The shallow well is used to contain the liquid galinstan; the large area is used to prevent any curvature of the liquid at the edges and corners from affecting the uniformly flat surface at the center. The sample was open to air at room temperature, allowing a few angstroms of gallium oxide to form (see §1.2); however, the effects of the oxide layer on the n and k values of galinstan was not included.

The results of the calculations of the n and k for the complex index of refraction for galinstan are shown in Figure A.3, along with the n and k for the complex index of refraction for aluminum (from refractiveindex.info [153], data collected from report by Rakić et al. [154].)

The n and k curves for galinstan appears similar in trend to that of aluminum, and this similarity is supported by considering that gallium and indium (the major components, ~60% and ~20%, respectively, of galinstan) as well as aluminum are all Group 3A column of elements in the periodic table, and each have three valence electrons in their highest energy orbitals. Since electromagnetic radiation primarily interacts with the valence electrons of an atom, it is reasonable that the complex index of refraction for a group will be similar. This similarity can now be used to select EOT device designs by selecting devices that have aluminum gratings, with the understanding that if the aluminum was replaced by galinstan the device you still produce the same behavior.

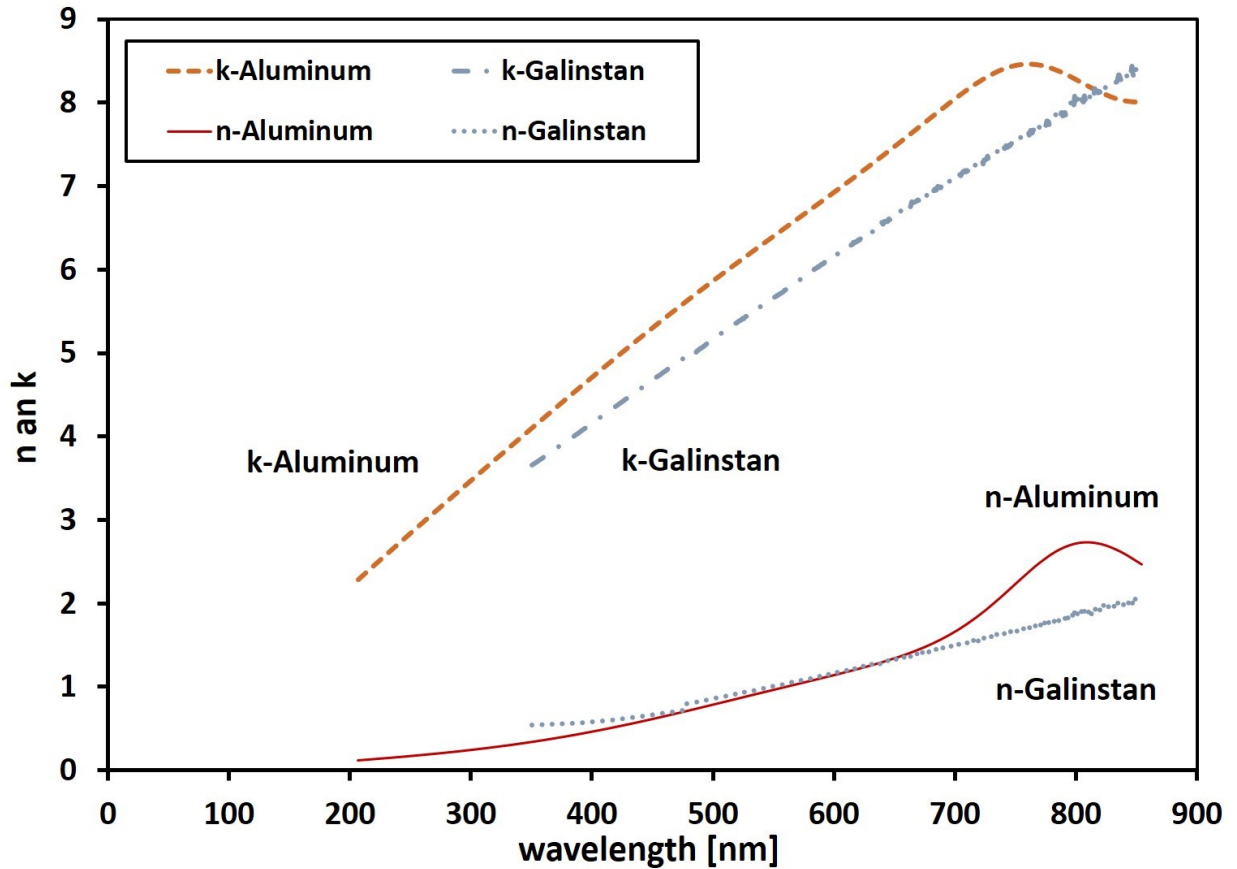


Figure A.1. The n (real part) and k (complex part) of the complex index of refraction for galinstan (calculated empirically) and aluminum from refractiveindex.info [153], data collected from report by Rakić et al. [154].

A.3 Design of tunable color filter

As previously discussed, in order to design a tunable EOT optical filter to operate in the visual region of the electromagnetic spectrum the grating parameters need to be in the submicron range. Since galinstan (or EGaIn) has complex index of refraction similar to that of aluminum, seeking previously fabricated EOT color filter devices that uses aluminum would be excellent foundation on which to base the design. Yokogawa et al. [147] has reported various plasmonic color filters for CMOS image sensor applications fabricated from thin film of aluminum on

quartz substrates (Figure A.4), and these results can be used to help predict the results for a liquid metal/PDMS based EOT device.

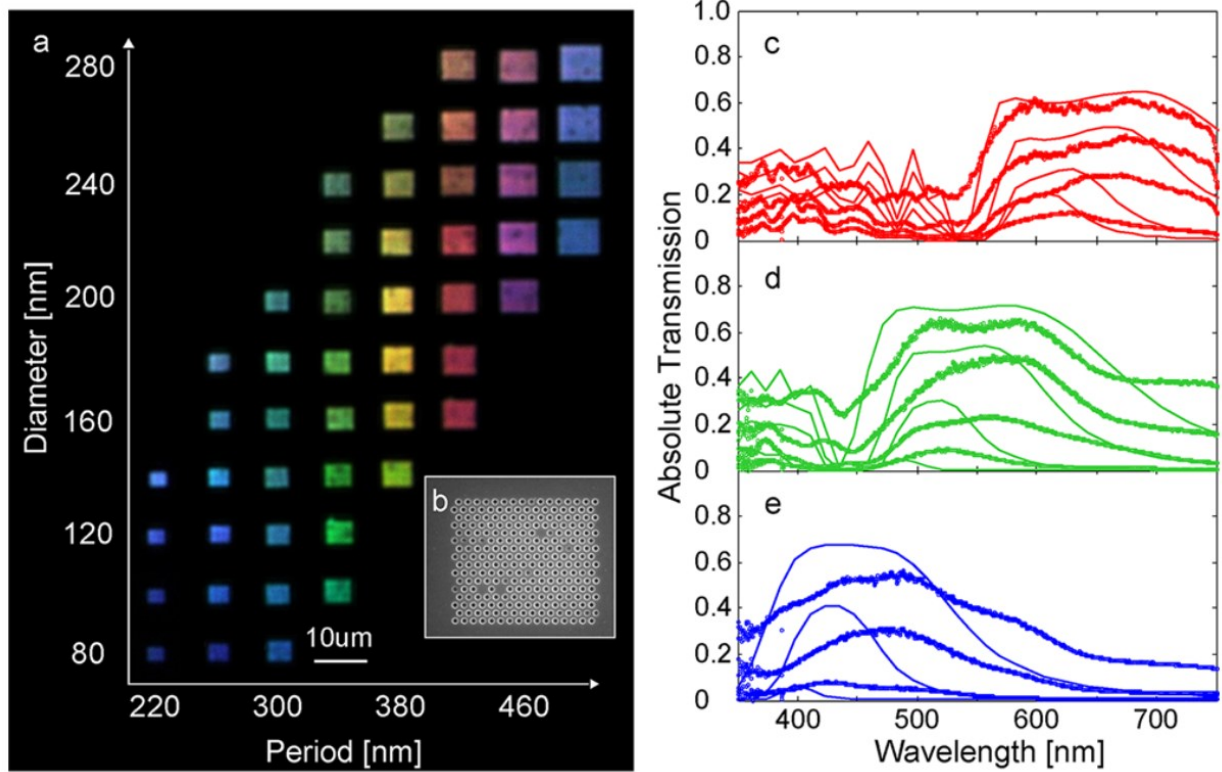


Figure 5.2

Figure A.4. (a) back illuminated plasmonic color filters; (b) SEM micrograph of hexagonal hole array in thin film of aluminum; measured transmission of hole array for (c) red (diameters ranging from 160 nm to 280 nm with period of 420 nm), (d) green (diameters ranging from 120 nm to 240 nm with period of 340 nm), and (e) blue (diameters ranging from 100 nm to 180 nm with period of 260 nm); all images from Yokogawa et al. [147] © 2012 American Chemical Society.

The results of the report (Figure A.4a) show that if a triangular hole array is used (Figure A.4b) and the diameter is kept constant while varying the period, one can more easily transition to different colors with minimal change in the period than by keeping the period constant and varying the diameters (Figure A.4a, c-e). For example, a grating of diameter of 180 nm and period of 340 nm would be expected to produce green light, and simply changing the period to

420 nm would produce red light. The change in period from 340 nm to 420 nm is roughly 23.5% increase, which the elastomer PDMS is quite capable of achieving without breaking. This indicates that a small amount of strain in the plane of a liquid metal/PDMS grating would be enough to behave as a tunable EOT color filter. However, fabricating in the submicron range is more difficult for smaller features, thus there is a benefit for choosing larger diameters and periods.

With these guidelines, one can start simulating the devices with smaller parameters and adjust them to suit a desired wavelength criterion. To set the range of operation within the visible region, the “resting” state wavelength of the tunable EOT color filter was chosen to be 550 nm (green) and the “strained” state wavelength was chosen to be 650 nm (red).

A.4 Simulation of tunable optical filter

All models for both the galinstan/PDMS EOT device design and Yokogawa’s aluminum/SiO₂ EOT device design were simulated using COMSOL[®]. In the models, a unit cell of the triangular array grating was implemented using Floquet periodicity for axial boundary condition matching. The unit cell was set up as a two-port system, with an input port acting as a source of TEM (transverse electric and transverse magnetic) monochromatic light incident along the normal of the 2D grating plane from the top, and an output port of transmitted waves exiting from the bottom (Figure A.5). After assigning either galinstan or aluminum properties to the grating structures of the unit cell (Figure A.5b) and simulating this two-port system over wavelengths ranging from 300 nm to 900 nm in 10 nm steps, the $|S_{21}|$ -parameter was retrieved, i.e. transmission spectrum of each device was calculated.

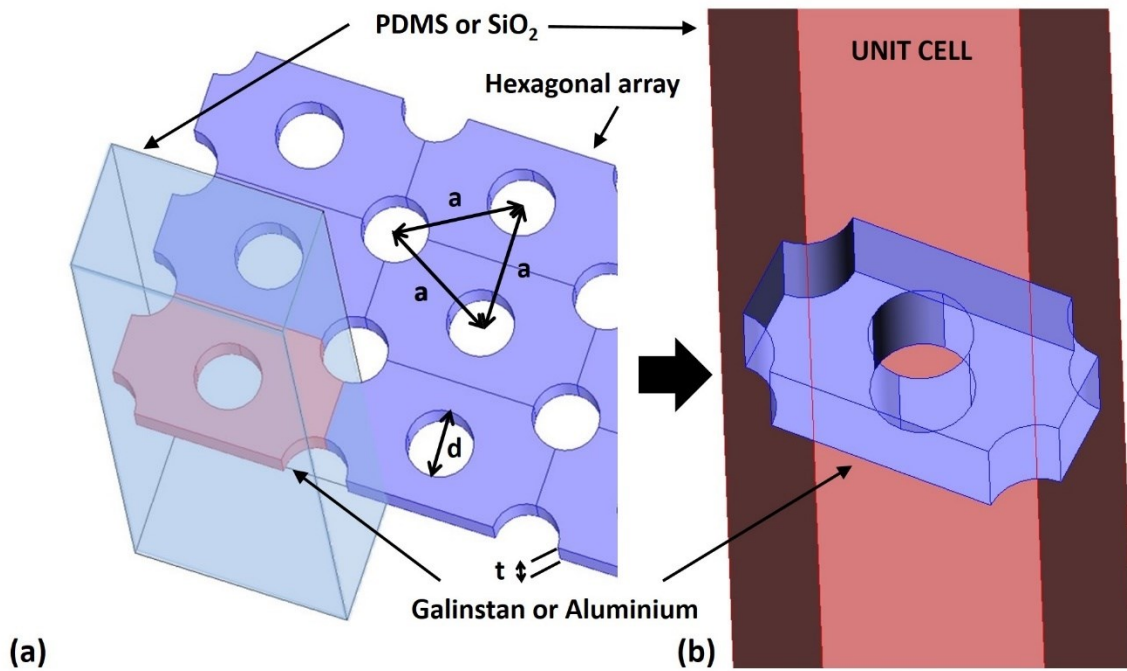


Figure A.5. (a) graphic depicting the hexagonal array consisting of holes with diameter d , period a , and thickness t ; material properties of the superstrate, substrate, and hole can be PDMS or SiO₂; material properties of the grating is galinstan or aluminium; (b) unit cell of the superstrate, hole, and substrate, along with the unit cell of the hexagonal grating.

Example results of the simulations for the resting state (grating parameters of $a = 370$ nm, $d = 196$ nm, $t = 150$ nm, expected to allow transmission of green light) of a PDMS-galinstan-PDMS unit cell are presented in Figure A.6. For green wavelength ($\lambda = 550$ nm) the simulation shows partial transmission of the incident light (Figure A.6a), while for near infrared wavelength ($\lambda = 880$ nm) the simulation shows zero transmission (Figure A.6b), indicating that the simulation produces expected results for an EOT color filter based of liquid metal/PDMS material, and that the results closely match the experimental results the EOT color filter designed by Yokogawa et al. (Figure A.4).

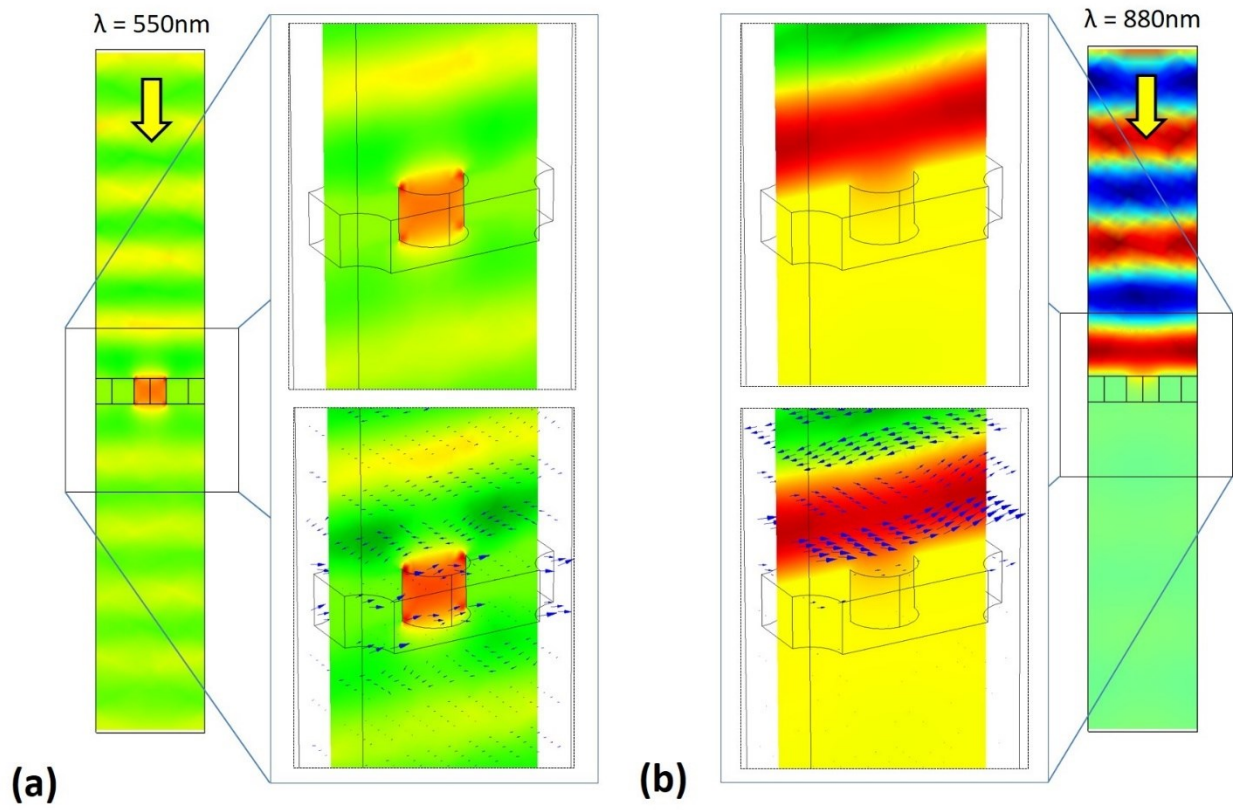


Figure A.6. Simulation example for resting state ($a = 370$ nm, $d = 196$ nm, $t = 150$ nm) PDMS-galinstan-PDMS unit cell for (a) $\lambda = 550$ nm (green) wavelength, which shows partial transmission, and (b) $\lambda = 880$ nm (near infrared) wavelength, which shows no transmission.

A.5 Analysis of simulation results

As mentioned in §A.3, the “resting” state wavelength of the tunable EOT color filter was chosen to be 550 nm (green) and the “strained” state wavelength was chosen to be 650 nm (red). Based on these requirements, the grating parameters for the “resting” state to produce transmission at 550 nm was found to be: $a = 370$ nm and $d = 196$ nm (Figure A.7, —◆— curve.) For the “strained” state to produce 650 nm the grating parameters was found to be: $a = 463$ and $d = 196$ nm, which results in a strain of 25% (Figure A.7, —■— curve.)

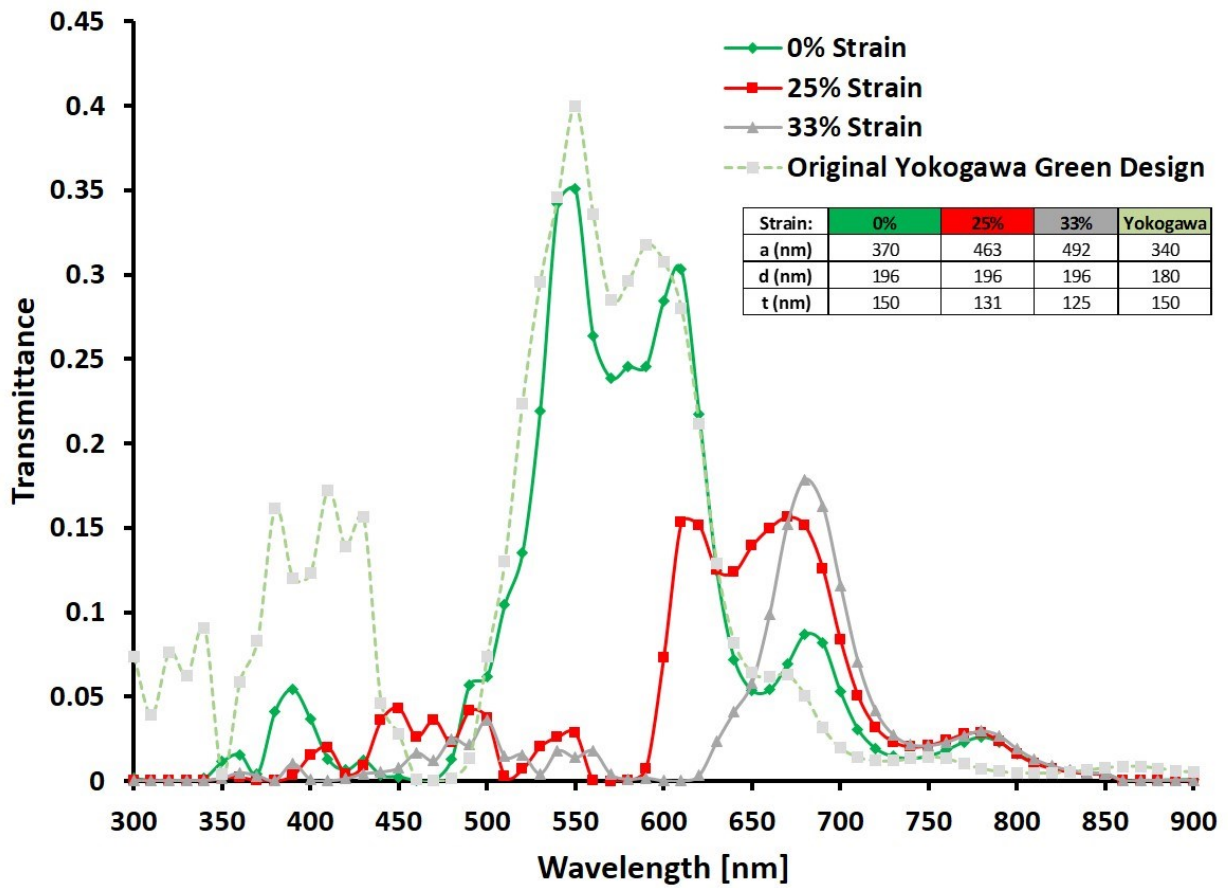


Figure A.7. Transmission spectrum obtained from COMSOL[®] simulations using the RF module. (—◆—) transmittance of “resting” (0% strain) producing resonance peak at 540 nm; (—■—) transmittance of “resting” (25% strain) producing a resonance peak at 610nm and 660 nm overlapping the green peak; (—▲—) transmittance of “resting” (33% strain) producing resonance peak at 690 nm; (---■---) transmittance of the model of the original Yokogawa grating design for green light producing resonance peak at 540 nm, matching that of the PDMS-galinstan-PDMS EOT color filter design.

However, this curve has a significant overlap over the resting state curve, and a 33% strain simulation was done to show that the “resting” state’s green transmission peak and the “strained” state’s red transmission peak are separate and resolvable (Figure A.7, —▲— curve.) To reflect device’s mechanical behavior more accurately, the reduction in device thickness under strain was accounted for. Using the Poisson ratio for PDMS ($\nu = 0.499$) and the strain of 25%

and 33% would result in a thickness of 131 nm and 125nm from the original 150 nm (Figure A.7, table inset.)

To have some comparison, the green color filter ($a = 340$ nm, $d = 180$ nm, $t = 150$ nm) designed by Yokogawa et al. [147] was also simulated (Figure A.7, ---■--- curve.) The transmittance for the simulated Yokogawa et al. model closely matches the PDMS-galinstan-PDMS model (Figure A.7, —◆— curve), and both these simulation results closely match the actual measured results by Yokogawa et al. (Figure A.8). The resonance is centered round 550 nm, with the absolute intensity around 0.4. These comparisons indicate that the simulation results for a liquid metal/PDMS based tunable color filter are reasonably accurate and should produce a similar but broader measured spectrum for green and red, as can be seen in the measured spectrums for green and red grating provided in Figure A.8.

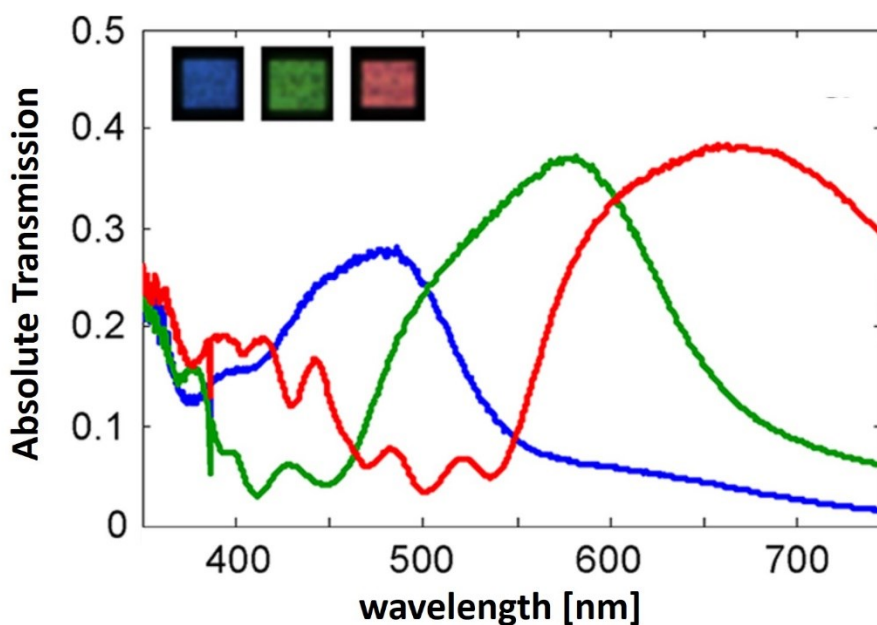


Figure A.8. Transmission spectra for hexagonal hole array filters optimized for red ($p = 420$ nm, $d = 240$ nm), green ($p = 340$ nm, $d = 180$ nm), and blue ($p = 260$ nm, $d = 140$ nm). © 2012 American Chemical Society.

A.6 Fabrication approach and limitations

Fabrication of the tunable EOT color filter requires creating a liquid metal subwavelength hole array, transferring it to a slab of cured PDMS, then pouring uncured PDMS to embed the liquid metal grating within a PDMS superstrate, substrate, and hole region. The process is outlined in Figure A.9.

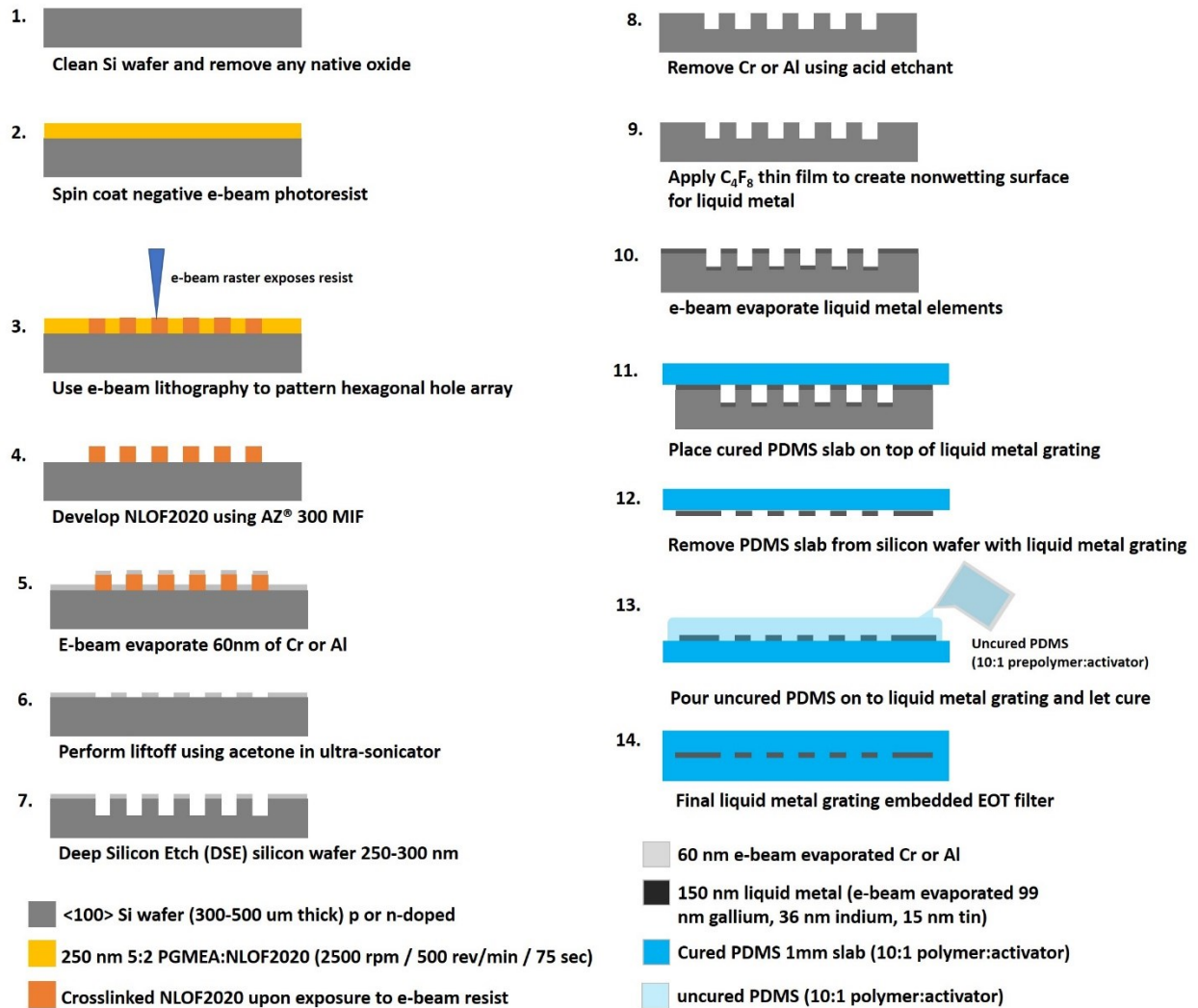


Figure A.9. Outline of process to fabricate liquid metal/PDMS EOT color filter.

Fabrication of the silicon wafer hole array up to step 9 (Figure A.9) was successful (Figure A.10a-d), however e-beam evaporation of the liquid metal elements would randomly form nanoscale droplets due to spontaneous formation of eutectic liquid metal alloy (Figure A.11a, b). These nanoscale droplets form bumps with radius of curvature on the order of the incident wavelengths, and this affects the distance a surface plasmon travels from hole to hole, destroying the grating periodicity. EOT is governed by surface plasmons that travel along the surface and these plasmons rely on the long-range uniform periodicity of the grating holes to create the large-scale effect of EOT. Thus, one may predict that the EOT effect is unlikely to happen due to the formation of the nanodroplet surface bumps. To successfully complete fabrication a method needs to be found to deposit the liquid metal elements on to the silicon substrate at temperatures low enough to keep the thin film solid and uniformly flat until the last step of pouring uncured PDMS. Once the uncured PDMS is cured, the device can be brought to room temperatures to allow the liquid metal alloy to form. However, such process technology was not available at the time.

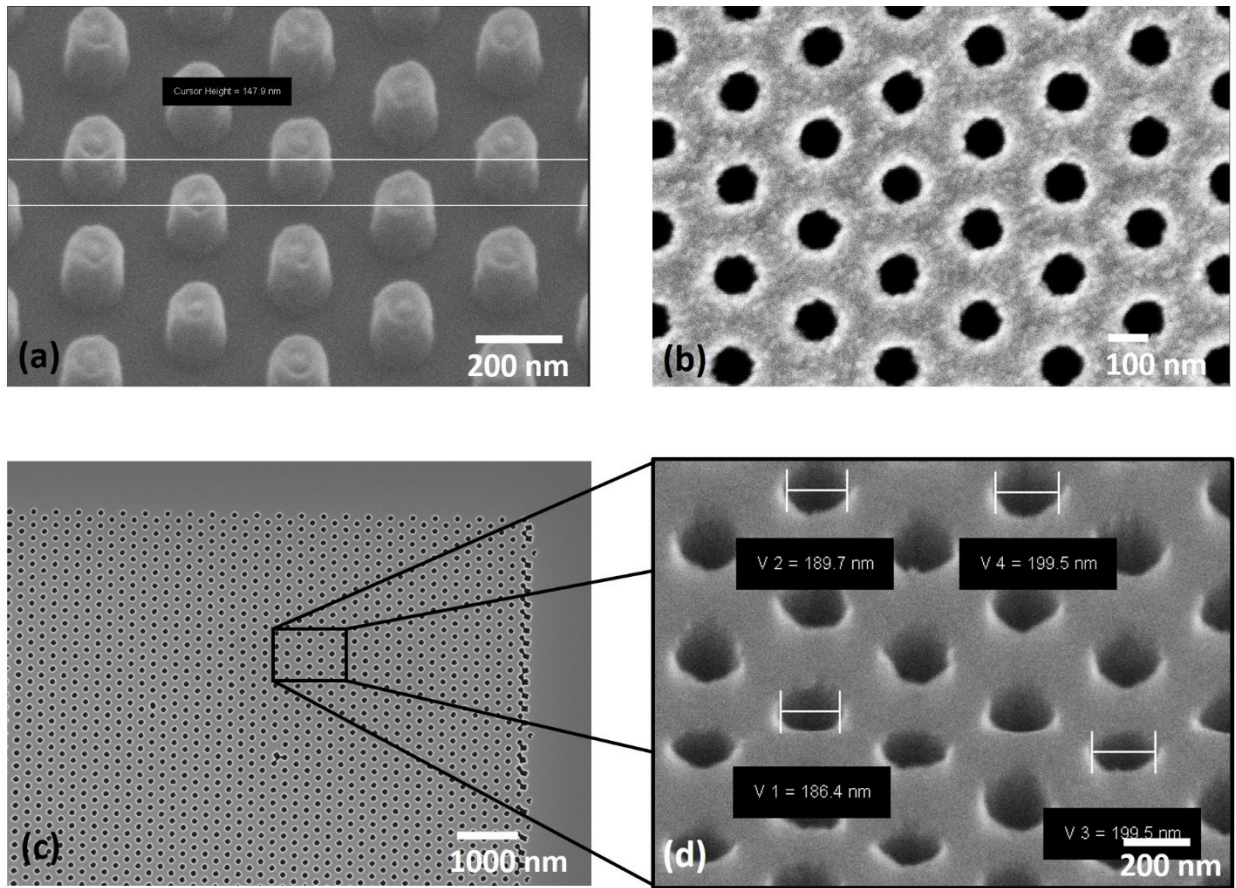


Figure A.10. (a) NLOF2020 hexagonal pillar array fabricated using e-beam lithography (step 4) (b) aluminum hexagonal hole array after liftoff (step 6) (c) hexagonal hole array in silicon (step 8) (d) close-up of hole array in silicon.

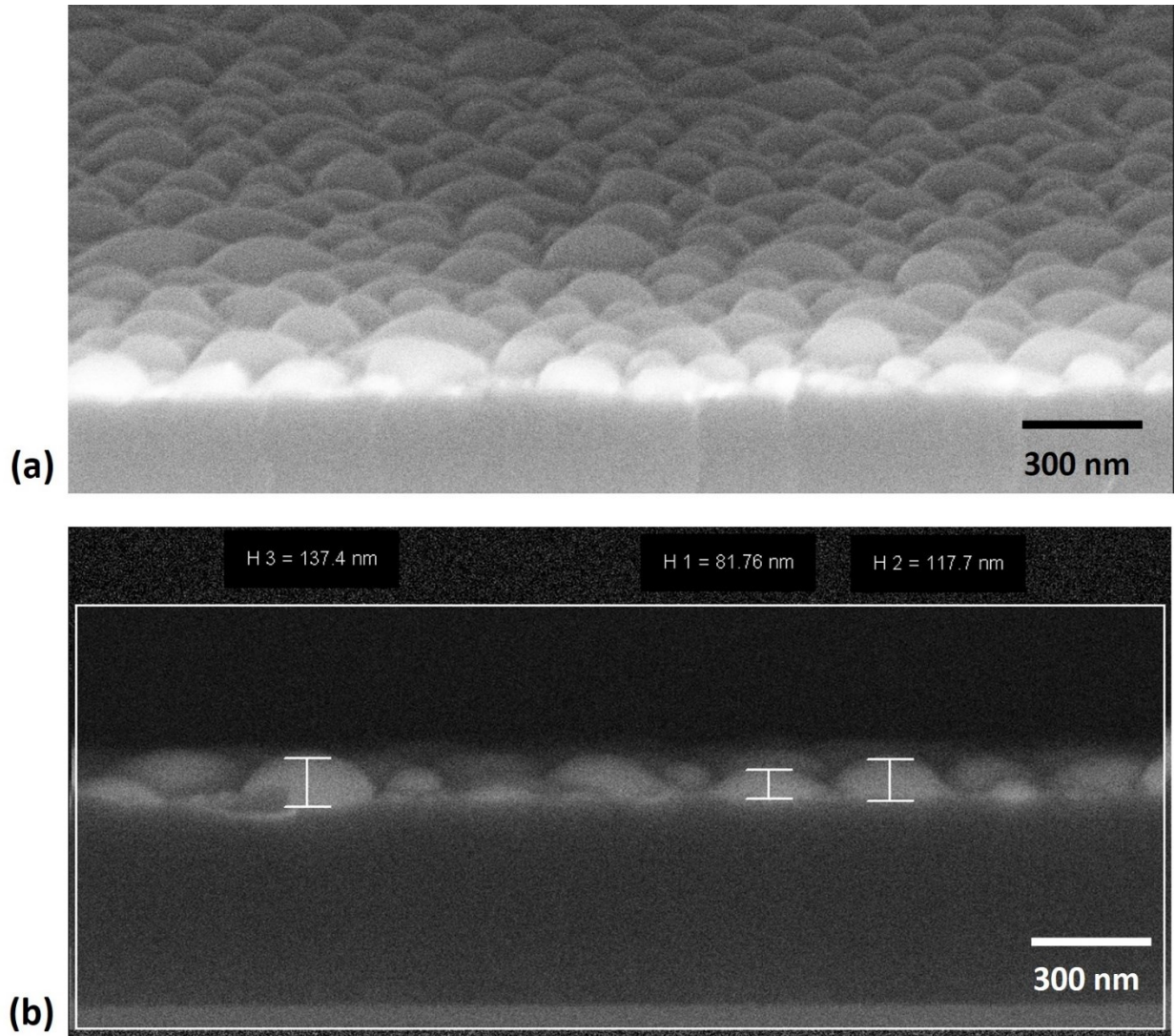


Figure A.11. (a) liquid metal nanodroplet formation after e-beam evaporation of elemental gallium on top of elemental indium on silicon nanohole grating (b) edge view of liquid metal nanodroplets.

A.7 Conclusions and future work

A design for tunable EOT color filter using compliant materials galinstan and PDMS was developed based on existing design using crystalline solid materials. The complex index of refraction of galinstan was empirically determined using spectroscopic ellipsometry and was

found to be similar to aluminum. The complex index of refraction was used in finite element analysis simulations of the EOT color filter design, and the results of the simulations showed a very close match to the same design made from aluminum and SiO₂. Fabrication attempts showed that evaporating elements of the liquid metal to create thin film of liquid metal would result in nanoscale droplets destroys the necessary periodicity required for extraordinary optical transmission. Future work would involve creating a fabrication setup that would keep the silicon hole array substrate cold enough to prevent formation of the nanodroplets until after the thin film of evaporated metals are sealed within PDMS.

REFERENCES

- [1] T. K. Gaylord and M. G. Moharam, "Analysis and applications of optical diffraction by gratings," *Proceedings of the IEEE*, vol. 73, no. 5, pp. 894–937, May 1985, doi: 10.1109/PROC.1985.13220.
- [2] R. Magnusson and S. S. Wang, "New principle for optical filters," *Appl. Phys. Lett.*, vol. 61, no. 9, pp. 1022–1024, Aug. 1992, doi: 10.1063/1.107703.
- [3] S. S. Wang and R. Magnusson, "Theory and applications of guided-mode resonance filters," *Appl. Opt., AO*, vol. 32, no. 14, pp. 2606–2613, May 1993, doi: 10.1364/AO.32.002606.
- [4] S. Tibuleac and R. Magnusson, "Reflection and transmission guided-mode resonance filters," *J. Opt. Soc. Am. A, JOSAA*, vol. 14, no. 7, pp. 1617–1626, Jul. 1997, doi: 10.1364/JOSAA.14.001617.
- [5] R. Magnusson, D. Shin, and Z. S. Liu, "Guided-mode resonance Brewster filter," *Opt. Lett., OL*, vol. 23, no. 8, pp. 612–614, Apr. 1998, doi: 10.1364/OL.23.000612.
- [6] D. Shin, S. Tibuleac, T. A. Maldonado, and R. Magnusson, "Thin-film optical filters with diffractive elements and waveguides," *OE*, vol. 37, no. 9, pp. 2634–2646, Sep. 1998, doi: 10.1117/1.601764.
- [7] Z. S. Liu, S. Tibuleac, D. Shin, P. P. Young, and R. Magnusson, "High-efficiency guided-mode resonance filter," *Opt. Lett., OL*, vol. 23, no. 19, pp. 1556–1558, Oct. 1998, doi: 10.1364/OL.23.001556.
- [8] M. G. Moharam and T. K. Gaylord, "Rigorous coupled-wave analysis of planar-grating diffraction," *J. Opt. Soc. Am., JOSA*, vol. 71, no. 7, pp. 811–818, Jul. 1981, doi: 10.1364/JOSA.71.000811.
- [9] D. Fattal, J. Li, Z. Peng, M. Fiorentino, and R. G. Beausoleil, "Flat dielectric grating reflectors with focusing abilities," *Nature Photonics*, vol. 4, no. 7, Art. no. 7, Jul. 2010, doi: 10.1038/nphoton.2010.116.
- [10] S. J. Foland, "Theory and design of a tunable guided-mode resonance sensor," M.S., The University of Texas at Dallas, United States -- Texas, 2010.
- [11] M.-L. Wu *et al.*, "Authentication labels based on guided-mode resonant filters," *Opt. Lett., OL*, vol. 32, no. 12, pp. 1614–1616, Jun. 2007, doi: 10.1364/OL.32.001614.
- [12] S. Tibuleac, P. P. Young, R. Magnusson, and T. R. Holzheimer, "Experimental verification of waveguide-mode resonant transmission filters," *IEEE Microwave and Guided Wave Letters*, vol. 9, no. 1, pp. 19–21, Jan. 1999, doi: 10.1109/75.752111.

- [13] J. A. Cox, R. A. Morgan, R. M. Wilke, and C. M. Ford, "Guided-mode grating resonant filters for VCSEL applications," in *Diffraction and Holographic Device Technologies and Applications V*, Jun. 1998, vol. 3291, pp. 70–76, doi: 10.1117/12.310571.
- [14] C. J. Chang-Hasnain, Y. Zhou, M. C. Y. Huang, and C. Chase, "High-Contrast Grating VCSELs," *IEEE Journal of Selected Topics in Quantum Electronics*, vol. 15, no. 3, pp. 869–878, May 2009, doi: 10.1109/JSTQE.2009.2015195.
- [15] J. H. Schmid *et al.*, "Silicon-on-insulator guided mode resonant grating for evanescent field molecular sensing," *Opt. Express, OE*, vol. 17, no. 20, pp. 18371–18380, Sep. 2009, doi: 10.1364/OE.17.018371.
- [16] D. Wawro, P. Koulen, Y. Ding, S. Zimmerman, and R. Magnusson, "Guided-mode resonance sensor system for early detection of ovarian cancer," in *Optical Diagnostics and Sensing X: Toward Point-of-Care Diagnostics*, Feb. 2010, vol. 7572, p. 75720D, doi: 10.1117/12.842725.
- [17] W.-J. Kim *et al.*, "Response to Cardiac Markers in Human Serum Analyzed by Guided-Mode Resonance Biosensor," *Anal. Chem.*, vol. 82, no. 23, pp. 9686–9693, Dec. 2010, doi: 10.1021/ac101716p.
- [18] S. J. Foland and J. Lee, "A highly-compliant asymmetric 2D guided-mode resonance sensor for simultaneous measurement of dual-axis strain," in *2013 IEEE 26th International Conference on Micro Electro Mechanical Systems (MEMS)*, Jan. 2013, pp. 665–668, doi: 10.1109/MEMSYS.2013.6474329.
- [19] M. D. Dickey, R. C. Chiechi, R. J. Larsen, E. A. Weiss, D. A. Weitz, and G. M. Whitesides, "Eutectic Gallium-Indium (EGaIn): A Liquid Metal Alloy for the Formation of Stable Structures in Microchannels at Room Temperature," *Advanced Functional Materials*, vol. 18, no. 7, pp. 1097–1104, 2008, doi: <https://doi.org/10.1002/adfm.200701216>.
- [20] T. Liu, P. Sen, and C.-J. Kim, "Characterization of Nontoxic Liquid-Metal Alloy Galinstan for Applications in Microdevices," *Journal of Microelectromechanical Systems*, vol. 21, no. 2, pp. 443–450, Apr. 2012, doi: 10.1109/JMEMS.2011.2174421.
- [21] L. C. Cadwallader, "Gallium Safety in the Laboratory," Idaho National Engineering and Environmental Laboratory, Idaho Falls, ID (US), INEEL/CON-03-00078, May 2003. Accessed: Jan. 24, 2021. [Online]. Available: <https://www.osti.gov/biblio/811932>.
- [22] G. Speckbrock, "Metallic gallium alloy as a thermometer fluid," DE10321843A1, Dec. 09, 2004.
- [23] M. D. Dickey, "Stretchable and Soft Electronics using Liquid Metals," *Advanced Materials*, vol. 29, no. 27, p. 1606425, 2017, doi: 10.1002/adma.201606425.

- [24] W. Gao, H. Ota, D. Kiriya, K. Takei, and A. Javey, “Flexible Electronics toward Wearable Sensing,” *Acc. Chem. Res.*, vol. 52, no. 3, pp. 523–533, Mar. 2019, doi: 10.1021/acs.accounts.8b00500.
- [25] L. Wang and J. Liu, “Liquid Metal Inks for Flexible Electronics and 3D Printing: A Review,” presented at the ASME 2014 International Mechanical Engineering Congress and Exposition, Mar. 2015, doi: 10.1115/IMECE2014-37993.
- [26] W. G. Tonaki, W. Hu, A. T. Ohta, and W. A. Shiroma, “A reconfigurable, liquid-metal-based low-pass filter with reversible tuning,” in *2013 IEEE International Wireless Symposium (IWS)*, Apr. 2013, pp. 1–3, doi: 10.1109/IEEE-IWS.2013.6616802.
- [27] D. Kim, R. G. Pierce, R. Henderson, S. J. Doo, K. Yoo, and J.-B. Lee, “Liquid metal actuation-based reversible frequency tunable monopole antenna,” *Appl. Phys. Lett.*, vol. 105, no. 23, p. 234104, Dec. 2014, doi: 10.1063/1.4903882.
- [28] S. Cheng and Z. Wu, “Microfluidic electronics,” *Lab Chip*, vol. 12, no. 16, pp. 2782–2791, Jul. 2012, doi: 10.1039/C2LC21176A.
- [29] D. Kim, “Microfluidic platforms for gallium-based liquid metal alloy,” University of Texas at Dallas, 2014.
- [30] D. Kim *et al.*, “Recovery of Nonwetting Characteristics by Surface Modification of Gallium-Based Liquid Metal Droplets Using Hydrochloric Acid Vapor,” *ACS Appl. Mater. Interfaces*, vol. 5, no. 1, pp. 179–185, Jan. 2013, doi: 10.1021/am302357t.
- [31] K. Doudrick *et al.*, “Different Shades of Oxide: From Nanoscale Wetting Mechanisms to Contact Printing of Gallium-Based Liquid Metals,” *Langmuir*, vol. 30, no. 23, pp. 6867–6877, Jun. 2014, doi: 10.1021/la5012023.
- [32] F. Scharmann *et al.*, “Viscosity effect on GaInSn studied by XPS,” *Surface and Interface Analysis*, vol. 36, no. 8, pp. 981–985, 2004, doi: 10.1002/sia.1817.
- [33] C. Ladd, J.-H. So, J. Muth, and M. D. Dickey, “3D Printing of Free Standing Liquid Metal Microstructures,” *Advanced Materials*, vol. 25, no. 36, pp. 5081–5085, 2013, doi: 10.1002/adma.201301400.
- [34] Q. Xu, N. Oudalov, Q. Guo, H. M. Jaeger, and E. Brown, “Effect of oxidation on the mechanical properties of liquid gallium and eutectic gallium-indium,” *Physics of Fluids*, vol. 24, no. 6, p. 063101, Jun. 2012, doi: 10.1063/1.4724313.
- [35] R. J. Larsen, M. D. Dickey, G. M. Whitesides, and D. A. Weitz, “Viscoelastic properties of oxide-coated liquid metals,” *Journal of Rheology*, vol. 53, no. 6, pp. 1305–1326, Nov. 2009, doi: 10.1122/1.3236517.

- [36] G. Li, M. Parmar, D. Kim, Jeong-Bong (JB) Lee, and D.-W. Lee, “PDMS based coplanar microfluidic channels for the surface reduction of oxidized Galinstan,” *Lab on a Chip*, vol. 14, no. 1, pp. 200–209, 2014, doi: 10.1039/C3LC50952D.
- [37] S. Babu and J.-B. Lee, “Plasma-Treated PDMS as Intrinsically Non-Wetting Surface for Gallium-Alloy Liquid Metal Microfluidics,” in *2020 IEEE 33rd International Conference on Micro Electro Mechanical Systems (MEMS)*, Jan. 2020, pp. 1122–1125, doi: 10.1109/MEMS46641.2020.9056134.
- [38] J. Simon, S. Saffer, and C.- Kim, “A liquid-filled microrelay with a moving mercury microdrop,” *Journal of Microelectromechanical Systems*, vol. 6, no. 3, pp. 208–216, Sep. 1997, doi: 10.1109/84.623109.
- [39] Junghoon Lee and C.-C. Kim, “Liquid micromotor driven by continuous electrowetting,” in *Proceedings MEMS 98. IEEE. Eleventh Annual International Workshop on Micro Electro Mechanical Systems. An Investigation of Micro Structures, Sensors, Actuators, Machines and Systems (Cat. No.98CH36176)*, Jan. 1998, pp. 538–543, doi: 10.1109/MEMSYS.1998.659815.
- [40] L. Latorre *et al.*, “Electrostatic actuation of microscale liquid-metal droplets,” *Journal of Microelectromechanical Systems*, vol. 11, no. 4, pp. 302–308, Aug. 2002, doi: 10.1109/JMEMS.2002.800934.
- [41] J. Kim, W. Shen, L. Latorre, and C.-J. Kim, “A micromechanical switch with electrostatically driven liquid-metal droplet,” *Sensors and Actuators A: Physical*, vol. 97–98, pp. 672–679, Apr. 2002, doi: 10.1016/S0924-4247(02)00022-5.
- [42] W. Shen, R. T. Edwards, and Chang-Jin Kim, “Mercury droplet microswitch for re-configurable circuit interconnect,” in *TRANSDUCERS '03. 12th International Conference on Solid-State Sensors, Actuators and Microsystems. Digest of Technical Papers (Cat. No.03TH8664)*, Jun. 2003, vol. 1, pp. 464–467 vol.1, doi: 10.1109/SENSOR.2003.1215354.
- [43] M. Knoblauch, J. M. Hibberd, J. C. Gray, and A. J. E. van Bel, “A galinstan expansion femtosyringe for microinjection of eukaryotic organelles and prokaryotes,” *Nature Biotechnology*, vol. 17, no. 9, Art. no. 9, Sep. 1999, doi: 10.1038/12902.
- [44] K. Niayesh, J. Tepper, and F. Konig, “A novel current limitation principle based on application of liquid metals,” *IEEE Transactions on Components and Packaging Technologies*, vol. 29, no. 2, pp. 303–309, Jun. 2006, doi: 10.1109/TCAPT.2006.875880.
- [45] C. Chen, J. Whalen, and D. Peroulis, “Non-Toxic Liquid-Metal 2-100 GHz MEMS Switch,” in *2007 IEEE/MTT-S International Microwave Symposium*, Jun. 2007, pp. 363–366, doi: 10.1109/MWSYM.2007.380446.

- [46] R. C. Gough, A. M. Morishita, J. H. Dang, W. Hu, W. A. Shiroma, and A. T. Ohta, “Continuous Electrowetting of Non-toxic Liquid Metal for RF Applications,” *IEEE Access*, vol. 2, pp. 874–882, 2014, doi: 10.1109/ACCESS.2014.2350531.
- [47] D. Kim, D.-W. Lee, W. Choi, and J.-B. Lee, “A Super-Lyophobic 3-D PDMS Channel as a Novel Microfluidic Platform to Manipulate Oxidized Galinstan,” *Journal of Microelectromechanical Systems*, vol. 22, no. 6, pp. 1267–1275, Dec. 2013, doi: 10.1109/JMEMS.2013.2278625.
- [48] I. D. Joshipura *et al.*, “Patterning and Reversible Actuation of Liquid Gallium Alloys by Preventing Adhesion on Rough Surfaces,” *ACS Appl. Mater. Interfaces*, vol. 10, no. 51, pp. 44686–44695, Dec. 2018, doi: 10.1021/acsami.8b13099.
- [49] Z. Chen and J. B. Lee, “Surface Modification with Gallium Coating as Nonwetting Surfaces for Gallium-Based Liquid Metal Droplet Manipulation,” *ACS Appl. Mater. Interfaces*, vol. 11, no. 38, pp. 35488–35495, Sep. 2019, doi: 10.1021/acsami.9b12493.
- [50] T. Hutter, W.-A. C. Bauer, S. R. Elliott, and W. T. S. Huck, “Formation of Spherical and Non-Spherical Eutectic Gallium-Indium Liquid-Metal Microdroplets in Microfluidic Channels at Room Temperature,” *Advanced Functional Materials*, vol. 22, no. 12, pp. 2624–2631, 2012, doi: <https://doi.org/10.1002/adfm.201200324>.
- [51] M. R. Khan, C. Trlica, J.-H. So, M. Valeri, and M. D. Dickey, “Influence of Water on the Interfacial Behavior of Gallium Liquid Metal Alloys,” *ACS Appl. Mater. Interfaces*, vol. 6, no. 24, pp. 22467–22473, Dec. 2014, doi: 10.1021/am506496u.
- [52] D. Kim, J. H. Yoo, Y. Lee, W. Choi, K. Yoo, and J.-B. Lee, “Gallium-based liquid metal inkjet printing,” in *2014 IEEE 27th International Conference on Micro Electro Mechanical Systems (MEMS)*, Jan. 2014, pp. 967–970, doi: 10.1109/MEMSYS.2014.6765804.
- [53] G. Li, M. Parmar, and D.-W. Lee, “An oxidized liquid metal-based microfluidic platform for tunable electronic device applications,” *Lab Chip*, vol. 15, no. 3, pp. 766–775, Jan. 2015, doi: 10.1039/C4LC01013B.
- [54] C. I. Merzbacher, A. D. Kersey, and E. J. Friebele, “Fiber optic sensors in concrete structures: a review,” *Smart Mater. Struct.*, vol. 5, no. 2, pp. 196–208, Apr. 1996, doi: 10.1088/0964-1726/5/2/008.
- [55] M. Amjadi, K.-U. Kyung, I. Park, and M. Sitti, “Stretchable, Skin-Mountable, and Wearable Strain Sensors and Their Potential Applications: A Review,” *Advanced Functional Materials*, vol. 26, no. 11, pp. 1678–1698, 2016, doi: <https://doi.org/10.1002/adfm.201504755>.
- [56] J. Fraden, “Pressure Sensors,” in *Handbook of Modern Sensors: Physics, Designs, and Applications*, J. Fraden, Ed. Cham: Springer International Publishing, 2016, pp. 429–451.

- [57] B. Lee, "Review of the present status of optical fiber sensors," *Optical Fiber Technology*, vol. 9, no. 2, pp. 57–79, Apr. 2003, doi: 10.1016/S1068-5200(02)00527-8.
- [58] S. S. Wang, R. Magnusson, J. S. Bagby, and M. G. Moharam, "Guided-mode resonances in planar dielectric-layer diffraction gratings," *J. Opt. Soc. Am. A, JOSAA*, vol. 7, no. 8, pp. 1470–1474, Aug. 1990, doi: 10.1364/JOSAA.7.001470.
- [59] A. Sharon, D. Rosenblatt, A. A. Friesem, H. G. Weber, H. Engel, and R. Steingrueber, "Light modulation with resonant grating-waveguide structures," *Opt. Lett., OL*, vol. 21, no. 19, pp. 1564–1566, Oct. 1996, doi: 10.1364/OL.21.001564.
- [60] H.-T. Chen, W. J. Padilla, J. M. O. Zide, A. C. Gossard, A. J. Taylor, and R. D. Averitt, "Active terahertz metamaterial devices," *Nature*, vol. 444, no. 7119, Art. no. 7119, Nov. 2006, doi: 10.1038/nature05343.
- [61] I. Abdulhalim, "Optimized guided mode resonant structure as thermo-optic sensor and liquid crystal tunable filter," *Chin. Opt. Lett., COL*, vol. 7, no. 8, pp. 667–670, Aug. 2009.
- [62] J. A. Giese, J. W. Yoon, B. R. Wenner, J. W. Allen, M. S. Allen, and R. Magnusson, "Guided-mode resonant coherent light absorbers," *Opt. Lett., OL*, vol. 39, no. 3, pp. 486–488, Feb. 2014, doi: 10.1364/OL.39.000486.
- [63] Y.-C. Lee, C.-F. Huang, J.-Y. Chang, and M.-L. Wu, "Enhanced light trapping based on guided mode resonance effect for thin-film silicon solar cells with two filling-factor gratings," *Opt. Express, OE*, vol. 16, no. 11, pp. 7969–7975, May 2008, doi: 10.1364/OE.16.007969.
- [64] T. Khaleque and R. Magnusson, "Light management through guided-mode resonances in thin-film silicon solar cells," *JNP*, vol. 8, no. 1, p. 083995, Mar. 2014, doi: 10.1117/1.JNP.8.083995.
- [65] O. Krasnykov, M. Auslender, and I. Abdulhalim, "Optimizing the guided mode resonant structure for optical sensing in water," vol. 1, no. 3, p. 8, 2011.
- [66] J.-N. Yih *et al.*, "Optical waveguide biosensors constructed with subwavelength gratings," *Appl. Opt., AO*, vol. 45, no. 9, pp. 1938–1942, Mar. 2006, doi: 10.1364/AO.45.001938.
- [67] N. L. Privorotskaya, C. J. Choi, B. T. Cunningham, and W. P. King, "Sensing micrometer-scale deformations via stretching of a photonic crystal," *Sensors and Actuators A: Physical*, vol. 161, no. 1, pp. 66–71, Jun. 2010, doi: 10.1016/j.sna.2010.05.024.
- [68] S. Foland, K.-H. Choi, and J.-B. Lee, "Pressure-tunable guided-mode resonance sensor for single-wavelength characterization," *Opt. Lett., OL*, vol. 35, no. 23, pp. 3871–3873, Dec. 2010, doi: 10.1364/OL.35.003871.

- [69] D. Cai, A. Neyer, R. Kuckuk, and H. M. Heise, “Raman, mid-infrared, near-infrared and ultraviolet–visible spectroscopy of PDMS silicone rubber for characterization of polymer optical waveguide materials,” *Journal of Molecular Structure*, vol. 976, no. 1, pp. 274–281, Jul. 2010, doi: 10.1016/j.molstruc.2010.03.054.
- [70] K.-C. Chen, A. Wo, and Y. Chen, “Transmission Spectrum of PDMS in 4-7 μ m Mid-IR Range for Characterization of Protein Structure,” *undefined*, 2006. /paper/Transmission-Spectrum-of-PDMS-in-4-7% μ m-Mid-IR-Range-Chen-Wo/4e0326317a33ed10389a8da120267fd3e2f7ac06 (accessed Jan. 10, 2021).
- [71] F. Schneider, J. Draheim, R. Kamberger, and U. Wallrabe, “Process and material properties of polydimethylsiloxane (PDMS) for Optical MEMS,” *Sensors and Actuators A: Physical*, vol. 151, no. 2, pp. 95–99, Apr. 2009, doi: 10.1016/j.sna.2009.01.026.
- [72] S. Foland, K. Liu, D. MacFarlane, and J. Lee, “High-sensitivity microfluidic pressure sensor using a membrane-embedded resonant optical grating,” in *2011 IEEE SENSORS*, Oct. 2011, pp. 101–104, doi: 10.1109/ICSENS.2011.6127285.
- [73] C. Fang *et al.*, “Tunable guided-mode resonance filter with a gradient grating period fabricated by casting a stretched PDMS grating wedge,” *Opt. Lett., OL*, vol. 41, no. 22, pp. 5302–5305, Nov. 2016, doi: 10.1364/OL.41.005302.
- [74] S. Sarkar, S. Poulouse, P. K. Sahoo, and J. Joseph, “Flexible and stretchable guided-mode resonant optical sensor: single-step fabrication on a surface engineered polydimethylsiloxane substrate,” *OSA Continuum, OSAC*, vol. 1, no. 4, pp. 1277–1286, Dec. 2018, doi: 10.1364/OSAC.1.001277.
- [75] T. Fujii, “PDMS-based microfluidic devices for biomedical applications,” *Microelectronic Engineering*, vol. 61–62, pp. 907–914, Jul. 2002, doi: 10.1016/S0167-9317(02)00494-X.
- [76] S. J. Foland and J. B. Lee, “Highly compliant resonant diffraction gratings, and methods and use thereof,” US9234991B2, Jan. 12, 2016.
- [77] O. Anderson, C. R. Ottermann, R. Kuschnerreit, P. Hess, and K. Bange, “Density and Young’s modulus of thin TiO₂ films,” *Fresenius J Anal Chem*, vol. 358, no. 1, pp. 315–318, May 1997, doi: 10.1007/s002160050416.
- [78] D. Armani, C. Liu, and N. Aluru, “Re-configurable fluid circuits by PDMS elastomer micromachining,” in *Technical Digest. IEEE International MEMS 99 Conference. Twelfth IEEE International Conference on Micro Electro Mechanical Systems (Cat. No.99CH36291)*, Jan. 1999, pp. 222–227, doi: 10.1109/MEMSYS.1999.746817.
- [79] S. Isaacs, A. Hajoj, M. Abutoama, A. Kozlovsky, E. Golan, and I. Abdulhalim, “Resonant Grating without a Planar Waveguide Layer as a Refractive Index Sensor,” *Sensors*, vol. 19, no. 13, Art. no. 13, Jan. 2019, doi: 10.3390/s19133003.

- [80] S. Fan and J. D. Joannopoulos, “Analysis of guided resonances in photonic crystal slabs,” *Phys. Rev. B*, vol. 65, no. 23, p. 235112, Jun. 2002, doi: 10.1103/PhysRevB.65.235112.
- [81] P. Pottier, L. Shi, and Y.-A. Peter, “Determination of guided-mode resonances in photonic crystal slabs,” *J. Opt. Soc. Am. B, JOSAB*, vol. 29, no. 1, pp. 109–117, Jan. 2012, doi: 10.1364/JOSAB.29.000109.
- [82] D. Fattal, M. Sigalas, A. Pyayt, Z. Li, and R. G. Beausoleil, “Guided-mode resonance sensor with extended spatial sensitivity,” in *Active Photonic Crystals*, Sep. 2007, vol. 6640, p. 66400M, doi: 10.1117/12.731928.
- [83] L. C. Andreani and D. Gerace, “Photonic-crystal slabs with a triangular lattice of triangular holes investigated using a guided-mode expansion method,” *Phys. Rev. B*, vol. 73, no. 23, p. 235114, Jun. 2006, doi: 10.1103/PhysRevB.73.235114.
- [84] H. Hemmati and R. Magnusson, “Development of tuned refractive-index nanocomposites to fabricate nanoimprinted optical devices,” *Opt. Mater. Express, OME*, vol. 8, no. 1, pp. 175–183, Jan. 2018, doi: 10.1364/OME.8.000175.
- [85] P. Lalanne and D. Lemerrier-lalanne, “On the effective medium theory of subwavelength periodic structures,” *Journal of Modern Optics*, vol. 43, no. 10, pp. 2063–2085, Oct. 1996, doi: 10.1080/09500349608232871.
- [86] A. Yariv and P. Yeh, “Electromagnetic propagation in periodic stratified media. II. Birefringence, phase matching, and x-ray lasers *,” *J. Opt. Soc. Am., JOSAA*, vol. 67, no. 4, pp. 438–447, Apr. 1977, doi: 10.1364/JOSA.67.000438.
- [87] D. C. Flanders, “Submicrometer periodicity gratings as artificial anisotropic dielectrics,” *Appl. Phys. Lett.*, vol. 42, no. 6, pp. 492–494, Mar. 1983, doi: 10.1063/1.93979.
- [88] E. B. Grann, M. G. Moharam, and D. A. Pommet, “Artificial uniaxial and biaxial dielectrics with use of two-dimensional subwavelength binary gratings,” *J. Opt. Soc. Am. A, JOSAA*, vol. 11, no. 10, pp. 2695–2703, Oct. 1994, doi: 10.1364/JOSAA.11.002695.
- [89] H. Kikuta, Y. Ohira, H. Kubo, and K. Iwata, “Effective medium theory of two-dimensional subwavelength gratings in the non-quasi-static limit,” *J. Opt. Soc. Am. A, JOSAA*, vol. 15, no. 6, pp. 1577–1585, Jun. 1998, doi: 10.1364/JOSAA.15.001577.
- [90] P. Lalanne and D. Lemerrier-Lalanne, “Depth dependence of the effective properties of subwavelength gratings,” *J. Opt. Soc. Am. A, JOSAA*, vol. 14, no. 2, pp. 450–459, Feb. 1997, doi: 10.1364/JOSAA.14.000450.
- [91] M. G. Moharam, “Coupled-Wave Analysis Of Two-Dimensional Dielectric Gratings,” in *Holographic Optics: Design and Applications*, Apr. 1988, vol. 0883, pp. 8–11, doi: 10.1117/12.944119.

- [92] C. B. Cooper *et al.*, “Stretchable Capacitive Sensors of Torsion, Strain, and Touch Using Double Helix Liquid Metal Fibers,” *Advanced Functional Materials*, vol. 27, no. 20, p. 1605630, 2017, doi: 10.1002/adfm.201605630.
- [93] G. Shin, B. Jeon, and Y.-L. Park, “Direct printing of sub-30 μm liquid metal patterns on three-dimensional surfaces for stretchable electronics,” *J. Micromech. Microeng.*, vol. 30, no. 3, p. 034001, Feb. 2020, doi: 10.1088/1361-6439/ab6dbc.
- [94] M. A. H. Khondoker and D. Sameoto, “Fabrication methods and applications of microstructured gallium based liquid metal alloys,” *Smart Mater. Struct.*, vol. 25, no. 9, p. 093001, Aug. 2016, doi: 10.1088/0964-1726/25/9/093001.
- [95] M. G. Mohammed and R. Kramer, “All-Printed Flexible and Stretchable Electronics,” *Advanced Materials*, vol. 29, no. 19, p. 1604965, 2017, doi: 10.1002/adma.201604965.
- [96] S. Cheng, A. Rydberg, K. Hjort, and Z. Wu, “Liquid metal stretchable unbalanced loop antenna,” *Appl. Phys. Lett.*, vol. 94, no. 14, p. 144103, Apr. 2009, doi: 10.1063/1.3114381.
- [97] G. J. Hayes, J.-H. So, A. Qusba, M. D. Dickey, and G. Lazzi, “Flexible Liquid Metal Alloy (EGaIn) Microstrip Patch Antenna,” *IEEE Transactions on Antennas and Propagation*, vol. 60, no. 5, pp. 2151–2156, May 2012, doi: 10.1109/TAP.2012.2189698.
- [98] M. Rashed Khan, G. J. Hayes, J.-H. So, G. Lazzi, and M. D. Dickey, “A frequency shifting liquid metal antenna with pressure responsiveness,” *Appl. Phys. Lett.*, vol. 99, no. 1, p. 013501, Jul. 2011, doi: 10.1063/1.3603961.
- [99] B. Yao *et al.*, “Highly stretchable and mechanically tunable antennas based on three-dimensional liquid metal network,” *Materials Letters*, vol. 270, p. 127727, Jul. 2020, doi: 10.1016/j.matlet.2020.127727.
- [100] Chung-Hao Chen and D. Peroulis, “Liquid metal droplets for RF MEMS switches,” in *Digest of Papers. 2006 Topical Meeting on Silicon Monolithic Integrated Circuits in RF Systems*, Jan. 2006, p. 4 pp.-, doi: 10.1109/SMIC.2005.1587895.
- [101] Wenjiang Shen, R. T. Edwards, and Chang-Jin Kim, “Electrostatically actuated metal-droplet microswitches integrated on CMOS chip,” *Journal of Microelectromechanical Systems*, vol. 15, no. 4, pp. 879–889, Aug. 2006, doi: 10.1109/JMEMS.2006.878877.
- [102] C.-H. Chen and D. Peroulis, “Liquid RF MEMS Wideband Reflective and Absorptive Switches,” *IEEE Transactions on Microwave Theory and Techniques*, vol. 55, no. 12, pp. 2919–2929, Dec. 2007, doi: 10.1109/TMTT.2007.910011.
- [103] P. Sen and C.-J. C. Kim, “Microscale Liquid-Metal Switches—A Review,” *IEEE Transactions on Industrial Electronics*, vol. 56, no. 4, pp. 1314–1330, Apr. 2009, doi: 10.1109/TIE.2008.2006954.

- [104] R. A. Bilodeau, D. Y. Zemlyanov, and R. K. Kramer, “Liquid Metal Switches for Environmentally Responsive Electronics,” *Advanced Materials Interfaces*, vol. 4, no. 5, p. 1600913, Mar. 2017, doi: 10.1002/admi.201600913.
- [105] M. Li, B. Yu, and N. Behdad, “Liquid-Tunable Frequency Selective Surfaces,” *IEEE Microwave and Wireless Components Letters*, vol. 20, no. 8, pp. 423–425, Aug. 2010, doi: 10.1109/LMWC.2010.2049257.
- [106] M. Li and N. Behdad, “Fluidically Tunable Frequency Selective/Phase Shifting Surfaces for High-Power Microwave Applications,” *IEEE Transactions on Antennas and Propagation*, vol. 60, no. 6, pp. 2748–2759, Jun. 2012, doi: 10.1109/TAP.2012.2194645.
- [107] P. Gurrala, S. Oren, P. Liu, J. Song, and L. Dong, “Fully Conformal Square-Patch Frequency-Selective Surface Toward Wearable Electromagnetic Shielding,” *IEEE Antennas and Wireless Propagation Letters*, vol. 16, pp. 2602–2605, 2017, doi: 10.1109/LAWP.2017.2735196.
- [108] S. Ghosh and S. Lim, “A Multifunctional Reconfigurable Frequency-Selective Surface Using Liquid-Metal Alloy,” *IEEE Transactions on Antennas and Propagation*, vol. 66, no. 9, pp. 4953–4957, Sep. 2018, doi: 10.1109/TAP.2018.2851455.
- [109] S.-Y. Tang *et al.*, “Creation of Liquid Metal 3D Microstructures Using Dielectrophoresis,” *Advanced Functional Materials*, vol. 25, no. 28, pp. 4445–4452, 2015, doi: 10.1002/adfm.201501296.
- [110] D. P. Parekh, C. Ladd, L. Panich, K. Moussa, and M. D. Dickey, “3D printing of liquid metals as fugitive inks for fabrication of 3D microfluidic channels,” *Lab Chip*, vol. 16, no. 10, pp. 1812–1820, May 2016, doi: 10.1039/C6LC00198J.
- [111] Y. Yu, F. Liu, R. Zhang, and J. Liu, “Suspension 3D Printing of Liquid Metal into Self-Healing Hydrogel,” *Advanced Materials Technologies*, vol. 2, no. 11, p. 1700173, 2017, doi: 10.1002/admt.201700173.
- [112] Y.-Z. Yu, J.-R. Lu, and J. Liu, “3D printing for functional electronics by injection and package of liquid metals into channels of mechanical structures,” *Materials & Design*, vol. 122, pp. 80–89, May 2017, doi: 10.1016/j.matdes.2017.03.005.
- [113] A. Fassler and C. Majidi, “Liquid-Phase Metal Inclusions for a Conductive Polymer Composite,” *Advanced Materials*, vol. 27, no. 11, pp. 1928–1932, 2015, doi: 10.1002/adma.201405256.
- [114] N. Kazem, T. Hellebrekers, and C. Majidi, “Soft Multifunctional Composites and Emulsions with Liquid Metals,” *Advanced Materials*, vol. 29, no. 27, p. 1605985, 2017, doi: 10.1002/adma.201605985.

- [115] E. J. Markvicka, M. D. Bartlett, X. Huang, and C. Majidi, “An autonomously electrically self-healing liquid metal–elastomer composite for robust soft-matter robotics and electronics,” *Nature Materials*, vol. 17, no. 7, Art. no. 7, Jul. 2018, doi: 10.1038/s41563-018-0084-7.
- [116] W. Tang *et al.*, “Liquid-Metal Electrode for High-Performance Triboelectric Nanogenerator at an Instantaneous Energy Conversion Efficiency of 70.6%,” *Advanced Functional Materials*, vol. 25, no. 24, pp. 3718–3725, 2015, doi: <https://doi.org/10.1002/adfm.201501331>.
- [117] R. C. Gough, J. H. Dang, A. M. Morishita, A. T. Ohta, and W. A. Shiroma, “Frequency-tunable slot antenna using continuous electrowetting of liquid metal,” in *2014 IEEE MTT-S International Microwave Symposium (IMS2014)*, Jun. 2014, pp. 1–4, doi: 10.1109/MWSYM.2014.6848565.
- [118] M. Wang, C. Trlica, M. R. Khan, M. D. Dickey, and J. J. Adams, “A reconfigurable liquid metal antenna driven by electrochemically controlled capillarity,” *Journal of Applied Physics*, vol. 117, no. 19, p. 194901, May 2015, doi: 10.1063/1.4919605.
- [119] M. Varga, C. Ladd, S. Ma, J. Holbery, and G. Tröster, “On-skin liquid metal inertial sensor,” *Lab Chip*, vol. 17, no. 19, pp. 3272–3278, Sep. 2017, doi: 10.1039/C7LC00735C.
- [120] J. H. Yoo, “A study on polymeric microfluidic and implantable neural devices,” Ph.D., The University of Texas at Dallas, United States -- Texas, 2016.
- [121] S. Seethapathy and T. Górecki, “Applications of polydimethylsiloxane in analytical chemistry: A review,” *Analytica Chimica Acta*, vol. 750, pp. 48–62, Oct. 2012, doi: 10.1016/j.aca.2012.05.004.
- [122] M. J. Madou, *Fundamentals of microfabrication: the science of miniaturization*. CRC press, 2002.
- [123] Ariana Bratt and Andrew Barron, “XPS of Carbon Nanomaterials. Carbon Nanotubes - OpenStax CNX.” https://cnx.org/contents/oDCdCjdZ@1.1:_d2_mDnO/XPS-of-Carbon-Nanomaterials (accessed Sep. 12, 2020).
- [124] A. L. Cordeiro *et al.*, “Fluorination of poly(dimethylsiloxane) surfaces by low pressure CF₄ plasma : physicochemical and antifouling properties.” Jan. 01, 2009, Accessed: May 04, 2020. [Online]. Available: <http://resolver.tudelft.nl/uuid:692c44dc-b83e-4fde-b0e5-13f11400152f>.
- [125] M. Manca, B. Cortese, I. Viola, A. S. Aricò, R. Cingolani, and G. Gigli, “Influence of Chemistry and Topology Effects on Superhydrophobic CF₄-Plasma-Treated Poly(dimethylsiloxane) (PDMS),” *Langmuir*, vol. 24, no. 5, pp. 1833–1843, Mar. 2008, doi: 10.1021/la703077u.

- [126] Y. Wang, M. Bachman, C. E. Sims, G. P. Li, and N. L. Allbritton, "Simple Photografting Method to Chemically Modify and Micropattern the Surface of SU-8 Photoresist," *Langmuir*, vol. 22, no. 6, pp. 2719–2725, Mar. 2006, doi: 10.1021/la053188e.
- [127] R. N. Wenzel, "Resistance of solid surfaces to wetting by water," *Industrial & Engineering Chemistry*, vol. 28, no. 8, pp. 988–994, 1936.
- [128] A. Cassie and S. Baxter, "Wettability of porous surfaces," *Transactions of the Faraday society*, vol. 40, pp. 546–551, 1944.
- [129] D. B. Mahadik *et al.*, "Effect of surface composition and roughness on the apparent surface free energy of silica aerogel materials," *Appl. Phys. Lett.*, vol. 99, no. 10, p. 104104, Sep. 2011, doi: 10.1063/1.3635398.
- [130] H. C. Barshilia, D. K. Mohan, N. Selvakumar, and K. S. Rajam, "Effect of substrate roughness on the apparent surface free energy of sputter deposited superhydrophobic polytetrafluoroethylene thin films," *Appl. Phys. Lett.*, vol. 95, no. 3, p. 033116, Jul. 2009, doi: 10.1063/1.3186079.
- [131] E. Chibowski, "Apparent Surface Free Energy of Superhydrophobic Surfaces," *Journal of Adhesion Science and Technology*, vol. 25, no. 12, pp. 1323–1336, Jan. 2011, doi: 10.1163/016942411X555890.
- [132] Y. Yan, E. Chibowski, and A. Szcześ, "Surface properties of Ti-6Al-4V alloy part I: Surface roughness and apparent surface free energy," *Materials Science and Engineering: C*, vol. 70, pp. 207–215, Jan. 2017, doi: 10.1016/j.msec.2016.08.080.
- [133] L. A. Girifalco and R. J. Good, "A Theory for the Estimation of Surface and Interfacial Energies. I. Derivation and Application to Interfacial Tension," *J. Phys. Chem.*, vol. 61, no. 7, pp. 904–909, Jul. 1957, doi: 10.1021/j150553a013.
- [134] R. J. Good and L. A. Girifalco, "A THEORY FOR ESTIMATION OF SURFACE AND INTERFACIAL ENERGIES. III. ESTIMATION OF SURFACE ENERGIES OF SOLIDS FROM CONTACT ANGLE DATA," *J. Phys. Chem.*, vol. 64, no. 5, pp. 561–565, May 1960, doi: 10.1021/j100834a012.
- [135] F. M. Fowkes, "ATTRACTIVE FORCES AT INTERFACES," *Ind. Eng. Chem.*, vol. 56, no. 12, pp. 40–52, Dec. 1964, doi: 10.1021/ie50660a008.
- [136] F. M. FOWKES, "Characterization of Solid Surfaces by Wet Chemical Techniques," in *Industrial Applications of Surface Analysis*, vol. 199, 0 vols., AMERICAN CHEMICAL SOCIETY, 1982, pp. 69–88.
- [137] K.-Y. Law and H. Zhao, *Surface wetting: characterization, contact angle, and fundamentals*. Springer Switzerland, 2016.

- [138] C. J. van Oss, R. J. Good, and R. J. Busscher, “Estimation of the Polar Surface Tension Parameters of Glycerol and Formamide, for Use in Contact Angle Measurements on Polar Solids,” *Journal of Dispersion Science and Technology*, vol. 11, no. 1, pp. 75–81, Feb. 1990, doi: 10.1080/01932699008943237.
- [139] D. K. Owens and R. C. Wendt, “Estimation of the surface free energy of polymers,” *Journal of Applied Polymer Science*, vol. 13, no. 8, pp. 1741–1747, 1969, doi: 10.1002/app.1969.070130815.
- [140] Y. Song, F. Xin, G. Guangyong, S. Lou, C. Cao, and J. Wang, “Uniform generation of water slugs in air flowing through superhydrophobic microchannels with T-junction,” *Chemical Engineering Science*, vol. 199, pp. 439–450, May 2019, doi: 10.1016/j.ces.2019.01.041.
- [141] M. A. Eddings, M. A. Johnson, and B. K. Gale, “Determining the optimal PDMS–PDMS bonding technique for microfluidic devices,” *J. Micromech. Microeng.*, vol. 18, no. 6, p. 067001, Apr. 2008, doi: 10.1088/0960-1317/18/6/067001.
- [142] C. -f Chen and K. Wharton, “Characterization and failure mode analyses of air plasma oxidized PDMS–PDMS bonding by peel testing,” *RSC Advances*, vol. 7, no. 3, pp. 1286–1289, 2017, doi: 10.1039/C6RA25947B.
- [143] T. W. Ebbesen, H. J. Lezec, H. F. Ghaemi, T. Thio, and P. A. Wolff, “Extraordinary optical transmission through sub-wavelength hole arrays,” *Nature*, vol. 391, no. 6668, Art. no. 6668, Feb. 1998, doi: 10.1038/35570.
- [144] S. G. Rodrigo, F. de León-Pérez, and L. Martín-Moreno, “Extraordinary Optical Transmission: Fundamentals and Applications,” *Proceedings of the IEEE*, vol. 104, no. 12, pp. 2288–2306, Dec. 2016, doi: 10.1109/JPROC.2016.2580664.
- [145] R. Gordon, D. Sinton, K. L. Kavanagh, and A. G. Brolo, “A New Generation of Sensors Based on Extraordinary Optical Transmission,” *Acc. Chem. Res.*, vol. 41, no. 8, pp. 1049–1057, Aug. 2008, doi: 10.1021/ar800074d.
- [146] S. Kumar, N. J. Wittenberg, and S.-H. Oh, “Nanopore-Induced Spontaneous Concentration for Optofluidic Sensing and Particle Assembly,” *Anal. Chem.*, vol. 85, no. 2, pp. 971–977, Jan. 2013, doi: 10.1021/ac302690w.
- [147] S. Yokogawa, S. P. Burgos, and H. A. Atwater, “Plasmonic Color Filters for CMOS Image Sensor Applications,” *Nano Lett.*, vol. 12, no. 8, pp. 4349–4354, Aug. 2012, doi: 10.1021/nl302110z.
- [148] W. L. Barnes, A. Dereux, and T. W. Ebbesen, “Surface plasmon subwavelength optics,” *Nature*, vol. 424, no. 6950, Art. no. 6950, Aug. 2003, doi: 10.1038/nature01937.

- [149] R. Sambles, “More than transparent,” *Nature*, vol. 391, no. 6668, Art. no. 6668, Feb. 1998, doi: 10.1038/35509.
- [150] C. Genet and T. W. Ebbesen, “Light in tiny holes,” *Nature*, vol. 445, no. 7123, Art. no. 7123, Jan. 2007, doi: 10.1038/nature05350.
- [151] J. Wang, S. Liu, Z. V. Vardeny, and A. Nahata, “Liquid metal-based plasmonics,” *Opt. Express, OE*, vol. 20, no. 3, pp. 2346–2353, Jan. 2012, doi: 10.1364/OE.20.002346.
- [152] D. K. Schroder, *Semiconductor Material and Device Characterization*. John Wiley & Sons, 2015.
- [153] Polyanskiy, M. N., “Refractive index of Al (Aluminium) - Rakic,” *Refractive index of Al (Aluminium) - Rakic*. <https://refractiveindex.info/?shelf=main&book=Al&page=Rakic> (accessed Mar. 26, 2021).
- [154] A. D. Rakić, “Algorithm for the determination of intrinsic optical constants of metal films: application to aluminum,” *Appl. Opt., AO*, vol. 34, no. 22, pp. 4755–4767, Aug. 1995, doi: 10.1364/AO.34.004755.

BIOGRAPHICAL SKETCH

Sachin Babu received his BS degrees in Physics and Electrical Engineering from The University of Texas at Dallas in 2001. In 2011, he decided to go back to The University of Texas at Dallas to earn his MS degree in Mechanical Engineering. Starting from Fall of 2013, he began his PhD career in Electrical Engineering within the Department of Electrical Engineering at The University of Texas at Dallas under the supervision of Prof. Jeong-Bong (JB) Lee. His research focused primarily on PDMS-based devices such as guided mode resonance strain sensors, liquid metal plasmonics, plasma-treated surfaces, and liquid metal microfluidics. In addition to his research, he has interests in developing compliant actuators for robotics, triboelectric nanogenerators for energy harvesting, and machine learning applications for smart surface characterization. After receiving his degree, he plans to pursue a career in research, in either academia or industry.

CURRICULUM VITAE

EDUCATION

PhD Electrical Engineering	University of Texas at Dallas	2021
MS Mechanical Engineering	University of Texas at Dallas	2012
BS Electrical Engineering	University of Texas at Dallas	2001
BS Physics	University of Texas at Dallas	2001

RESEARCH EXPERIENCE

- 5+ years of microfabrication and clean room experience, including UV photolithography, e-beam lithography; various metal and dielectric deposition and etching tool experience; solvent, acid, and base hood experience.
- 5+ years characterization experience, including scanning electron microscopy (SEM), atomic force microscopy (AFM), profilometry, reflectometry, ellipsometry, as well as optical microscopy.
- 2+ years of 3D printing experience (both FDM and SLA resin), including computer aided design (CAD) of models using AutoCAD, FreeCAD, OpenSCAD, and Cura.
- 2+ years of liquid metal microfluidics experience, including complex microfluidics channel mold making, pneumatically sealed connectors, syringe pump operations, and contact angle goniometry.

PUBLICATIONS

1. Babu S.; Dousti B.; Lee G.S.; Lee, J.B. “Conversion of polymer surfaces into nonwetting substrates for liquid metal microfluidics.” (submitted to *Langmuir*), March 2021.
2. Babu, S.; Lee, J.-B. Axially-Anisotropic Hierarchical Grating 2D Guided-Mode Resonance Strain-Sensor. *Sensors* 2019, *19*, 5223.
3. Dousti, B.; Babu, S.; Choi, M.; Lee, J. B.; Lee, G. S. “Highly flexible all-solid-state on-chip microsupercapacitors for portable electronics: a self-powered integrated system.” (submitted to *Carbon*), April 2021.
4. Qaradaghi, V.; Ramezany, A.; Babu, S.; Lee, J.B.; Pourkamali, S. Nanoelectromechanical Disk Resonators as Highly Sensitive Mass Sensors. *IEEE Electron Device Letters* 2018, *39*, 1744–1747.
5. Xu, T.; Yoo, J.H.; Babu, S.; Roy, S.; Lee, J.-B.; Lu, H. Characterization of the mechanical behavior of SU-8 at microscale by viscoelastic analysis. *J. Micromech. Microeng.* 2016, *26*, 105001.

CONFERENCES AND PROCEEDINGS

1. Babu, S.; Lee, J.B. Plasma-treated PDMS as intrinsically non-wetting surface for gallium-alloy liquid metal microfluidics. In Proceedings of the 2020 IEEE 30th International Conference on Micro Electro Mechanical Systems (MEMS); 2020.
2. Ramezany, A.; Babu, S.; Kumar, V.; Lee, J.-B.; Pourkamali, S. Resonant piezoresistive amplifiers: Towards single element nano-mechanical RF front ends. In Proceedings of

the 2017 IEEE 30th International Conference on Micro Electro Mechanical Systems (MEMS); 2017; pp. 72–75.

3. Arkadeep, M.; Xu, K.; Babu, S.; Choi, J. H.; Lee, J.-B. “Liquid metal-based flexible band-stop frequency selective surface.” *2021 IEEE 34rd International Conference on Micro Electro Mechanical Systems (MEMS)*. IEEE, 2021.